ELECTRICAL IMPEDANCE TOMOGRAPHY WITH NEURAL NETWORKS AND FUZZY SETS

BY

ABDOLHOSSEIN NEJATALI

A Thesis
Submitted to the faculty of Graduate Studies
in Partial Fulfilment of the Requirements for the Degree of

DOCTOR OF PHILOSOPHY

Department of Electrical and Computer Engineering
University of Manitoba
Winnipeg, Manitoba

THE UNIVERSITY OF MANITOBA

FACULTY OF GRADUATE STUDIES

*****

COPYRIGHT PERMISSION PAGE

ELECTRICAL IMPEDANCE TOMOGRAPHY WITH NEURAL NETWORKS AND FUZZY SETS

BY

ABDOLHOSSEIN NEJATALI

A Thesis/Practicum submitted to the Faculty of Graduate Studies of The University of Manitoba in partial fulfillment of the requirements of the degree of

DOCTOR OF PHILOSOPHY

Acknowledgement

I am indebted to professor Ioan R. Ciric, my advisor, for his thoughtful and generous guidance throughout this research program.

I am grateful to other Ph.D. committee members, professors W. Lehn and E. Shwedyk for their support and comments.

I also thank Dr. N. Sepehri who reviewed the manuscript and attended the oral presentation.

I appreciate the insightful discussions and encouragements contributed by my colleagues and fellow students in the Department of Electrical and Computer Engineering at the University of Manitoba.

I dedicate this Thesis to my wife, Cima Cina, without whose constant encouragement, this Thesis would not have been possible, and to my children Fatemeh and Mostafa who I am proud of them.

I also dedicate this Thesis to my parents, Mohammad-Hassan Nejatali and Parveen Eftekhar, without whose support I would not have contemplated this endeavour.

Funding for this project was provided by:

The Ministry of Culture and Higher Education of Iran,

The Manitoba Cancer Treatment and Research Foundation,

and The University of Manitoba.

Abstract

Various imaging procedures, providing different types of information and based on different physical properties of the tissues, are characterized by specific complexities, degrees of hazard, resolutions and price. Electrical impedance tomography (EIT) has the advantage of a low price and simplicity, as well as of not having any known hazards, such as ionising radiation, which makes it particularly attractive. However, it has the disadvantage of a low resolution. The information provided by EIT could be used directly for medical diagnosis or in combination with other imaging systems.

In EIT the electric current is applied to the periphery of the body and the corresponding voltage is measured in order to find the internal distribution of conductivity and permittivity.

In this thesis, the EIT performance has been improved in three different aspects: 1) improving the network approximation method for solving the electrode voltages when the distribution of conductivity and permittivity within the object as well as injecting current pattern are known, namely, the forward problem; 2) utilizing neural networks in an iterative procedure for solving the conductivity distribution when the electrode voltages as well as injecting current pattern are known, namely, the inverse problem; and 3) improvising a new method for image fusion based on fuzzy set theory to be used in a multifrequency scheme to increase certainty and accuracy.

TABLE OF CONTENTS

List of Tables

List of Figures

1. INTRODUCTION

Electrical impedance tomography is defined as a technique which from a knowledge of voltage and current on the boundary of a region, determines the spatial distribution of conductivity and permittivity within the region. Hence, electrical impedance tomography may be considered as a member of imaging techniques (see Table 1), in which the common goal is to noninvasively determine certain physical characteristics within a particular region. Noninvasive imaging techniques are widely used in medical practice. The wide variety of techniques has arisen because of the ability of each to provide complementary information to the others.

The information provided by any of these imaging techniques is different, primarily because of the different physical phenomena that are measured. The use of different mechanisms means that different equipment, different data-collection strategies and different data-processing algorithms are used for each imaging technique. Therefore, although all of these techniques have a common objective, and all produce a similar end result, i.e. an image, they have widely different functional characteristics, e.g. cost, speed, size, portability, accuracy, resolution, safety, and operator skills.

Electrical impedance tomography (EIT) is not a new technique. Since about 1930, this technique has been used by geophysicists to determine the conductivity of different layers (strata) close to the Earth's surface [115]. The identification of these strata and their

conductivities, along with the known properties of rocks and minerals, is an aid in the prospecting for minerals and oil.

Table 1: Medical imaging techniques; most popular techniques are mentioned here. For each technique the, mechanism of measurement and physical characteristic which determines the contrast between different tissues, is given [115].

Technique	Mechanism of measurement	Physical characteristic measured
Ultrasound	Reflection and scattering of ultrasonic waves	Changes in acoustic impedance
X-ray computer tomography	Transmission of X-ray	X-ray absorptivity
Nuclear magnetic resonance imaging	Magnetic and electric fields	Spin relaxation times, proton density
Positron emission tomography	Nuclear particle emissions	Density of administrated isotope
Electrical impedance tomography	Electric currents	Electric conductivity and permittivity

EIT has numerous practical applications, e.g. in quality control and fault detection for various materials [36], in multicomponent fluid flow analysis [100], geological exploration [30], and medical imaging [5]. Recently, it seems following the advent of other medical imaging techniques, people have seriously considered impedance imaging as an aid to medical diagnosis [60,106]. The rationale for its use is based on the knowledge that different tissues and fluids within the body possess different values of conductivity and permittivity and dependency on frequency (see Table 2). It therefore follows that the ability to image conductivity and permittivity permits the visualization of the various tissues. There is also evidence that the electrical properties of tissue vary according to its state of health, which raises the possibility of distinguishing between healthy and

abnormal tissue.

Table 2: Conductivity and relative permittivity of some tissues [6,49,106]

Tissue	Conductivity [S/m]		Relative permittivity	
	100 kHz	150 kHz	100 kHz	150 kHz
Cerebrospinal fluid	1.54	NA	NA	NA
Plasma	1.52	NA	NA	NA
Blood	0.667	NA	NA	NA
Liver	0.123 - 0.286	0.144	11 700	10 000
Human arm	0.417 (longitudinal) 0.148 (transverse)	NA	NA	NA
Skeletal muscle	0.8 (longitudinal) 0.0556 (transverse) 0.428 (average)	0.462	14 800	11 900
Cardiac muscle	0.625 (longitudinal) 0.236 (transverse) 0.43 (average)	NA	NA	NA
Neural tissue -gray matter -white matter	0.172 0.352 0.147	NA	NA	NA
Lung	0.0423 - 0.138	NA	NA	NA
Fat	0.0337 - 0.0485	0.0342	89.5	78.9
Bone	0.0060 - 0.0085	0.0090	163	141
Spleen	0.593	0.593	3 160	2 830
Pancreas	0.297	0.305	10 000	8 420
Kidney	0.110	0.120	7 610	5 970

2. ELECTRICAL IMPEDANCE TOMOGRAPHY SYSTEM

Electrical impedance measurements have been used to study biological systems since the late 1800s. Very generally, investigations can be divided into two major categories [2]: (1) studies conducted to investigate fundamental electric properties and to correlate these properties with tissue structure and (2) measurement of physiological events. Investigations of the electric properties of tissue have employed measurements of both real and reactive components of impedance at a number of frequencies; the earlier studies were conducted on various cell suspensions to identify cell membrane properties. In contrast, because of instrumentation limitations and safety considerations, studies directed toward detection of physiological events have usually been conducted at a single frequency above 20kHz and generally only impedance magnitude has been measured. It should be mentioned that this study has nothing to do with internal body electrical sources such as those generated by the heart or brain. In an effort to eliminate their consequences, the frequencies which are being used in electrical impedance tomography are much larger than internal sources frequencies (i.e. heart or brain) and a high pass filter is used before measuring instruments.

2.1 Biological Effects of Current Flow

The threshold of sensation for low-frequency currents applied between electrodes

placed on the skin generally rises with frequency. Three distinct types of sensation occur as frequency increases [6].

At frequencies below approximately 0.1 Hz individual cycles can be discerned as a periodic stinging sensation; this is thought to arise as a result of electrolysis at the electrode-tissue interface. Currents as low as 100 μA can be felt. At frequencies above 10 Hz electrolysis effect appear to be reversible and the dominant biological effect is that of neural stimulation. However, as frequency is further increased the threshold for neural stimulation increases and beyond approximately 10 kHz no neurai stimulation takes place and ohmic heating of the tissue becomes the dominant biological effect [6].

2.2 Electrodes

Before considering how to form impedance images from a set of voltage and current measurements, it is worthwhile considering what measurements should be obtained and the problems in doing so. In general measurements of impedance are performed by connecting electrodes to a conductive region and driving a current between them. The resulting voltage then may be measured with a suitable voltmeter. Measurement of voltage between two electrodes, while current is being passed, clearly produces inadequate information for imaging. What actually is done, is that an array of electrodes (i.e. 16 or 32) is connected around the body (e.g. thorax). Then current is applied to some or all of these electrodes and the developed voltages are measured on them. To achieve the maximum amount of information, this is repeated for all the independent measurements.

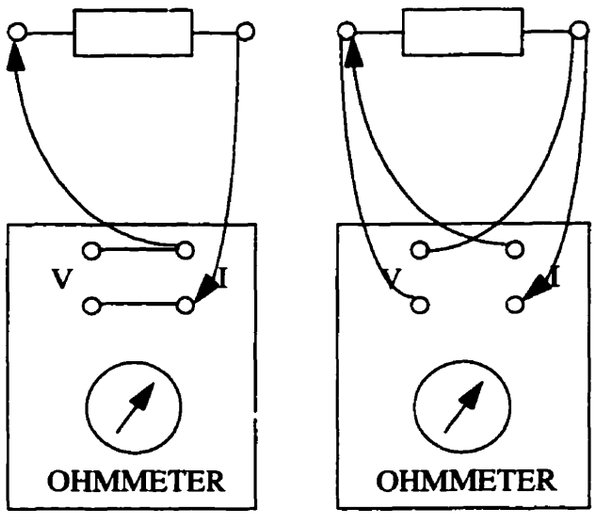

Fig. 2.1 (a) Two wire ohmmeter method; (b) four wire ohmmeter method.

2.2.1 Two and Four Electrodes Arrangement

Ohmmeters usually use a two wire method for measuring resistivity, but it is well know that the four wire method is more accurate. The reason for better results for four wire methods lies in the exclusion of the resistance of current-carrying wires from the measurements (see Fig. 2.1). The ohmmeter performs a division of voltage by applied current and in the two wire method, resistivity of wires is included. In contrast, in the four wire method, voltage is measured by separate wires and as there is not a significant amount of current in these wires (voltage measurement is done by a very high resistive device) their resistivity is excluded in the readings.

In measuring the resistivity or impedance of human tissue, using the four wire method has an additional advantage. In this case by using a separate pair of electrodes for measuring voltage, the resistance of electrode-skin interface and most of the skin

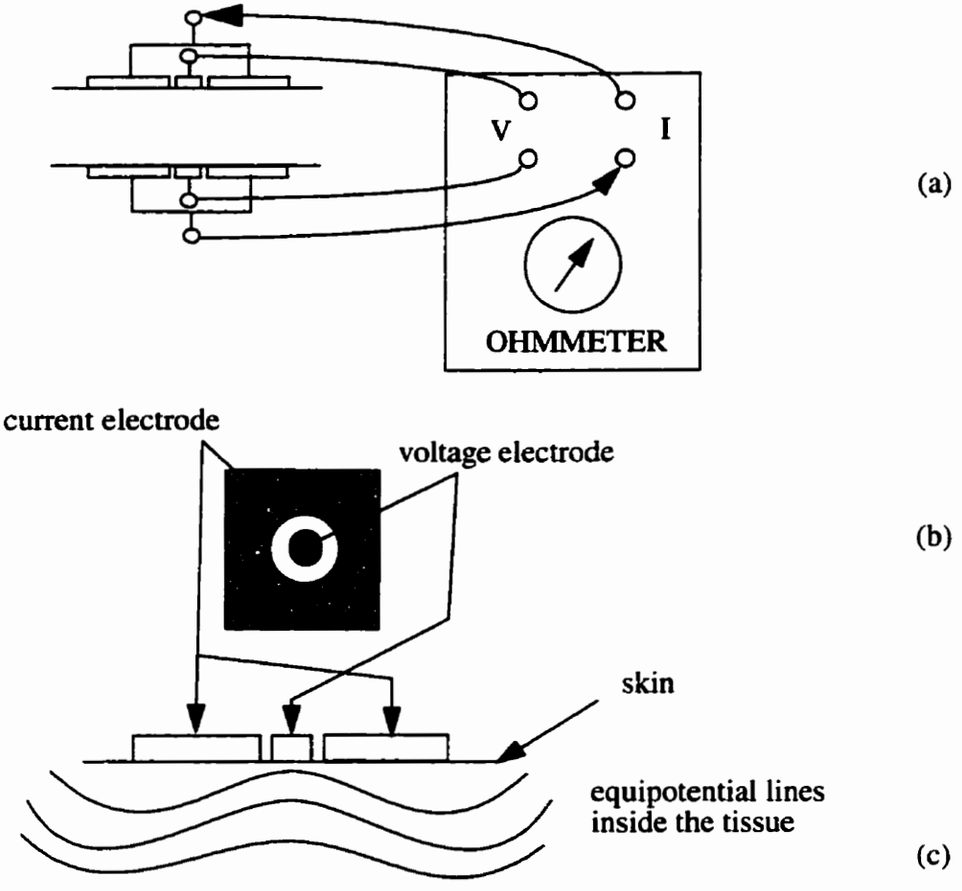

Fig. 2.2 (a) Four electrode method; (b) configuration of compound electrode; (c) equipotential lines inside the tissue which explains, in the four electrode method, what actually is measured, is the voltage beneath the skin, so electrode-skin impedance and skin impedance are almost excluded.

impedance will be excluded in measurements (see Fig. 2.2 for details). Equipotential lines have been shown in Fig. 2.2. As can be seen the voltage of the voltage-electrode is the same as the voltage beneath the skin for current-electrode, so what is measured by the voltage-electrode is actually the voltage produced by injected current when electrode impedance and electrode-skin impedance are excluded. To achieve this property and to

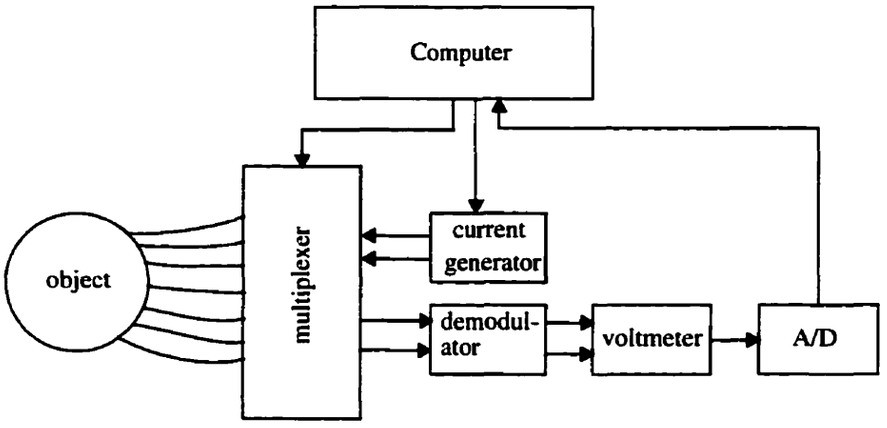

Fig. 2.3 Block diagram of a very simple EIT system which shows main components.

keep both current and voltage electrodes as close as possible, a compound electrode has been introduced [62]. As the voltage electrode is not carrying a significant amount of current, its size is much smaller than the current electrode (see Fig. 2.2) [111].

2.3 Hardware

Like any other imaging device, there is a variety of instruments that make up an electrical impedance tomography system. Among them one can name current generators, demodulators, voltmeters, interfaces, and computer facilities.

Basic components of an electrical impedance tomography system are shown in Fig. 2.3. It should be noted that in comparison to other imaging systems, EIT has one of the most simple, inexpensive, and small-size hardwares.

2.3.1 Current Generators

To measure an unknown impedance, one must do one of two things. Either apply a known voltage across the object and then measure the current through it, or inject a known current into that object and measure the voltage across it. Both of these methods have been used for various EIT and similar systems. The current generator-voltmeter couple has a technical advantage over the voltage generator-ampmeter. The main reason lies in the simplicity of building a current generator over an ampmeter. In the next chapter, it will be shown that (virtually) there are two different methods in data collection from the current generator point of view. In one of them only one pair of electrodes is driven by a current generator and this pair will be changed during the sampling time. In this case, one current generator and a multiplexer is enough. In the other case, all electrodes are simultaneously driven with current generators. In this case one needs as many current generators as electrodes. Obviously the second strategy needs more hardware in return for better distinguishability [68].

It is well known that current generators are actually voltage generators with a large internal impedance. Voltage sources are available with an internal impedance which can be adjusted automatically or through a voltage signal. Thus the required internal impedance can be adjusted through software which in turn controls a voltage signal. These sources are ideal for our purpose. In addition, to having complete synchronization between current sources and demodulators, programmable read only memories (PROM) are perfect devices. The wave form of a sinusoid can be stored with very small time steps in a PROM, then a timing device produces addresses of this PROM and the stored value in turn goes to a digital to analog convertor (D/A). This analog signal can be used as a

reference for all current sources and demodulators [24].

2.3.2 Demodulators

All signals in EIT system are sinusoidally modulated. But it is the amplitude of the voltages and currents that we are interested in, therefore, demodulators have to be implemented to determine the required amplitudes.

Moreover, it was already mentioned that the impedance of tissues is frequency dependant. Thus multifrequency scheme has been suggested to increase the acquired information from a limited number of electrodes. The interesting point is that these different frequencies may be applied at the same time and be decomposed during the demodulation. This technique further decreases the sampling time [24,48,102].t

2.3.3 Stray Capacitances

It was indicated that using four electrode method improves measurement accuracy, but this technique is not too effective in eliminating stray capacitances. These are capacitances between wires and ground as well as between wires and are in parallel with tissue's impedance.

One way to decrease the effect of these impedances, is to install current generators and demodulators as near as possible to the electrodes. Development of integrated circuits for these devices would enable the installation of them in the electrode compartment.

2.3.4 Voltmeters

The demodulated signal goes to a voltmeter. There are several electrodes around

the body (i.e. 16 or 32 or 64). There may be just one voltmeter and a multiplexer which selects which electrode is to be connected to the voltmeter (see Fig. 2.3), or there may be the same number of voltmeters as electrodes. The former will have lower cost and longer sampling time.

As will be seen in the next chapter, the data collection method has a direct impact on the measurement signal to noise ratio (SNR). The expected range of voltages for the neighboring method, for instance, in a 64 electrode system is 1 to 2800 [14]. Obviously without an automatic adjusting scheme for the voltmeter range, the SNR would be very low.

Furthermore to achieve the required precision, high precision voltmeters are needed. So far, measurement devices (current source, demodulator, voltmeter and A/D convertor) with up to 16 bits of precision have been built, but precision up to 24 bits is also feasible [24].

2.3.5 Interfacing and Computer

All reconstruction methods need a considerable amount of computation to produce an image from raw data. Reconstruction of an image in EIT is not an exception and so a computer and an interface to convert analog signals to digital ones (A/D) is inevitable. A/Ds are common devices for interfacing. In previous subsections, it was mentioned that some or all devices may use digital techniques. In that case, output data is already in the correct format to be fed into a computer, otherwise, A/Ds should be used.

Selection of the computer depends on the reconstruction method as well as availability. For example the earliest clinically useful CT scanners were based on mini-computer

architectures that were minuscule by today's standards. The first such machines used a 16-bit processor, with only 64k bytes of memory. With the falling cost of computer power, system designers have integrated much faster computers, array processors, multiple viewing stations, and other features into medical instruments. This escalation in computer power has permitted more accurate and stable reconstruction algorithms, while keeping reconstruction times on the same order of magnitude as data acquisition times.

In contrast, the non-linear nature of the EIT problem results in reconstruction algorithms that are computationally intensive. As will be seen later, Yorkey implemented and reviewed the performance of six reconstruction algorithms and found that the most accurate, a Newton-Raphson technique, required several hundred CPU seconds per iteration for a 16 electrode simulation on an 8 by 8 element resistivity mesh [131].

Simske has implemented a one step Newton-Raphson technique for a 32 electrode system with a 496 element resistivity mesh [118]. This program has been modified to run on processors ranging from Sun 3/50 workstation to a Cray X/MP-48 supercomputer. Results of run time analysis (see Table 3) indicate that implementation of the current

Table 3: Run time of Newton-Raphson method of a 32 electrodes EIT system [43].

Computer	Run time (seconds)
Sun 3/60 workstation	3 239
Sun 4/280	350
IBM 3081-D	165
Cray X-MP/48	6

program on small machines is clearly impractical. Since this algorithm runs in $O(n^4)$, with n the number of electrodes, run times for a 64 electrode system would be intolerable on any but the largest supercomputers.

It is obvious that a high computational burden is not welcomed and is a major drawback for such a reconstruction method. It is the aim in this research to develop a method with acceptable reconstruction time.

Following review of EIT systems, data collection methods in EIT are presented next[24].

3. DATA COLLECTION METHODS

Electrical impedance tomography reconstructs the conductivity and permittivity within an object based on the conditions of voltage and current on the surface of the object. To determine the conditions of the current and voltage on the surface, one can inject the current through a set of the electrodes in contact with the surface and measure the developed voltages. There are numerous ways in which the current-injecting electrodes, voltage measuring electrodes and current patterns are chosen. This section describes various methods by which the current is injected and the voltages are measured. Upon completion of these measurements, numerical reconstruction methods to be described in the next chapter may be employed to reconstruct the distribution of conductivity and permittivity within the object.

3.1 Neighboring Method

Brown *et al* [20] introduced the neighboring method of data collection. In this method, the current is applied through two adjacent electrodes and voltages are measured from all other successive pairs of neighboring electrodes in this four electrode method, though compound electrodes have not been used. Data collection for a 16-electrode system is shown in Fig. 3.1. Current is injected through electrode pair 1-2 and voltage is measured on all other pairs, e.g. electrode pair 6-7. The current flows throughout the

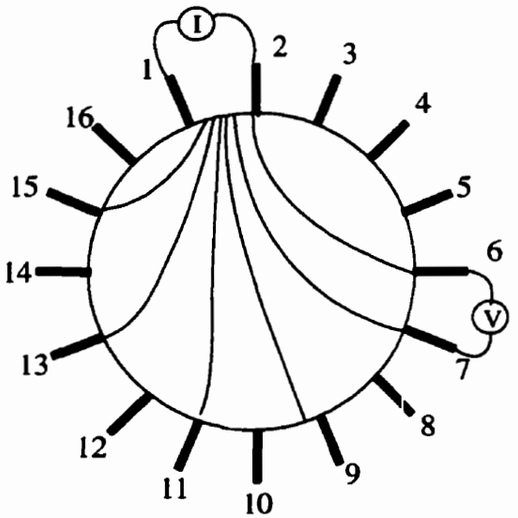

Fig. 3.1 In the neighboring method, currents are injected through neighboring electrodes and voltages are measured between adjacent pairs of electrodes.

object, with its intensity maximal at the periphery near the current-injecting electrodes and diminishing rapidly towards the opposite side. Figure 3.1 shows some equipotential lines, and the portion between those two lines that terminate on electrodes 6 and 7, represents the impedance zone for these electrodes. The voltages are measured between all the other electrode pairs, i.e., 3-4, 4-5, 5-6, ... , 15-16. These 13 voltage measurements are independent. The current injecting pair changes to electrode pair 2-3 and all 13 voltages are measured on other neighboring electrodes. Each set of these voltage measurements are called a projection angle in analogy to a X-ray CT scanner. Repeating this procedure for the sixteen electrode pairs, produces $16 \times 13 = 208$ voltage measurements. However, not all of these measurements are independent, since the reversal of voltage and current electrode pairs would give an identical value of the measured impedance (reciprocity

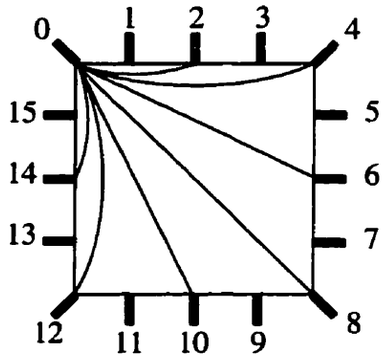

Fig. 3.2 Current injecting electrodes in the cross method.

theorem). Thus, only 104 independent measurements are obtained for the above 16-electrode system.

The neighboring method of data collection has a very nonuniform current distribution. Most of the current flows near the current injecting electrodes and hence good sensitivity is obtained at the periphery. This method does not yield good sensitivity at the center because the current density is low there.

In general when the voltages of current carrying electrodes are used as well, then in an n-electrode system, there are n(n-1)/2 independent measurements, i.e. in a 16-electrode system, there is 16(16-1)/2=120 independent measurements. Brown *et al* have not utilized all of these because in their reconstruction method, they do not measure voltages on the current carrying electrodes.

3.2 Cross Method

Compared to the neighboring method, the current in the cross method, proposed by

Hua *et al* [61], is more uniformly distributed as the current injecting electrodes are separated by large dimensions. The data collection system in shown in Fig. 3.2. Electrode 0 is taken as current reference and electrode 1 as voltage reference. The current is then applied successively to even electrodes, i.e. 2, 4, ... , 14 and voltage is measured on all other electrodes with respect to the voltage reference electrode. The second data set is obtained by switching the current reference to electrode 3 and the voltage reference to electrode 2 and injecting current through odd electrodes, i.e., 5, 7, ... , 15, 1. This means 13 voltage measurements for seven different current injecting electrodes for each set, which yields $2 \times 7 \times 13 = 182$ data points. Thus a 16-electrode system yields a maximum of 182 data points, out of which only 104 are independent measurements. The cross method does not have as good a sensitivity in the periphery as the neighboring method, but, has better matrix conditioning and sensitivity over the entire region.

3.3 Opposite Method

Opposite method was also proposed by Hua *et al* [61]. In this method, current injecting electrodes are diametrically opposed to each other. The voltage reference electrode is selected to be the neighbour of current injecting electrode.

For a 16-electrode system, there are 8 different current injecting electrode pairs and 13 voltages corresponding to each pair of them, therefore, a total of $8 \times 13 = 104$ data points can be obtained. Not all of these measurements are independent, but, this method has more uniform current density and hence good sensitivity.

3.4 Adaptive Method

Adaptive method or as it is sometimes called the optimal current method was proposed by Gisser *et al* [42] and is based on applying current to all electrodes. As such, compound electrodes should be used for this data collection method. The amplitude of the currents are chosen in an iterative algorithm such that the optimal currents are obtained. The optimal current is defined as a current pattern that maximizes the measured electrode voltages, for a constraint current amplitude. This method gives the best distinguishability [68] and is the most versatile method of data collection. For a homogeneous impedance distribution, the amplitude of the current in the electrodes follows a cosine curve (spatially), to give a perfectly uniform current distribution. In maximizing distinguishability, an interactive experimental process must be pursued to approximate a best current i to distinguish between two areas with different impedances. The basic idea for this method can be shown easily using the following formulation [64].

Let $\boldsymbol{R}(\rho)$ denote the resistance matrix for the original impedance distribution ρ and $\boldsymbol{R}(\hat{\rho})$ the estimated resistivity distribution for $\hat{\rho}$. The voltage difference for a given current pattern $\boldsymbol{I}$ is

$$\boldsymbol{V}_0 - \boldsymbol{V}_1 = [\boldsymbol{R}(\rho)\boldsymbol{I} - \boldsymbol{R}(\hat{\rho})\boldsymbol{I}] = [\boldsymbol{R}(\rho) - \boldsymbol{R}(\hat{\rho})]\boldsymbol{I} = \boldsymbol{D}\boldsymbol{I} \tag{3.1}$$

where $\boldsymbol{D} = \boldsymbol{R}(\rho) - \boldsymbol{R}(\hat{\rho})$. The current patterns that maximize the norm of the voltage difference for a unit current, $\|\boldsymbol{V}_0 - \boldsymbol{V}_1\| / \|\boldsymbol{I}\|$, are defined as the optimal current patterns. The voltage difference is an important term in the updating of impedance estimation, whose maximising can accelerate the convergence of a reconstruction algorithm and minimize the effects of measurement errors. Issacson [68] concluded that the optimal

current patterns are the eigenvectors corresponding to the largest eigenvalues of matrix $\boldsymbol{D}$.

The following algorithm can be used to obtain the best current pattern [42].

1) Guess a current density $\boldsymbol{I}_0(\theta)$ for which (to keep current in desired plane)

$$\int_0^{2\pi} \boldsymbol{I}_0(\theta)\, d\theta = 0 \tag{3.2}$$

and $|\boldsymbol{I}_0(\theta)| = 1$. Set $k = 0$.

2) Measure the voltage $\boldsymbol{V}_k^1(\theta) = \boldsymbol{R}(\rho_1)\boldsymbol{I}_k(\theta)$ that results from applying $\boldsymbol{I}_k(\theta)$ to the body whose impedance distribution is ρ_1.

3) Compute the voltage (see Chapter 5) $\boldsymbol{V}_k^0(\theta) = R(\rho_0)\, I_k(\theta)$ that would result from applying $\boldsymbol{I}_k(\theta)$ to a body with impedance ρ_0.

4) Compute the next estimate, $\boldsymbol{I}_{k+1}(\theta)$, as the best current to distinguish ρ_0 from ρ_1 by $\boldsymbol{V}_k^1(\theta) - \boldsymbol{V}_k^0(\theta)$.

$$\boldsymbol{I}_{k+1}(\theta) = \left|\boldsymbol{V}_k^1(\theta) - \boldsymbol{V}_k^0(\theta)\right| \tag{3.3}$$

5) If the changes in the $\boldsymbol{I}_k(\theta)$ are less than the measurement precision ε, i.e., $|\boldsymbol{I}_{k+1} - \boldsymbol{I}_k| < \varepsilon$ stop, otherwise increment k and go to step 2.

Using the algorithm described above, Gisser *et al* showed that after five iterations ($k \approx 5$), best current values converged rapidly toward their theoretically calculated values at $k \approx \infty$.

This procedure requires no advance knowledge of the impedance distribution and is numerically stable. However, it does require repetitive measurements from the real

object.

After finding the dominant eigensystem λ_0 and $\boldsymbol{I}_0$, another matrix $\boldsymbol{D}'$ is formed as follows:

$$\boldsymbol{D}' = \boldsymbol{D} - \lambda_0 \boldsymbol{I}_0 \boldsymbol{I}_0^T = \lambda_1 \boldsymbol{I}_1 \boldsymbol{I}_1^T + \lambda_2 \boldsymbol{I}_2 \boldsymbol{I}_2^T + \ldots + \lambda_{N-1} \boldsymbol{I}_{N-1} \boldsymbol{I}_{N-1}^T \tag{3.4}$$

Then using the same algorithm again with $\boldsymbol{D}'$ substituted for $\boldsymbol{D}$, one obtains the dominant eigensystem of $\boldsymbol{D}'$, i.e., λ_1 and $\boldsymbol{I}_1$. Repeat the above procedure to obtain the rest of the desired current distributions.

It should be kept in mind that *in vivo* applications of this algorithm have two major drawbacks.

1) The acquisition time is lengthy. In one case for a 32-electrode system it took 7.2 seconds. Many factors can cause impedance change during this data acquisition interval. If one images the human thorax, the heart rate is about one beat/s, and cardio-vascular ejection time is about 250 ms. The blood has a lower resistivity than other tissues in the chest, and thus ejection will change the impedance distribution during the cycle of data collection. The pulmonary ventilation cycle lasts about 8s. The air exchange and morphological changes also result in impedance change. Any of these changes during the data-collection period will result in distorted measurements and a blurred image. To all the previous problems, electrode artifacts resulted from subject movements, should also be added.

2) The explained procedure has to be repeated after each step of reconstruction algo-rithm. The reconstruction time for each step depends upon the reconstruction algo-rithm, computational method and computer facility. Therefore, to implement this

method, the measurement devices have to remain attached to the patient during the reconstruction algorithm. The impedance change during this period also introduces measurement errors.

3.5 Independent Current Patterns Method

First, it will be shown through linear algebra that any set of independent measurements can be used to synthesis optimal current patterns [22].

Suppose there are L electrodes and voltages due to an arbitrary current pattern $\boldsymbol{I}$ are to be synthesized from voltages that result from L - 1 orthogonal current patterns $\boldsymbol{T}^k$; $k = 1, 2, \ldots, L - 1$. Let $\boldsymbol{I}_l$ denote the current applied to the l^{th} electrode for $l = 1, 2, \ldots, L$, and $\boldsymbol{I} = (I_1, \ldots, I_L)^T$. From the conservation of charge

$$\sum_{i=1}^{L} I_i = 0. \tag{3.5}$$

Let V_l denote the voltage on the l^{th} electrode with the reference potential chosen so that

$$\sum_{i=1}^{L} V_i = 0. \tag{3.6}$$

Similarly, $\boldsymbol{V} = (V_1, \ldots, V_L)^T$. Denote the inner product of two vectors $\boldsymbol{A}$ and $\boldsymbol{B}$ by

$$\langle \boldsymbol{A}, \boldsymbol{B} \rangle = \sum_{i=1}^{L} A_i B_i. \tag{3.7}$$

Let $\boldsymbol{T}^k = \left(T_1^k, T_2^k, \ldots, T_L^k \right)$ for $k = 1, 2, \ldots, L - 1$ be orthogonal current patterns, i.e.,

$$\langle \boldsymbol{T}^k, \boldsymbol{T}^s \rangle = \delta_{k,s} = \begin{cases} 1 & \text{if} \quad k = s \\ 0 & \text{if} \quad k \neq s \end{cases}. \tag{3.8}$$

Then if $\boldsymbol{I}$ denotes an arbitrary current pattern

$$\boldsymbol{I} = \sum_{k=1}^{L-1} \langle \boldsymbol{I}, \boldsymbol{T}^k \rangle \boldsymbol{T}^k. \tag{3.9}$$

The voltage $\boldsymbol{V}$ that results from applying $\boldsymbol{I}$ is assumed to be linearly related to $\boldsymbol{I}$, i.e., there is an $L \times L$ matrix R such that $\boldsymbol{V} = \boldsymbol{RI}$.

In practice voltages are only measured with a finite number of digits or bits so the last equation holds only approximately for the real data. If measurements could be made with infinite precision then, the voltage due to any current could be synthesized from the voltages $\boldsymbol{V}^k$ due to the current $\boldsymbol{T}^k$. For $k = 1, 2, \ldots, L - 1$, apply $\boldsymbol{T}^k$ and measure $\boldsymbol{V}^k$. Thus $\boldsymbol{V}^k = \boldsymbol{RT}^k$ and

$$\boldsymbol{V} = \boldsymbol{RI} = \sum_k \langle \boldsymbol{I}, \boldsymbol{T}^k \rangle \boldsymbol{RT}^k = \sum_k \langle \boldsymbol{I}, \boldsymbol{T}^k \rangle \boldsymbol{V}^k. \tag{3.10}$$

When measurements are made with finite precision the measured voltages $\tilde{\boldsymbol{V}}$ due to $\boldsymbol{I}$ will in general differ from the synthesized voltages $\boldsymbol{V}$ given by the above formula.

The difference between measured voltages $\tilde{\boldsymbol{V}}$ and synthesized ones $\boldsymbol{V}$ could be unacceptably large, if the independent voltages are poorly selected. For instance, the neighboring method can be used to produce an independent set of measurements in a sufficiently short sampling time, and then the method described above is used to deduce voltages of optimal currents. But as already discussed, in the neighboring method, voltages measured far away from current injecting electrodes, are small and consequently their associated SNR would be too low. To implement this method, one has to use a suitable set of current patterns such as the trigonometric functions and Walsh functions patterns described in next sections.

3.5.1 Trigonometric Current Patterns

Trigonometric patterns T^k, $k=1, 2, \ldots, 31$ for a 32-electrode system are:

$$\begin{aligned} &for \quad k = 1, 2, \ldots, 16 \\ T_l^k &= A \cos[kl2\pi/32] \;, \quad l = 1, 2, 3, \ldots, 32 \end{aligned} \tag{3.11}$$

$$\begin{aligned} &for \quad k = 17, 18, \ldots, 31 \\ T_l^k &= A \sin[(32-k)l2\pi/32] \;, \quad l = 1, 2, 3, \ldots, 32 \end{aligned} \tag{3.12}$$

where k is current pattern number, A is amplitude (i.e. 5 mA) and l is electrode number.

As can be seen there are 31 patterns which yield 31×31 voltage measurements. It was mentioned that in a 32-electrode system there are at most 31×16 independent voltages. Although some of these measurements are redundant, there is no simple way to eliminate dependent ones. Issacson [68] derived these patterns as adaptive current patterns for a simple case when the inhomogeneity is centered in the background. Though obvious, it is worth mentioning that all electrodes will inject currents with the same frequency, but different amplitudes.

3.5.2 Walsh Function Current Patterns

The other set of current patterns mentioned, is known as Walsh function patterns [127]. Walsh function patterns are a complete orthogonal set of square pulses. For the case of a 32-electrode system ($l = 32$), Fig. 3.3 shows the first 16 out of 32 Walsh functions in Walsh order. When the signals in Fig. 3.3 uniformly sampled, one can formulate a matrix containing sampled values and the resulting matrix is called the Walsh-Hadamard matrix H. The Walsh-Hadamard matrix is symmetric and orthogonal, that is,

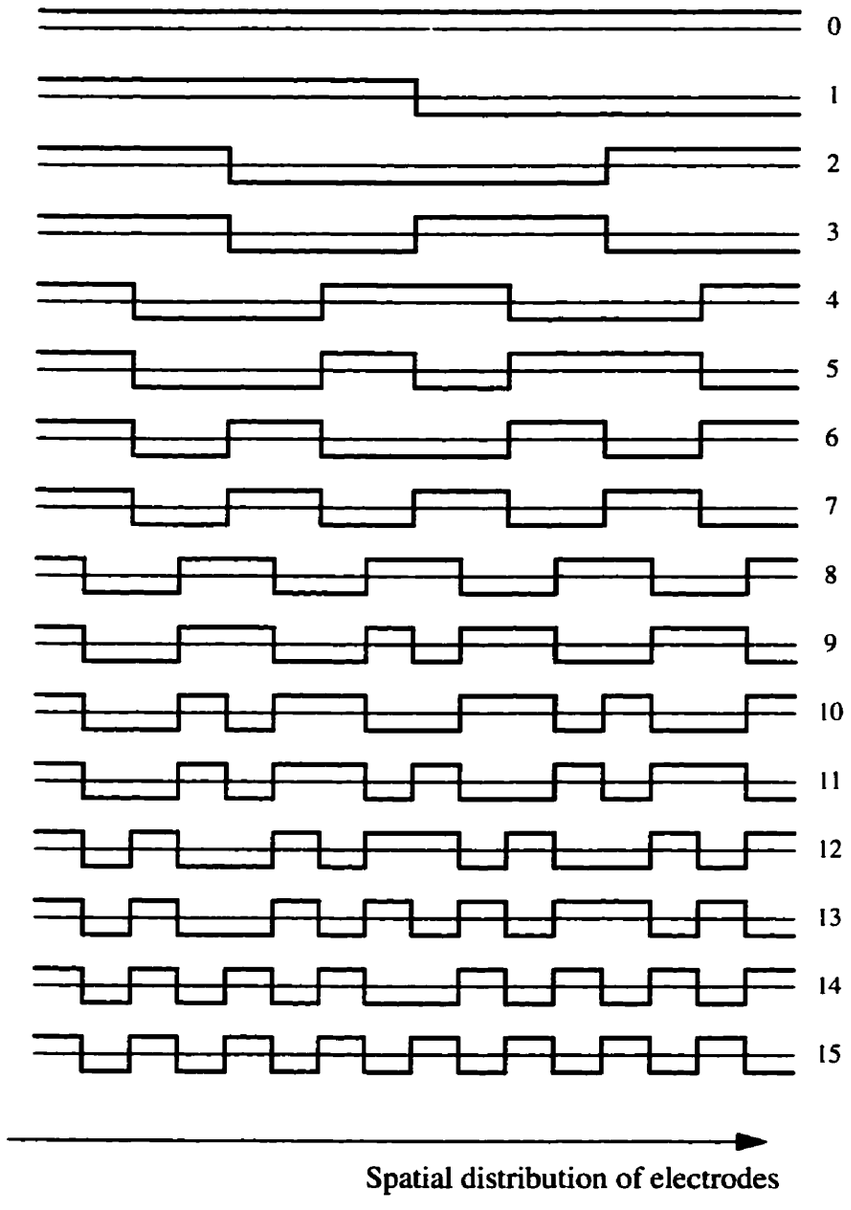

Fig. 3.3 First 16 Walsh functions

$$\boldsymbol{HH} = \boldsymbol{HH}^T = l\,\boldsymbol{I} = 2^n\,\boldsymbol{I} \qquad (n = \log_2 l, n \text{ is an integer}) . \tag{3.13}$$

The Walsh-Hadamard transform of a data sequence x is

$$\boldsymbol{x}_w = \frac{1}{l}\boldsymbol{H}\boldsymbol{x} \tag{3.14}$$

The inverse Walsh-Hadamard transform is

$$\boldsymbol{x} = \boldsymbol{H}\boldsymbol{x}_w \tag{3.15}$$

Even though both trigonometric and Walsh functions were introduced to be used in the adaptive current method, both can also be used for measurements without further synthesis. In this case, Walsh functions have an additional advantage that they require current sources with a constant amplitude, in contrast to the trigonometric functions, which need current sources with an adjustable amplitude. Note again, that in both trigonometric and Walsh functions, it is the spatial distribution of amplitudes that being described. I.e. sinusoidal wave current sources with the same frequency are still used.

4. RECONSTRUCTION ALGORITHMS

In previously reported reconstruction methods, usually only the resistive part of impedance is considered. This discussion starts with studying the Maxwell equations for time varying electromagnetic fields.

These equations in their point form are:

$$\nabla \times \mathbf{E} = -\frac{\partial \mathbf{B}}{\partial t} \tag{4.1}$$

$$\nabla \times \mathbf{H} = \mathbf{J} + \frac{\partial \mathbf{D}}{\partial t} \tag{4.2}$$

$$\nabla \cdot \mathbf{D} = \rho \tag{4.3}$$

$$\nabla \cdot \mathbf{B} = 0. \tag{4.4}$$

These four equations form the basis of all electromagnetic theory. They are partial differential equations and relate the electric and magnetic fields to each other and to their sources, charge and current density.

Auxiliary equations which relate **D** and **E**,

$$\mathbf{D} = \varepsilon \mathbf{E} \tag{4.5}$$

relate **B** and **H**,

$$\mathbf{B} = \mu \mathbf{H} \tag{4.6}$$

define conduction current density,

$$\mathbf{J} = \sigma\mathbf{E} \tag{4.7}$$

and define the convection current density in terms of the volume charge density ρ,

$$\mathbf{J} = \rho\mathbf{v} \tag{4.8}$$

are also required to define and relate the quantities appearing in Maxwell's equations.

It has been claimed [65,106] that as far as EIT is concerned, for frequencies below 10 to 30 MHz the magnetic field can be neglected. In that case from (4.2) one has:

$$\mathbf{J} + \frac{\partial \mathbf{D}}{\partial t} = 0. \tag{4.9}$$

After applying the $\nabla\cdot$ operator (divergence) to this equation and replacing $\frac{\partial}{\partial t}$ with $j\omega$ since sinusoidal time variations are being considered, one gets:

$$\nabla \cdot (\mathbf{J} + j\omega\mathbf{D}) = 0. \tag{4.10}$$

Substituting **J** and **D** from (4.5) and (4.7) then yields:

$$\nabla \cdot (\sigma\mathbf{E} + j\omega\varepsilon\mathbf{E}) = 0 \tag{4.11}$$

or

$$\nabla \cdot (\gamma\mathbf{E}) = 0 \tag{4.12}$$

where

$$\gamma = \sigma + j\omega\varepsilon. \tag{4.13}$$

The scalar electric potential ϕ and vector magnetic potential **A** are not directly necessary in electromagnetic field theory, but are extremely useful. They are related to the electric field and magnetic flux density respectively in the static case as:

$$\mathbf{E} = -\nabla\phi \quad \text{(static)} \tag{4.14}$$

$$\mathbf{B} = \nabla \times \mathbf{A} \quad \text{(dc)}. \tag{4.15}$$

(4.15) does not change for the time varying case, but (4.14) or the scalar electric potential is defined in time varying case as:

$$\mathbf{E} = -\nabla\phi - \frac{\partial \mathbf{A}}{\partial t}. \tag{4.16}$$

In general a vector can not be completely defined when only its curl is known. Additional information should also be given for this purpose i.e. its divergence. There is liberty in defining the divergence so one selects a simple definition. Two usual selections are:

$$\nabla \cdot \mathbf{A} = 0 \tag{4.17}$$

also known as Coulomb's gauge and:

$$\nabla \cdot \mathbf{A} = -\mu\varepsilon\frac{\partial \phi}{\partial t} \tag{4.18}$$

which is suitable for the wave equation.

When magnetic field is neglected, the relation between ϕ or potential and $\mathbf{E}$ or electric field can be written simply as:

$$\mathbf{E} = -\nabla\phi. \tag{4.19}$$

Then from (4.12) and (4.19)

$$\nabla \cdot \gamma(-\nabla\phi) = 0 \tag{4.20}$$

or

$$\nabla \cdot \gamma(\nabla\phi) = 0. \tag{4.21}$$

In the simplified case when only conductivity is considered, i.e., the permittivity is neglected, (4.21) becomes

$$\nabla \cdot \sigma(\nabla\phi) = 0 \tag{4.22}$$

or

$$\nabla \cdot \rho^{-1} (\nabla \phi) = 0. \tag{4.23}$$

(4.23) is the governing equation for our problem when only conductivity is considered. To solve an electromagnetic field problem, like any other differential equation, boundary conditions should be specified to have a unique solution. Here, these boundary conditions are:

$$\rho^{-1} \frac{\partial \phi}{\partial n} = \mathbf{J}_0 \tag{4.24}$$

wherever there is a current injection into the body. In this formula $\frac{\partial}{\partial n}$ means the outward normal derivative and $\mathbf{J}_0$ is the injected current. Also

$$\rho^{-1} \frac{\partial \phi}{\partial n} = 0 \tag{4.25}$$

wherever there is not an injecting current electrode in contact with the body.

4.1 Forward versus Inverse Problem

The definition of the forward problem for the EIT is shown in Fig. 4.1. Given the resistivity distribution within the object with boundary current density conditions on the

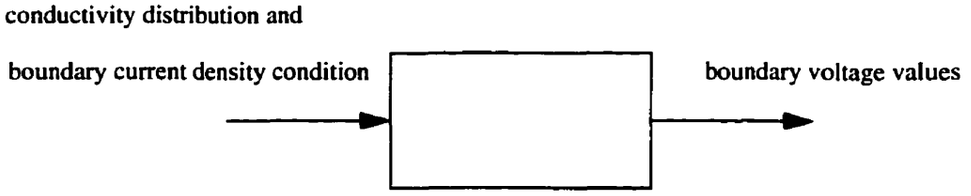

Fig. 4.1 The forward problem

surface of the object, the forward problem is to solve for the developed voltages on the surface of the object. Although one is interested only in boundary voltage values, internal voltage distributions are also found when numerical methods are used.

Figure 4.2 shows the definition of the inverse problem. Given the voltage and current density conditions on the boundary, the inverse problem is to solve for conductivity distribution within the object. Generally speaking the forward problem does not have analytical solution but in some trivial cases, nevertheless, it can be solved using numerical methods and does have a unique solution. On the other hand, the inverse problem does not have a unique solution and is solved either by iterative methods which require the solution of the forward problem at each step hence computationally extensive, or by non-iterative methods which although fast, only produce an approximate solution. Although only conductivity distribution was mentioned through this section, in general, permittivity distribution might also be involved.

4.2 Numerical Methods for the Forward Problem

Solving the forward problem, except for trivial cases, can not be managed through analytical methods. Using numerical methods in general is inevitable. There are many of such techniques to be used for this problem such as finite element method (FEM), finite difference method, method of moment, network approximation and transmission line matrix to name a few. Although, each of these techniques has its own advantages and limitations, some of them are more suitable for specific problems. The selection of a particular method, is based not only on the suitability from the strengths and limitations point of view, but factors such as software availability and user familiarity, are also very important.

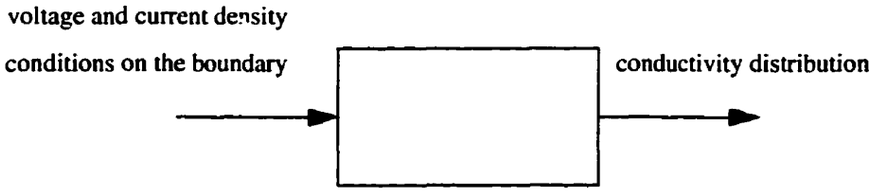

Fig. 4.2 The inverse problem

So far, FEM and network approximation are the most popular ones among researchers in EIT.

4.3 Dynamic versus Static Imaging

There are two different imaging techniques in EIT. One is dynamic (or difference) imaging and the other is static imaging. In dynamic imaging, the first boundary voltage data set is measured at time T_1 as a reference data set and then, at time T_2, another boundary voltage data set is measured. A dynamic image shows any changes in the resistivity distribution that occurred during the time between T_1 and T_2. Dynamic imaging is considerably simpler than static imaging since various errors are cancelled out by the subtraction process.

In static imaging, the absolute values of a cross-sectional resistivity distribution are reconstructed. Since current flow is a function of unknown resistivity distribution, the static impedance imaging problem is a nonlinear problem.

Major existing numerical methods for solving the inverse problem are to be considered in the rest of this chapter.

4.4 Backprojection Between Equipotential Lines

In this method the potential difference between two equipotential lines on the surface is backprojected to the resistivity value in the inside area between these two equipotential lines [43]

$$\rho = \rho_0 \frac{(V_i - V_j)_{measured}}{(V_i - V_j)_{expected}}. \tag{4.26}$$

The neighboring method which was discussed in Section 3.1 is used for data collection. For each projection angle a ρ is determined which is then averaged for all projection angles. A ramp filter is also employed to reduce the blurring inherent in backprojection.

4.4.1 Fast Filtered Backprojection Method

A fast filtered backprojection method has been proposed under the assumption that the unknown resistivity distribution is close to a known reference resistivity distribution.

When this assumption is valid, then there is an approximately linear relationship between the perturbation of the measured surface voltage gradients from those of the reference distribution and the logarithm of the resistivity perturbation from the reference distribution [35].

4.4.1.1 Computation of Equipotential Lines

The equipotential lines can be calculated by analytically solving Laplace's equation for circular, homogeneous, isotropic medium for given boundary conditions (under these assumption, (4.21) simplifies to $\rho^{-1}\nabla^2\phi = 0$ which is called Laplace's

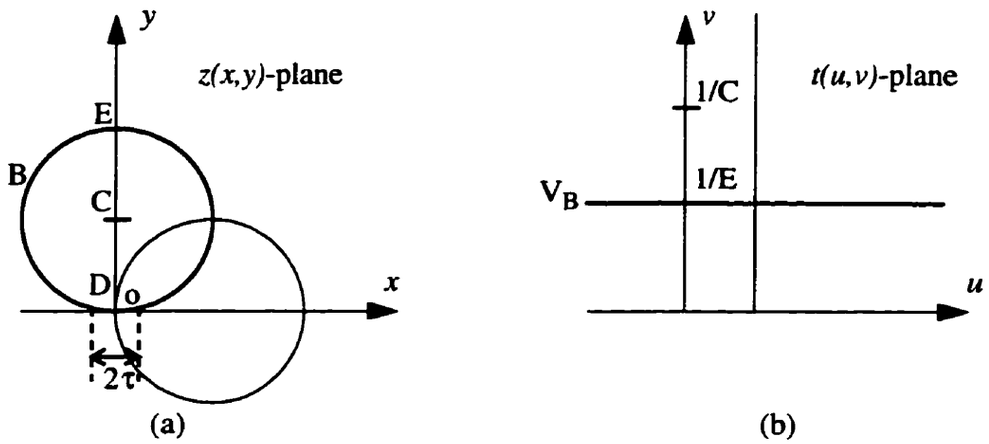

Fig. 4.3 Conformal mapping between a circular region and a semi-infinite region

equation). However, a different approximate method of finding the equipotential lines in developing the backprojection reconstruction algorithm has been used by Barber and Brown [7].

In the neighboring method the distance between two adjacent driving electrodes (2τ) is very small and these injecting current electrodes might be assumed as a current dipole. Then following conformal mapping, the $z(x,y)$ plane in Fig. 4.3(a) can be transformed into the $t(u,v)$ plane in Fig. 4.3(b).

$$x = \frac{u}{\left(u^2 + v^2\right)} \tag{4.27}$$

$$y = \frac{v}{\left(u^2 + v^2\right)} \tag{4.28}$$

$$u = \frac{x}{\left(x^2 + y^2\right)} \tag{4.29}$$

$$v = \frac{y}{\left(x^2 + y^2\right)} \tag{4.30}$$

Using this transformation, straight line (v=E) parallel to the u-axis in the t-plane is the transformation of the circle B in the z-plane. The points at $-\infty$ and $+\infty$ of the u-axis are transformation of the two end points of the current dipole((0 - τ, 0) and (0 + τ, 0)). Therefore, in the t-plane, two point charges with opposite polarity are placed at $-\infty$ and $+\infty$ of the u-axis. The straight lines parallel to the u-axis become field lines and are transformed into circles tangential to the x-axis at the point O in the z-plane. In the same way, equipotential lines which are perpendicular to the u-axis in the t-plane are transformed into the circular lines passing through the point O in the z-plane. If the dipole strength is m, then the equipotential lines are the lines passing through points at which

$$V = \frac{mx}{\left(x^2 + y^2\right)} \tag{4.31}$$

is constant. This method results in significant error close to the electrodes when the distance between the current injecting electrodes (2τ) is not sufficiently small.

4.4.1.2 Backprojection along Equipotential Lines

Assume $V_u(\Phi)$ is the potential measured at a point Q(Φ) on the boundary B of a homogeneous resistivity (ρ_u) medium S as shown in Fig. 4.4(a). Similarly assume $V_m(\Phi)$ = $V_u(\Phi) + \Delta V(\Phi)$ is the potential measured at the same point after the resistivity of the medium has changed from ρ_u to $\rho_u + \Delta\rho_u$. The change in the boundary voltage is related to the change in the resistivity of the medium. Therefore,

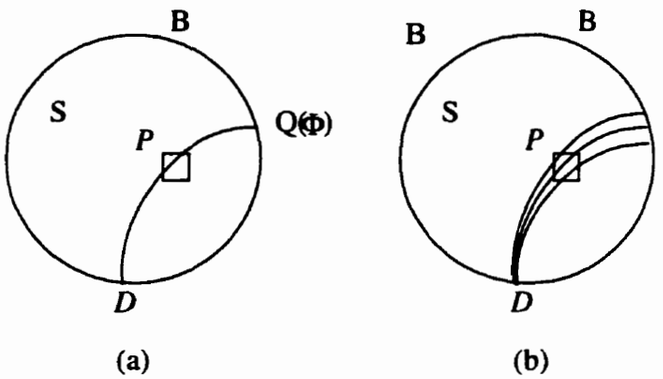

Fig. 4.4 Backprojection of boundary voltage measurements.

$$\frac{V_m(\Phi)}{V_u(\Phi)} \approx \frac{\rho_u + \Delta\rho}{\rho_u}. \tag{4.32}$$

Assume that $\Delta V(\Phi) \ll V_u(\Phi)$, $\Delta\rho_u \ll \rho_u$, and therefore the shape of the equipotential lines do not change significantly. Upon taking the natural logarithm of both sides the above equation becomes

$$\frac{\Delta V(\Phi)}{V_u(\Phi)} \approx -\frac{\Delta\rho}{\rho_u}. \tag{4.33}$$

Therefore, for the image value of the pixel P which lies on the equipotential line ending at the point $Q(\Phi)$, the normalized boundary voltage change is backprojected. Assuming $\boldsymbol{g}(D)$ is a vector of normalized boundary voltage change for drive pair D and p is the image value of the pixel P, then,

$$p = \boldsymbol{w}(PD) \cdot \boldsymbol{g}(D) \tag{4.34}$$

where $\boldsymbol{w}(PD) = [0, 0, \ldots, w_j, 0, \ldots, 0]$ is the backprojection vector for the pixel P, the drive

pair D, and the jth voltage measuring electrode pair. w_j is a weighting factor for angular uniformity and will be described in the next subsection. Since Eq. (4.34) holds for all pixels,

$$\boldsymbol{p}(D) = \mathbf{W}(D)\,\boldsymbol{g}(D) \tag{4.35}$$

where $\boldsymbol{p}(D)$ is a vector of image values of all pixels and $\mathbf{W}(D)$ is a matrix whose rows are $\boldsymbol{w}(PD)$.

A pair of current injection electrodes (D) is not actually a dipole due to the distance between them not being sufficiently small. To get better results the dipole is moved by small angles and new equipotential lines originating from the new dipoles and passing through the pixel P are found. Then, different boundary potentials at the ending points of the new equipotential lines are backprojected into the pixel. Moreover, since more than one equipotential line passes through a pixel due to the finite size of the pixel (see Fig. 4.4 (b)), corresponding boundary potentials are also appropriately backprojected into the pixel.

For a 16 electrode system, there are 16 drive pairs and the final image $\boldsymbol{p}$ is obtained using this formula:

$$\boldsymbol{p} = \sum_{D=1}^{16} \boldsymbol{p}(D) = \mathbf{W}\boldsymbol{g}. \tag{4.36}$$

4.4.1.3 Weighting Factors: w_j

Except for the pixel at the center, the equipotential lines are not circularly symmetric. Therefore, the weights should be different for all pixels other than the middle one.

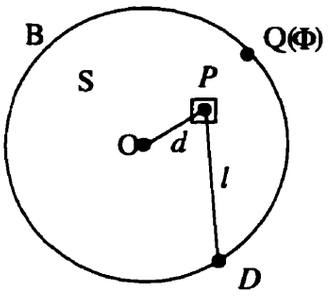

Fig. 4.5 Computation of backprojection weight.

Based on the conformal mapping of a central point and an offset point [79], the weights w_j is computed using:

$$w_j = \frac{l^2 - d^2}{l^2} \tag{4.37}$$

where l and d are shown in Fig. 4.5.

4.4.1.4 Filtering

The spatial resolution is position dependent because it depends on the location of an object in the circular medium. In order to minimize the artifacts due to the severe position dependence of the spatial resolution of the reconstructed image, Seagar *et al* [114] developed a restoration filter empirically. A nonlinear radial transformation is applied to the image to make the filtration problem position independent. Then the image is filtered with a position-dependent resolution restoring filter. Finally, the inverse radial transform is applied to the result. The nonlinear radial transform and inverse transforms

are

$$s = \tanh(r) \tag{4.38}$$

$$r = 0.5 \ln \frac{1+s}{1-s} \tag{4.39}$$

where r is the radial distance in the original image and s is the radial distance in the transformed image.

The filtering operation can be combined with backprojection since the reconstruction algorithm is linear. Let $\mathbf{E}$ denote the filtering operation and $\boldsymbol{q}$ be the final reconstructed image. Then,

$$\boldsymbol{q} = \mathbf{E}\boldsymbol{p} = \mathbf{E}\mathbf{W}\boldsymbol{g} \tag{4.40}$$

which is called the filtered backpropagation method.

4.4.2 Iterative Equipotential Lines Method

The equipotential line method is a linear reconstruction method and the results are produced in a non iterative scheme after corrections have been made for all measurements. An iterative method based on the equipotential line method has been proposed by Yorkey *et al* [132]. This method shows better performance over the non iterative one. Since the original equipotential lines are no longer valid after a single correction of the resistivity, equipotential lines have been iteratively calculated after each projection angle.

Iteration is essential in producing static images by the backprojection between equipotential lines method. This method has been implemented by Ider *et al* [66,26] where they used the finite element method (FEM) to solve the forward problem and determined the position of electrodes using 16 ultrasonic transducers. For a 16-electrode system and

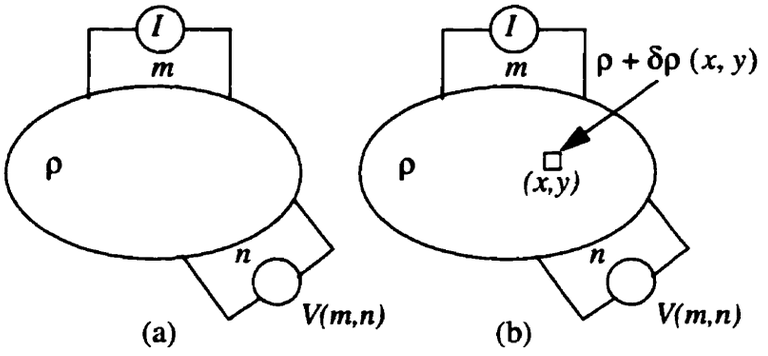

Fig. 4.6 Measuring resistance using a four electrode system for (a) a homogeneous object and (b) the same object as before but with a changed resistance in a discretized element [76].

12 bit A/D, static images with a conductivity contrast better than 20% and about 10% spatial resolution have been reconstructed.

4.4.3 Backprojection Method Using Sensitivity Coefficients

In Fig. 4.6, assuming the $\delta\rho\ (x, y)$ is small, a sensitivity coefficient is defined as

$$S_{m,n,x,y} = \frac{\delta V(m,n)}{\delta\rho\ (x, y)} = \int_e \nabla\phi_m \cdot \nabla\phi_n dS \tag{4.41}$$

where e denotes the integration over the area of the element.

It has been found that the backprojection between equipotential lines method is equivalent to the sensitivity matrix, built based on the Eq. (4.41) when all the elements but the diagonal ones are neglected [24]. It, therefore, has been suggested that utilizing other matrix elements should improve the backprojection between equipotential lines method, because the other elements are not negligible. Thus, a backprojection algorithm has been

proposed that uses all sensitivity coefficients as weights [76].

The sensitivity matrix can be computed using FEM in the same way as the Jacobian matrix is computed in the modified Newton-Raphson method. An an alternative, it can be computed from the analytic solution of Laplace's equation for the homogeneous resistivity distribution. When the sensitivity matrix is in hand the pixel value *P(x,y)* can be computed by [76]

$$P(x,y) = \sum_{m=1}^{M} \sum_{n=1}^{N} S_{m,n,x,y} \ln\left[\frac{V'(m,n)}{V(m,n)}\right] \tag{4.42}$$

in this single-pass reconstruction algorithm.

Although this algorithm would produce less accurate images compared to an iterative nonlinear reconstruction algorithm, proper use of the sensitivity matrix will improve the image quality of the backprojection method.

4.4.4 Dual Frequency Imaging

As mentioned before the backprojection method is a dynamic imaging method that shows the difference in conductivity of the object between two time frames. It has been suggested to use the measurement at one frequency as a reference to a measurement at another frequency [50,53]. The rationale for this method is that the dielectric constant and electrical conductivity of human tissues change depending on the frequency (see Table 2).

Dual-frequency imaging can also be used with other reconstruction algorithms.

4.4.5 Discussion: Backprojection Method

The fast filtered backprojection method can not produce static images. Its other

constraints include assuming that the object has a circular boundary with equally spaced electrodes, that the object is two dimensional, and that the resistivity distribution to be reconstructed is close to the reference resistivity distribution. In spite of those constraints, this method rapidly produces useful difference images and is being used in various clinical applications.

This method is fairly immune to random electrode placement errors, however, sometimes it might be very difficult to keep the same electrode placement between the measurements of the two data sets which renders no use for the reconstructed image [8].

Using the iterative backprojection method provides more accurate images compared to the noniterative method but at the expense of more computation time. Using all sensitivity values in the sensitivity matrix improves the image quality of the backprojection method. Dual-frequency imaging also provides a kind of static image.

4.5 Perturbation Method

Unlike other methods, the perturbation method is based on applying voltage and measuring current.

The current change is calculated using FEM when the resistivity of one element is slightly altered. This percent change in current is backprojected using the perturbation matrix [71,73,132].

4.5.1 Formation of Perturbation Matrix

Each pattern of voltage application is called a projection angle. For each projection angle, the currents of the current-measuring electrodes are calculated using FEM for a

homogeneous distribution, then, the resistivity of one element is increased by a factor of ten and currents are calculated again. This is done for all projection angles and the amount of the change in exit currents is normalized with respect to the current-measuring electrode for the projection angle. Finally the perturbation matrix $\mathbf{T}(E \times C \times P)$ is calculated where E is the number of elements, C is the number of current electrodes, and P is the number of projection angles. Other practical considerations include storing only the integer portion of T_{ijl} to reduce the storage requirement and permitting the corrections only within the central region by setting the sensitivity value of the outermost elements to zero. Otherwise, the reconstruction diverges since the sensitivity values of the peripheral elements are at least an order of magnitude larger than those at the center.

4.5.1.1 Backprojection after Each Projection Angle

The percent change in exit currents due to the object is backprojected after measuring exit currents with an object for each projection angle as follows:

$$\rho_i^n = \rho_i^{n-1} + k \frac{\sum_{j=1}^{C} RC_{jl}^n T_{ijl} \rho_i^{n-1}}{\sum_{j=1}^{C} |T_{ijl}|} \tag{4.43}$$

where k is the overrelaxation factor, T_{ijl} is the sensitivity of the ith element in the jth current electrode at the lth projection angle, and RC_{jl}^n is the percent difference between the predicted and actual exit current at the jth current electrode for the lth projection angle in the nth iteration.

Yet better convergence can be obtained by correcting the resistivity values after

acquiring all the data from all projection angles [52].

$$\rho_i^n = \rho_i^{n-1} + k \frac{\sum_{i=1}^{P}\sum_{j=1}^{C} RC_{jl}^n T_{ijl} \rho_i^{n-1}}{\sum_{i=1}^{P}\sum_{j=1}^{C} |T_{ijl}|} \tag{4.44}$$

This is similar to the simultaneous iterative reconstruction technique (SIRT) in the X-ray CT reconstruction technique whereas the previous approach is similar to the algebraic reconstruction technique (ART) [41,110].

4.5.2 Modified Perturbation Method

It has been found that the larger the element size, the closer to the current-measuring electrode, and the lower the background resistivity, the higher the sensitivity value [73]. Based on this fact, the perturbation method has been modified in such a way that the resistivity adjustment during the backprojection is based on a linearly decreasing function of distance from the current-measuring electrode. Columns of elements have been defined for each electrode pair and each projection as shown in Fig. 4.7. Backprojection along these columns is performed by updating the resistivity,

$$\rho_i^n = \rho_i^{n-1} k\left(\frac{C_{2pd} - C_{1pd}}{m-1} i + C_{1pd}\right) + \rho_i^{n-1} \tag{4.45}$$

where m is the number of elements in the column, i is the element position in the column (between 0 and m), k is the overrelaxation factor, ρ_i^n is the resistivity of the ith element in the nth iteration and C_{1pd}, C_{2pd} are the percent differences between calculated and

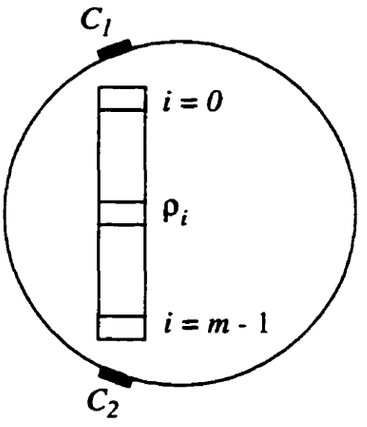

Fig. 4.7 C_1 and C_2 are current-measuring electrodes, i is the position number, m is the number of elements in the column and ρ_i is the resistivity of element i.

measured currents at electrodes C_1, C_2.

Although the perturbation method is based on a homogeneous object with only the resistivity of one element different from that of the background, it has been found that updating the perturbation matrix after each iteration does not improve the performance of the method [132].

4.6 Double Constraint Method

The double constraint method solves Poisson's equation by the FEM using Neumann boundary conditions and Dirichlet boundary conditions successively in each iteration.

Starting from a homogeneous resistivity distribution, the resistivity distribution is updated in each iteration by using the compatibility between the two boundary conditions

[125]. This method consists of three main steps.

1) Calculation of voltage, V and current density, $\mathbf{J}$ with Neumann boundary conditions.

FEM can be used to solve the Poisson equation for the voltage values inside the region due to the injection currents and to find the voltages at each node. Knowing the voltages, electric field density may be calculated using

$$\mathbf{E} = -\nabla V. \tag{4.46}$$

When electric field density is determined, the electric current density $\mathbf{J}$ in each element is given by

$$\mathbf{J} = \sigma\mathbf{E} = -\sigma\nabla V = -\rho^{-1}\nabla V \tag{4.47}$$

where the σ is the conductivity and ρ is the resistivity of the element.

Until the error between the calculated surface voltages and the measured voltages satisfies the stopping criterion, the resistivity distribution used in this step would be different from the actual resistivity distribution.

The error between the calculated surface voltages and the measured voltages is calculated and if this error is smaller than the stopping criterion, then the final image is presented, otherwise the next step is performed.

2) Calculation of voltage, V and $-\sigma\nabla V$ with both Neumann and Dirichlet boundary conditions.

The Poisson equation is again solved for the voltage values inside the region using the measured surface voltage values as the Dirichlet boundary condition while using the same Neumann boundary condition. The resulting voltage values inside the region should be a better estimate because the measured surface voltages used as boundary

data, change the voltage values at each node in correct direction.

3) Calculation of resistivity.

Considering that the Poisson equation using one boundary condition (Neumann or Dirichlet) has unique solution, one can solve the equation for the voltage values using one type of boundary data, and then calculate the other type of boundary data from the solution. The boundary conditions should be compatible for a given resistivity distribution, however, two solutions from previous methods are not identical since the actual resistivity distribution is not known.

Here a new resistivity distribution is calculated from the minimization of the squared error between the electric current density of the previous methods. The following equation defines the squared residual sum, R,

$$R = \sum_i \iiint_{v_i} (\mathbf{J}_i + \sigma_i \nabla V_2) \cdot (\mathbf{J}_i + \sigma_i \nabla V_2)\, dv \tag{4.48}$$

where v_i and dv denote the volume integral over the element i, $\mathbf{J}_i$ is the calculated electric current density in the element i from the first method and $\sigma_i \nabla V_2$ is the electric current density in the same element from the second method.

The new resistivity is calculated from the minimization of the squared residual sum, assuming homogeneous resistivity within one element,

$$\frac{\partial R}{\partial \sigma_i} = \iiint_{v_i} (2\mathbf{J}_i \cdot \nabla V_2 + 2\sigma_i \nabla V_2 \cdot \nabla V_2)\, dv = 0 \tag{4.49}$$

and

$$\sigma_i = \frac{1}{\rho_i} = \frac{-\iiint_{v_i} J_i \cdot \nabla V_2 dv}{\iiint_{v_i} \nabla V_2 \cdot \nabla V_2 dv}. \tag{4.50}$$

A modified version of double constraint method has been also proposed which is more efficient for practical calculation since the minimization of the relaxed foundation on a coarse mesh is roughly equivalent to the minimization of the original one on a much finer mesh [75].

The effect of the Dirichlet boundary conditions on the voltage values in the first step is small and therefore, the method needs many iterations [126]. However it has been claimed that this method is not subject to matrix ill-conditioning compared to the method where minimization is applied to the boundary voltage error.

4.7 Newton-Raphson Method

The Newton-Raphson algorithm is an iterative reconstruction algorithm specifically developed for nonlinear problems.

It is one of the most theoretically sound algorithms used in EIT. This method shows good convergence characteristics and reconstructs almost perfect images when no error is involved in the modelling and measurement. However when modelling error and measurement noise are present and when the number of elements (pixels) are large for good spatial resolution, the performance of this method deteriorates rapidly and produces noisy images or may even diverge. Furthermore, when a large number of elements are used, the image reconstruction requires an unreasonably long computation time [130,131].

4.7.1 The Measure of Error

The Newton-Raphson method is based on minimizing an objective function which in turn is made of a measure of error. A straightforward way to measure the error would be to compare the real resistivity distribution with the reconstructed one, but, the real distribution is unknown. As an alternative the difference between measured voltages and those based on the reconstructed distribution has been taken as the measure of error. If the voltage responses of the reconstructed resistivity distribution match those of the real distribution, we claim that the reconstructed distribution is the desired answer.

Although there are many ways to define the objective function based on this measure of error, usually it is defined as the equally weighted mean square difference between the measured and estimated voltage responses [130],

$$\Phi(\rho) = (1/2)\,(\boldsymbol{f}(\rho) - \boldsymbol{V}_0)^T(\boldsymbol{f}(\rho) - \boldsymbol{V}_0) \tag{4.51}$$

where $\boldsymbol{V}_0$ is the measured voltage, $\boldsymbol{f}(\rho)$ the estimated voltage for a resistivity distribution ρ, and superscript T means transpose.

However the problem can be described in a general sense as follows:

$$Min_{\rho} Max_{\boldsymbol{c},\boldsymbol{e}} \Phi(\rho, \boldsymbol{c}, \boldsymbol{e})$$

where $\Phi(\rho, \boldsymbol{c}, \boldsymbol{e})$ is the objective function (error signal) which indicates the difference between the resistivity distribution of the model and that of the subject, ρ is the resistivity distribution of the model, $\boldsymbol{c}$ is the injection current pattern, and $\boldsymbol{e}$ is the electrode configuration. An efficient EIT system requires a measurement method including injection current patterns, electrode size, position, etc., which maximizes the objective function or distinguishability [68]. Given the measurement method, we need an algorithm by which we

adjust the resistivity distribution of the model so that the objective function is minimized.

4.7.2 Formulation for the Newton-Raphson Method

To find a ρ which minimizes Φ in (4.51), set its derivative to zero, i.e.,

$$\Phi'(\rho) = [f'(\rho)]^T (f(\rho) - V_0) = 0 \tag{4.52}$$

where $[f'(\rho)]_{ij} = \dfrac{\partial f_i}{\partial \rho_j}$, and is called the Jacobian matrix.

Take the Taylor series expansion of $\Phi'(\rho)$ about a point ρ^k and keep the linear terms

$$\Phi'\left(\rho^{k+1}\right) = \Phi'\left(\rho^k\right) + \Phi''\left(\rho^k\right)\Delta\rho^k = 0 \tag{4.53}$$

where

$$\rho^{k+1} = \rho^k + \Delta\rho^k. \tag{4.54}$$

The term Φ'' is called the Hessian matrix, expressed as

$$\Phi'' = [f']^T f' + [f'']^T \{I \otimes [f - V_0]\} \tag{4.55}$$

where $\otimes$ is the Kronecker matrix product. Since f'' is difficult to calculate and relatively small omit the second term in the above equation. Therefore,

$$\Phi'' = [f']^T f' \tag{4.56}$$

Substitute Eqs. (4.56) and (4.52) into Eq. (4.53), and find the updating equation for ρ

$$\Delta\rho^k = -\left[f'\left(\rho^k\right)^T f'\left(\rho^k\right)\right]^{-1}\left[f'\left(\rho^k\right)\right]^T\left[f\left(\rho^k\right) - V_0\right]. \tag{4.57}$$

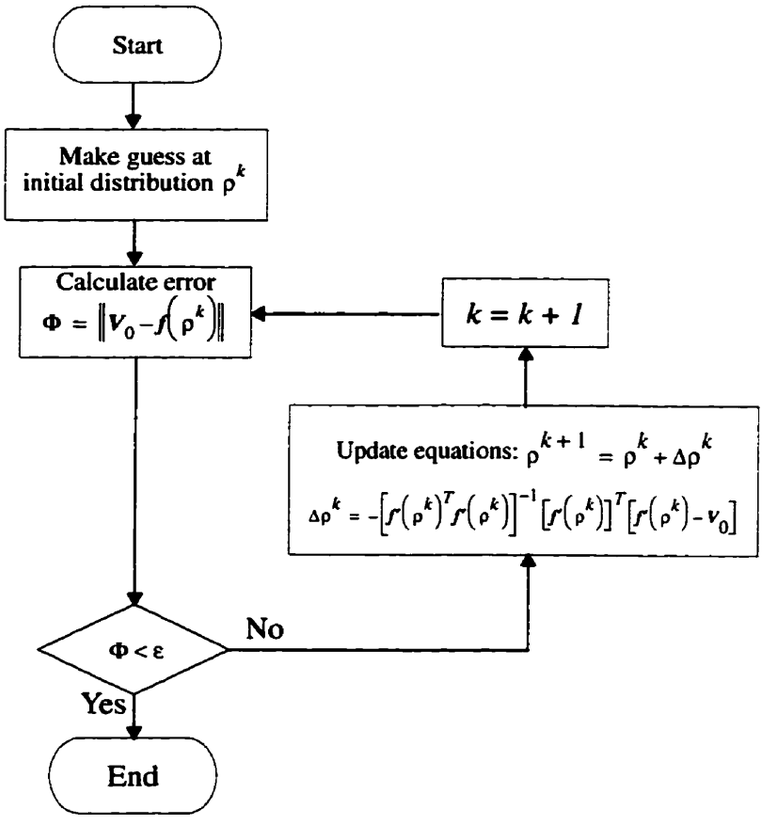

Fig. 4.8 The Newton-Raphson algorithm performs k iterations to minimize the mean-squared error Φ.

The flow chart of the algorithm is shown in Fig. 4.8. The theoretical voltage response for the given current distribution using the finite-element method are calculated for an initial distribution. These voltages are subtracted from measured ones to obtain the objective function. If less than a criterion error, the initial distribution is taken as the desired distribution. If not, the distribution is updated using Eq. (4.57). The above procedure is repeated until the stopping criterion is met.

Assuming f to be proportional to ρ, Φ would be a quadratic function of ρ. Its derivative Φ' would be a linear function. For the assumed distribution ρ^k, the error Φ is calculated to determine if it is less than stopping criterion ε. If not, the slope of Φ' is found, and then the assumed distribution along the direction opposite to the slope is updated. In this linear case, the solution can be found in one step, as $\rho = \alpha (V/I)$, where α is a constant which measures the geometric shape of the medium.

The vector $f(\rho)$ denotes a collection of all voltage data, which should contain sufficient information about the resistivity distribution. To solve this problem the number of independent data measurements should be equal to or greater than the number of pixels of the image. This usually requires one to make several sets of measurements, with each set being the voltage response of one current distribution, called a projection.

The calculation of f and f' requires the use of the FEM or other methods to solve the forward problem. A system function is established to describe the relationship among resistivity distribution, voltage and current, for each current distribution. The system function is solved to obtain its voltage response v_i, $i = 1$ to n, where n is the number of projections. The voltages from all projections are stacked to form f, i.e., $f = \left[v_1^T \; v_2^T \ldots v_i^T \ldots v_n^T\right]^T$.

Equation (4.57) has a step size of unity. However, the step size depends on the application, and is usually chosen less than one to achieve guaranteed convergence. If the step size is too big, even though the process may show fast convergence during the first few iterations, undesired oscillation occurs in the neighborhood of the solution.

Although in EIT the voltages are nonlinear functions of the resistivity and

therefore the Newton-Raphson procedure may result in a local minimum, the problem can be avoided by making an appropriate initial guess. In biomedical applications, there is sufficient prior knowledge to provide a good initial guess.

4.7.3 The Ill-Conditioning Problem

The n roots of the characteristic polynomial of an n by n matrix A are called its eigenvalues.

If the ratio of the maximal and the minimal eigenvalues is very large, then the matrix is considered to be ill-conditioned or ill-posed.

The inversion of the normalized Jacobian matrix shown in Eq. (4.57) is a part of the updating procedure. Depending upon the resistivity distribution and data collection method, the matrix could be very ill-conditioned. If the current is extremely small within some region, the resistivity change does not yield much voltage change at the boundary, and this results in ill-conditioning.

Ill-conditioning causes the matrix inversion to be very inaccurate and also the updating of Eq. (4.57) to be very sensitive to measurement error which both factors result in large reconstruction errors.

Using the adaptive method in data collection which was discussed in section 3.4 can considerably improve the situation.

4.8 Compensation Theorem Method

The compensation theorem method is essentially the Newton-Raphson method which uses the compensation theorem to calculate the Jacobian matrix.

The following subsections describe this method in details.

4.8.1 Sensitivity Theorem

The sensitivity theorem proposed by Geselowitz states how the voltage changes as a result of resistivity change. The impedance network shown in Fig. 4.9 displays the subject of the theorem. Applying a current source c_k to port k, results in the voltage V_i at port i. The discrete version of the sensitivity theorem [88,90] states that if the conductance y_j of port j changes to $y_j + \Delta y_j$, the voltage change at port i is

$$\Delta v_i = -c_k \Delta y_j z_{ij'} z_{kj} \tag{4.58}$$

where $z_{ij'}$ and z_{kj} are the transfer impedances between the described ports, j' denoting the changed port.

4.8.2 The Compensation Theorem Method

When using FEM method to solve the forward problem, each element is made of L resistors with the resistivity value being $\rho_j s_l$, $l = 1$ to L, where ρ_j is the resistivity value and s_l is the FEM coefficient. A change in conductivity of an element causes changes of L resistor values, therefore, the corresponding voltage change at port i is the summation of the changes due to individual resistivities is as shown in the following equation:

$$\Delta v_i = -c_k \sum_{l=1}^{L} \Delta y_j(l)\, z_{ij'}(l)\, z_{kj}(l)\ . \tag{4.59}$$

After some manipulations one can derive [88,90]

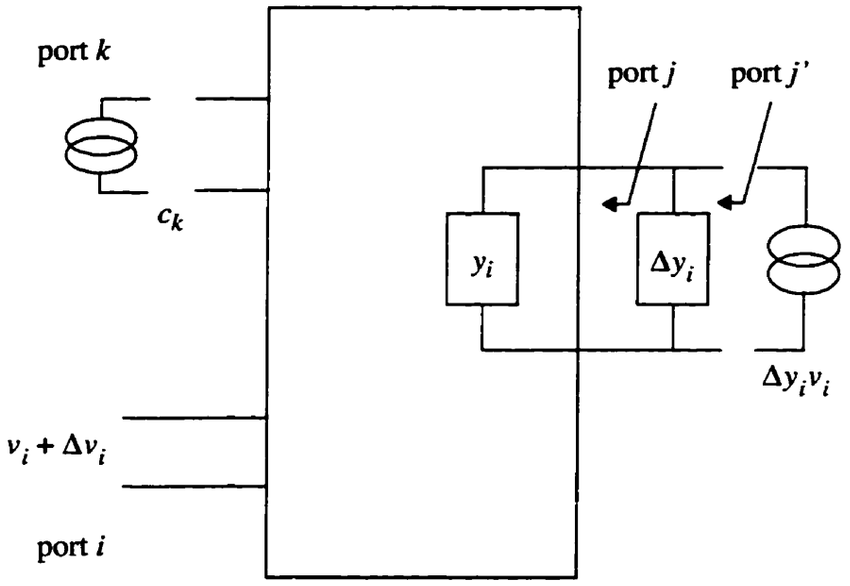

Fig. 4.9 When a current source is applied to port k and an admittance Δy_i to port j, the compensation theorem explains how to calculate the resulting voltage at port j by removing the current source and applying a particular current source to port j'. This theorem can be used to calculate the Jacobian matrix more efficiently.

$$\frac{\partial v_i}{\partial \rho_j} = \sum_{k=1}^{M} \frac{1}{c_k \rho_j^2} \sum_{l=1}^{L} s_l v_{ij}(l)\, v_{kj}(l), \tag{4.60}$$

which yield the entries of the Jacobian matrix in Eq. (4.52).

4.9 Comparison of Covered Reconstruction Methods

Yorkey *et al* [129] used computer simulations to compare the performance of the different nonadaptive algorithms. In their study, data was produced through a computer phantom by solving the forward problem and no noise was added to the measurements. By

these assumptions a comparison can be made between these methods, but it should be kept in mind that in a real case when noise is present in measurements, the situation could be quite different.

The Newton-Raphson method and compensation theorem algorithms have the best convergence while other methods do not converge in all cases and actually sometimes diverge.

From the computation time point of view, the standard Newton-Raphson method takes a long time for each iteration, approximately four times that of the compensation theorem, while both methods require the same number of iterations. The perturbation method needs the most time for each iteration, while, the iterative equipotential line method, the double constraint method and the equipotential line method need much less time for each iteration. If neglecting the part of computations that are not repeated in all iterations but the first one then in decreasing order the computation time for each iteration is; iterative equipotential line, double constraint method, equipotential line method, perturbation method, compensation theorem method and finally the standard Newton-Raphson method.

4.10 Regularization Method

The matrix $[f']^T[f']$ that should be inverted in the Newton-Raphson method is an ill-conditioned matrix as well as a complicated function of current, voltage, and the unknown resistivity distribution. This degrades the performance when the data is contaminated with measurement error. Improving the conditioning of the matrix by choosing a measurement method for a resistivity distribution impedance is a very difficult task, since

no explicit relationship can be seen. As an alternative, Hua *et al* [63] used the regularization method to improve its conditioning.

The objective function to be minimized in the regularization of the Bayesian technique [47] is

$$\Phi(\rho) = (1/2)\,(\boldsymbol{f}(\rho) - \boldsymbol{V}_0)^T(\boldsymbol{f}(\rho) - \boldsymbol{V}_0) + \lambda J(\rho)\,. \tag{4.61}$$

The first term is the same as in Eq. (4.51), while the second term, $J(\rho)$ takes the prior information into account. The smoothing parameter λ controls the relative weighting given to the prior information. Here $J(\rho)$ is taken to be a quadratic function of ρ, i.e., $J(\rho) = \rho^T\Sigma\rho$, where Σ is a positive definite matrix, depending on the form of prior information. Therefore, the objective function can be rewritten as

$$\Phi(\rho) = (1/2)\,(\boldsymbol{f}(\rho) - \boldsymbol{V}_0)^T(\boldsymbol{f}(\rho) - \boldsymbol{V}_0) + \lambda\rho^T\Sigma\rho\,. \tag{4.62}$$

The extremum of the above objective function can be reached by updating the resistance distribution as

$$\rho^{k+1} = \rho^k + \Delta\rho^k \tag{4.63}$$

where

$$\Delta\rho^k = -\left[\boldsymbol{f}\left(\rho^k\right)\boldsymbol{f}'\left(\rho^k\right) + 2\lambda\Sigma\right]^{-1}\left[\boldsymbol{f}'\left(\rho^k\right)\right]^T\left[\boldsymbol{f}\left(\rho^k\right) - \boldsymbol{V}_0\right]. \tag{4.64}$$

Equation (4.66) differs from (4.57) only in the matrix to be inverted. Since Σ is a positive-definite matrix with λ nonnegative, the matrix to be inverted should have a better conditioning than that without regularization. In other words, the prior knowledge helps to stabilize the system.

If the solution is known to be bounded but fluctuating, then the $J(\rho)$ in the

second term of Eq. (4.63) can be taken as $\|\rho\|^2$.

Table 4: Summary of some EIT systems [124]

		Madison	**Rensselear**	**Sheffield**	**Barcelona**
Data acquisition	Number of electrodes	32	32	16	16
	Frequency	50 kHz	15 kHz	50 kHz	10-100 kHz
	C. channel	32	32	1	1
	V. channel	1	1	1	16
	Accuracy	12 bit	12 bit	16 bit	16 bit
	2 or 4 electrode	4	2	4	4
Data collection	Method	Optimal currents	Optimal currents	Neighboring method	Neighboring method
	Unit time	500 μs	16 ms	380 μs	400 μs
	Frame time	480 ms	15 s	100 ms	5.2 ms
Forward solution		FEM	Analytic	Analytic	Analytic
Inverse solution	Algorithm	N-R with regularization	N-R single step	Weighted backprojection	Weighted backprojection
	Iteration	10	1	1	1
Contact impedance		FEM	Lumped model	V not measured on I electrode	V not measured on I electrode
Image type		Static	Static	Dynamic	Dynamic
Spatial resolution	Simulation	10%	5%	10%	10 - 20%
	Phantom	10%	10%	10%	10 - 20%
	In vivo	Progress	10 - 20%	10 - 20%	10 - 20%

To handle the ill-conditioning, Murai and Kagawa [88] have applied the SVD (singular value decomposition) method while, Akaike [4] implemented the information criterion, and Yorkey *et al* [130] used the Marquardt [83] method as Bard [10] has shown that the Marquardt method is more advantageous than the SVD and other methods. The Marquardt method is actually a regularization method corresponding to $J(\rho) = \|\rho\|^2$, with the weighting coefficient λ adjusted at each iteration by the algorithm.

4.11 Summary of EIT Systems

Table 4 shows the main specifications of EIT systems developed by various research groups in this field. In this Table, unit time is the time for one voltage measurement and frame time is for all possible voltage measurements.

5. CLINICAL APPLICATIONS

There are a wide range of clinical applications that the electrical impedance tomography (EIT) can be used in, at a low cost and without any known hazard [18,115,128]. The fact that biological tissues have a wide range of resistivities (see Table 2) implies that good tissue contrast can be obtained in EIT imaging and therefore, it would be very useful for clinical assessment of patients.

This chapter is devoted to the various applications of EIT in the medical field. Although, some of these have been already demonstrated, some at the present time are speculations. Up to now, very few *in vivo* images have been obtained, which is going to be explained.

5.1 Cerebral Hemodynamics

The incidence of periventricular intraventicular hemorrhage in low-birthweight infants (1500 g), or infants born less than 35 weeks of gestation, is about 40 to 45% [122]. This is a major cause of death in these infants. Therefore, early detection of the intraventicular hemorrhage (IVH) in these infants would be useful.

The most reliable and convenient screening procedure is ultrasound scanning. Ultrasonic scanning is usually done only once every 24 hours on a patient. Therefore, it becomes difficult to determine the exact time the hemorrhage occurred. If it could be

determined, a better insight into the etiology of IVH could be obtained, which is not properly understood. Moreover, the infants in the risk group should be monitored closely, and kept under constant watch.

Cerebrospinal fluid (CSF) is about 2-1/2 times as conductive as blood (see Table 2). IVH occurs when the fragile network of capillaries situated below the cerebral ventricles rupture, which leads to the oozing out of blood and mixing with the CSF in the ventricles, thereby increasing the impedance. This leads to the conclusion that impedance imaging in this case could be helpful.

5.2 Cardiac Parameters

The methods that are used for the measurement of cardiac parameters (Cardiac Output, CO; Stroke Volume, SV; and Left Ventricular Ejection Time, LVET) are mostly invasive, and require cardiac or arterial catheterization.

In contrast, EIT can be used to measure cardiac parameters noninvasively. Eyuboglu *et al* [35] showed that the thoracic impedance changes can be related to the cardiac cycle and hence can be concluded from the EIT images. It has been shown, from the ECG-gated dynamic EIT images of the thorax that the change in the thoracic impedance (related to the cardiac activity) from different organs can be distinguished.

5.3 Limb Plethysmography

The measurement of peripheral blood flow is useful for the diagnosis of cardiovascular diseases, and also for monitoring vascular hemodynamics in the limb segments of patients in the ICU and those undergoing operations. The only accurate method available

is venous occlusion plethysmography, but it is very cumbersome to apply. As the name suggests, the venous blood is prevented from leaving the limb by using a venous occlusion cuff. The limb is pressurized to 50 mm Hg. The initial linear, and then exponential nature of the curve is due to the arterial inflow, which is defined as the increase in volume of blood in the limb per unit time. When the cuff is removed, the volume returns back to normal.

Blood is among the most conductive fluids in the human body. Nyboer *et al* [101] and many others showed that with the flow of blood into any segment of the limb, the volume of blood in that segment fluctuates, and hence, gives rise to an impedance decrease. Impedance also decreases with an increase in velocity of blood [79]. This fact has been corroborated by a number of researchers who made *in vitro* measurements of the impedance of blood under static and dynamic conditions [124].

5.4 Pulmonary Ventilation

The level of ventilation in the lungs is measured using radioisotope lung scans, which is harmful, but, covers the entire lung. EIT can be used repeatedly without causing any harm to the patient but the EIT image can only give a cross-sectional view of the lung in a plane.

Static imaging would be very useful in detecting apnea. But, even dynamic images obtained using EIT could be used to monitor infants who are prone to apneic episodes.

5.5 Pulmonary Perfusion

Change in fluid volume within the lung could be determined using EIT, which

could be related to the changes in the thoracic impedance. Lung tissue basically has two components; air (80%) and fluid (liquid)(5%). During maximal inspiration, the ratio of air to the fluid is maximum, and hence the impedance is maximal; during maximal expiration, the amount of air decreases inside the lungs, which implies a decrease in the impedance. Therefore, any increase in the proportion of the fluid in the lungs would imply a significant drop in impedance. This relationship has been confirmed by Pomerantz *et al* [107] who carried out experiments on humans. The changes in electrical impedance can, therefore, be used as a means for detecting impending pulmonary edema.

5.6 Stomach Emptying

The rate of stomach emptying can be used to detect congenital heart diseases, gastroesophagal reflux and pyloric stenosis. It can also be used for studying the influence of the component parts of various types of food on gastric emptying, such as the fat proportion [89].

The present methods for measuring stomach emptying are invasive, and therefore, are not ideal for routine clinical use. The methods are: the Marker dilution technique and Scintigraphy (Gamma Camera). EIT can be used to image the profile of gastric emptying. It is a noninvasive and inexpensive technique. After a meal is consumed, as the food passes through the various stages of the stomach and upper abdomen, the stomach resistivity changes [124].

5.7 Bladder Volume

The measurement of bladder volume is important in the investigation of patients

suffering from a disturbance of bladder fullness (maturation), which should be avoided urgently. The problem of bladder fullness is very prevalent among the elderly, particularly elderly women. Also the urinary bladder may be paralysed by spinal-cord injury. Ultrasonic imaging of the bladder is the most commonly used diagnostic procedure. The ultrasonic bladder sensor provides the user an external electric signal, which acts as an internal stimulus. The volume of urine is continuously monitored using this device, and when it reaches the threshold level, the user is alerted by an alarm. This method requires the patient to remain supine and immobile [87].

Some experiments by Denniston and Baker [29] have been done using impedance changes for monitoring bladder fullness. They have used a four electrode impedance measurement system, which is a primary EIT device. EIT, a noninvasive technique, could be used to monitor the urine accumulation in the bladder.

5.8 Hyperthermia Monitors

The need to measure the temperature deep within the tissue plays an important role in the detection and treatment of cancer using microwave. The present techniques are invasive, in which the thermocouples, thermistors or optical fibres are implanted in the patient to obtain the temperature profile within the body. There exists a need to develop a noninvasive technique.

EIT responds to temperature changes in the tissues [52]. The temperature coefficient of electrical conductivity of tissue is about +2%/^{o}C, which is very large compared to the X-ray absorption coefficient (in CT), which changes only by 0.04%/^{o}C [51]. A temperature increase, can, therefore, be sensed from a change in conductivity occurring during a

hyperthermia treatment.

5.9 Breast Tissue Analysis

The detection of soft tissue lesions is particularly important in breast tissue analysis, for the detection of malignancies in the breast, which in the presently available methods, they are difficult to detect [30]. EIT seems to be one possibility to tackle such a clinical problem. Fricke and Morse [39] showed that the dielectric constant in the breast would change, if a tumour were present. Also, the highly vascularized tissue surrounding a tumour will have a low resistivity, which contrasts with the avascular tissue of the tumour; this change in resistivity (due to the growth of a tumour) could be sensed by EIT. Skidmore *et al* [119] have developed an EIT system for this purpose.

5.10 Monitoring Fracture Healing

Large changes of electrical characteristics are associated with limb fractures in the plane of the fracture which revert to normal during the healing process. Kulkarni *et al* [77] used impedance imaging techniques to measure and image the spatial distribution of changes in resistivity during the healing process. There is suddenly a highly conductive region in the plane of the fracture subsequent to the occurrence of a diaphyseal fracture. Then, during the process of healing, the region recovers the normal electrical characteristics as the fracture hematoma is organized to form a dense mass of bone.

5.11 Detection of Neural Activity

The membrane surrounding a neuron has a lower resistivity when the neuron is

depolarized than when polarized. It has been suggested [85] that the bulk changes in neural tissue when it is active might be detected using a method of impedance imaging. The idea is very attractive as it would enable the area within the brain which become active following an afferent stimulus to be seen. Perhaps a visual stimulus could be followed from the brain stem to the visual cortex. It might be possible to identify the focus of an epileptic attack and so use this information to guide surgical intervention. However, there is yet no experimental evidence to show that evoked resistivity changes can be seen.

5.12 Measurement of Lean-Fat Ratios

The ratios of resistivities of fat and muscle is approximately 5:1. Ratios of less than 1.3:1 can be resolved relatively easily using EIT so fat and muscle are well resolved. There is considerable clinical interest in the investigation of nutrition and particularly the changes which can occur postoperatively.

6. FORWARD PROBLEM

6.1 Introduction

In EIT the electric current is applied to the periphery of the body and the corresponding voltage is measured in order to find the internal distribution of conductivity and permittivity. This inverse problem has no unique solution. On the other hand, the direct or forward problem, which consists of finding the voltage on the periphery when the internal distributions of conductivity and permittivity, as well as the applied current, are known does have a unique solution. The inverse problem can be solved through an iterative solution of the forward problem. The algorithm starts with a usually uniform initial estimate of the conductivity and permittivity distribution. Then the forward problem is solved for the initial estimate and the resultant voltage is compared with the actual one. In the next step, the difference between the computed and the measured voltages is used to update the conductivity and permittivity distributions. This process continues until the difference between these two reduces to a specified level, assuming the algorithm converges. Therefore, a fast and accurate solution to the forward problem is extremely important.

Except for some trivial conditions, there is no analytical solution for this problem and therefore using numerical methods is inevitable. Although the network approximation method has been briefly mentioned in some early works in the electrical impedance tomography [30,106], the finite element method (FEM) has been mostly used for this problem

[88]. For the FEM method, most of the software packages are not able to handle the permittivity, mesh generation is a complicated task and simulation of wide area electrodes can only be performed approximately. Here a modified method based on the network approximation is proposed that is able to consider the permittivity as well as the conductivity without increasing computational burden, simulates wide area electrodes without approximation, is computationally fast and easy to implement.

6.2 Basic Model

Experience shows that at frequencies below 10 MHz, the contribution of the electric current induced by the time-varying magnetic field is negligible with respect to the conduction current [88]. The electric field intensity can be derived from a scalar potential ϕ which satisfies the equation

$$\nabla \cdot [\gamma(\nabla\phi)] = 0 \tag{6.1}$$

where $\gamma = \sigma + j\omega\varepsilon$, and σ and ε are the local conductivity and permittivity, respectively. This is the equation used in EIT since the operating frequencies are much below the above mentioned level. In some studies presented in the literature [88] even the displacement current, i.e. the permittivity contribution is neglected. Here it is taken into consideration and one of the main advantages of the presented method is that, practically, the consideration of the permittivity does not increase the computational effort, which is not the case in other methods.

Consider a cube of side Δl containing a homogeneous and isotropic medium, which can be modelled as shown in Fig. 6.1, by a resistor of conductance $\sigma\Delta l$ in parallel with a capacitor of capacitance $\varepsilon\Delta l$ corresponding to each spatial direction. In two-

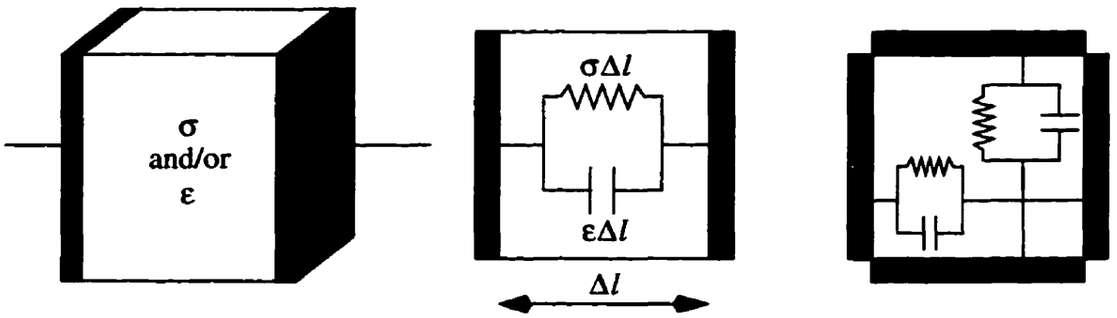

Fig. 6.1 Modelling a material cube of side Δl. (a) Conductive and permittive cube. (b) One-dimensional model. (c) Two-dimensional model with no interaction between the two directions.

dimensional EIT problems, two spatial directions are considered and the corresponding model is that in Fig. 6.1 (c), if there is no interaction between the two directions. The interaction between the circuit elements corresponding to the two directions is taken into account by using the models in Figs. 6.2 and 6.3.

When assembled with adjacent cells the symmetrical model in Fig. 6.3 yields supplementary nodes, as shown in Fig. 6.4, which increases the size of matrices involved in the nodal admittance matrix (NAM) to be inverted for computing electrode voltages. A previously proposed architecture that does not produce extra nodes is represented in Fig. 6.5 [37].

Here an alternative architecture is proposed that decreases further the number of nodes and the number of elements as well. It is shown in Fig. 6.6, where the values of the circuit elements are $\sigma\Delta l/2$ and $\varepsilon\Delta l/2$, respectively. The advantage of this model lies in the fact that an obvious simplification can be performed on its parallel elements. Namely,

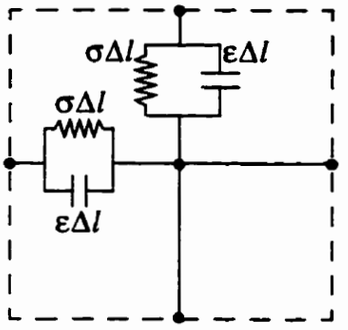

Fig. 6.2 Model with interaction between two directions.

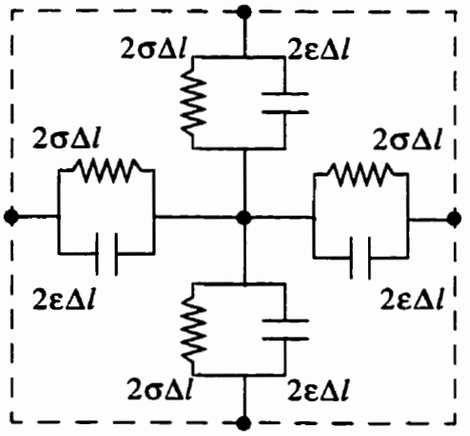

Fig. 6.3 Improved model with symmetrical topology.

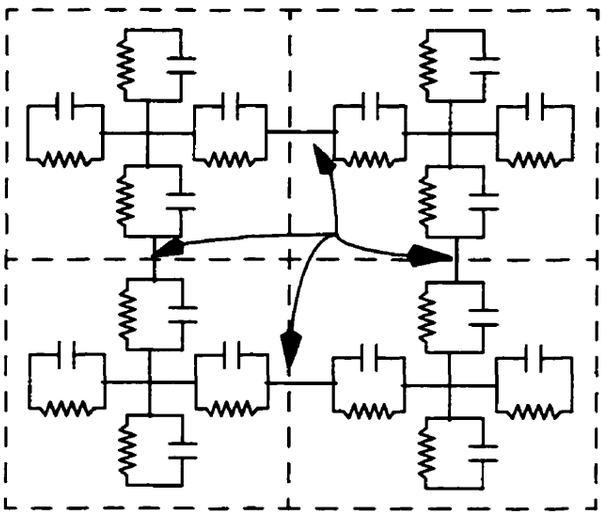

Fig. 6.4 Additional nodes resulting from connecting several cells.

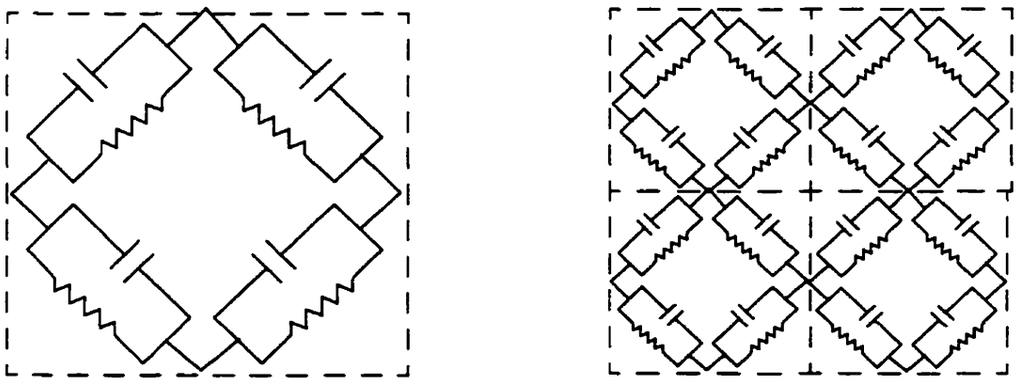

Fig. 6.5 Improved model with no extra nodes. (a) A single cell. (b) Connecting several cells.

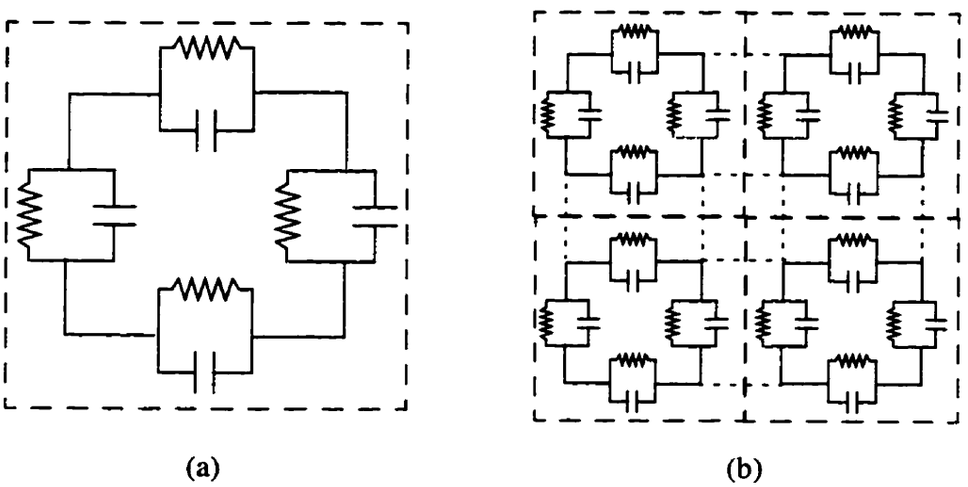

Fig. 6.6 Proposed improved model. (a) A single cell. (b) Connecting several cells.

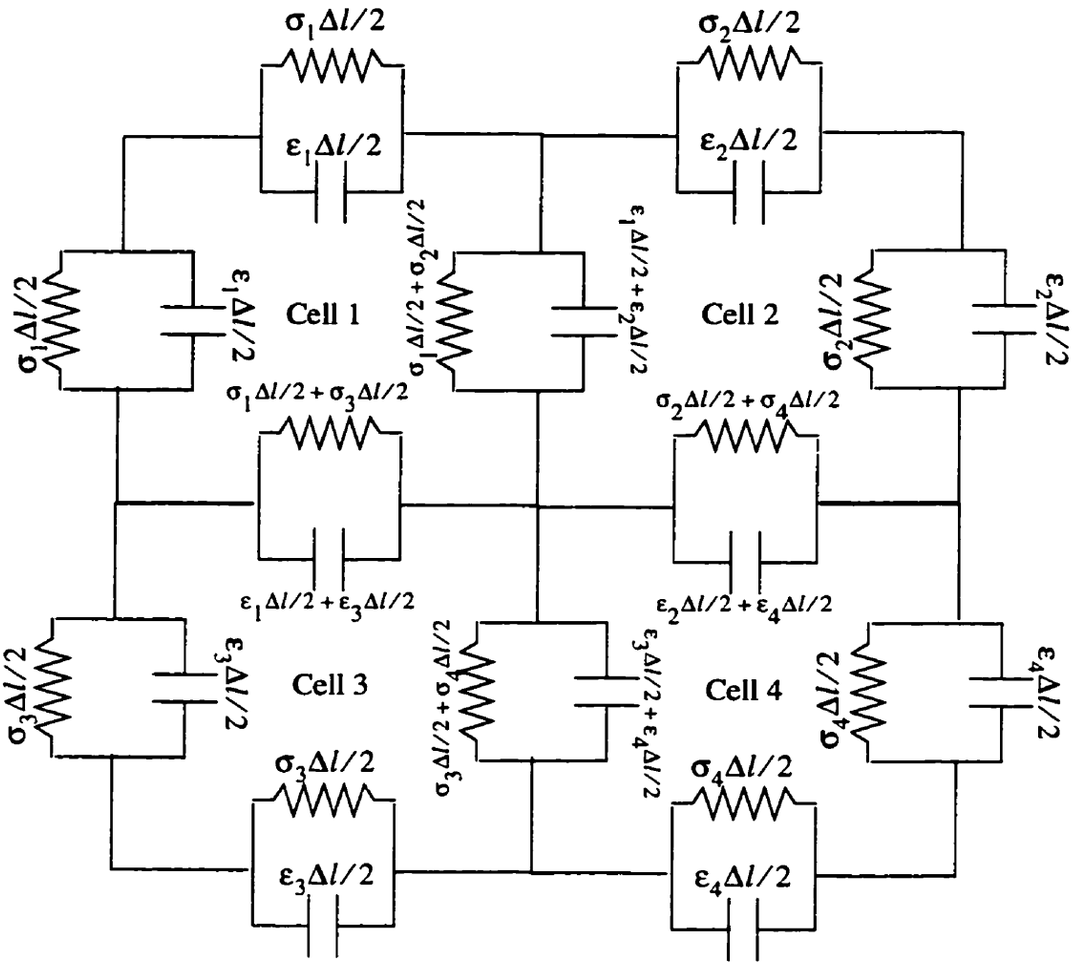

Fig. 6.7 Network approximation for EIT frequencies.

conductances and capacitances of neighboring cells can be simply added together to produce a simpler network. This is shown in Fig. 6.7, where some element values are indicated. In order to make the model consistent, one needs to modify the values associated with the cell sides lying on the boundary of the region to be modelled. To illustrate what happens, consider the modelling of a homogeneous square. The assembled cells will contain resistors and capacitors which are all equal to each other, except for the region boundary, where the corresponding values are equal to half of the others. If this model is excited with current sources on one side of the square by injecting a certain current into it and by having the same current drained from the opposite side, then a uniform voltage distribution along that direction is expected. To achieve this, there should be an equal admittance over all the parallel paths in the direction considered. It is obvious that the two border paths have higher admittance (twice, in this case), thus producing a nonuniform voltage distribution. To correct this nonuniformity assume that there is one more layer of cells connected with those located on the region boundary, which is equivalent to adding their corresponding admittances to the last cell layer. In effect, if in Fig. 6.7 the upper row is the last one, then the corrected values of the conductance and the capacitance for the cell 1, for instance, are $\sigma_1 \Delta l$ instead of $\sigma_1 \Delta l/2$, and $\varepsilon_1 \Delta l$ instead of $\varepsilon_1 \Delta l/2$, respectively.

6.3 Electrode Modelling

It has been shown [68] that large area electrodes increase the distinguishability [68], and so they are preferred. At the same time, large area electrodes have the advantage of allowing for bigger current amplitudes, which is equivalent to a better signal-to-noise

ratio. However, modelling of large area electrodes is difficult in most methods. For instance, in the finite element method it is not allowed to connect such an electrode to several nodes, and one has to use low magnitude resistors in series with each connection. The lower the resistance of these resistors the better the model of the respective electrodes, but correspondingly the condition of the system matrix is more deteriorated. As a consequence, a trade-off has to be adopted.

In the proposed network approximation method, it is possible to connect an electrode to as many nodes as desired by modifying appropriately the nodal admittance matrix in terms of these new connections. If one wishes to connect a current source to several nodes in the network, this can be done by first connecting that source to one of the nodes and then by connecting other nodes to the first one, in other words by short-circuiting those nodes together. In order to illustrate the necessary modifications of the NAM when short-circuiting two nodes, suppose the nodes i and j are connected to form the new node i. The following alterations occur:

1) The admittance connecting nodes i and j becomes a closed loop element, which is no longer relevant, i.e. $y_{ij}^{\text{new}} = 0$.

2) The admittance between nodes i and k and that between j and k, will be in parallel and so are added together, i.e. $y_{ik}^{\text{new}} = y_{ik} + y_{jk}$ and $y_{ki}^{\text{new}} = y_{ki} + y_{kj}$, $k \neq i, j$.

3) y_{ii} and y_{jj} are equal to the sum of all admittances connected to nodes i and j respectively. These include the admittance between nodes i and j as well. After connection, y_{ii} should be equal to the sum of all admittances connected to nodes i and j excluding y_{ij}. This can be done by adding y_{ii} and y_{jj} and then subtracting y_{ij} twice, as the latter

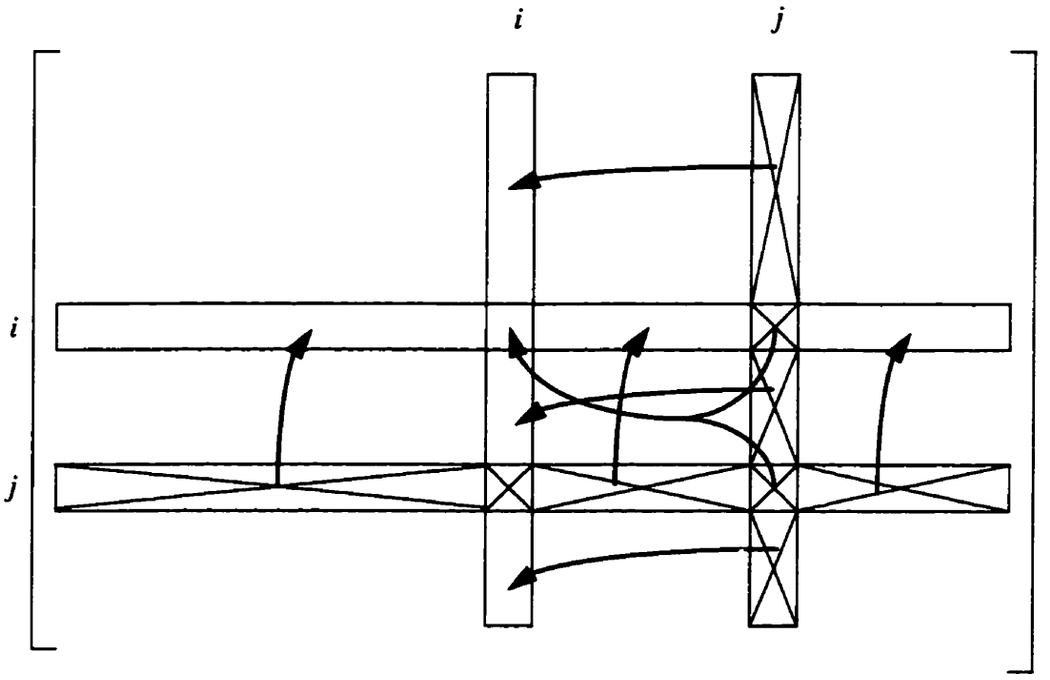

Fig. 6.8 Operations performed to connect node *j* to node *i* for modifying the nodal admittance matrix.

was considered once in y_{ii} and once in y_{jj}, i.e. $y_{ii}^{new} = y_{ii} + y_{jj} + 2y_{ij}$. The plus sign for y_{ij} is used since y_{ij} is actually equal to the negative value of the admittance between *i* and j.

4) The modified network does not have the node *j* any more and so its corresponding row and column should be removed from the NAM.

The above procedure is illustrated in Fig. 6.8. In this Figure, the elements on column *j* except for those on rows *i* and *j* are added to their corresponding elements on column *i*. In the same manner, the elements on row *j* are added to their counterparts on row *i*, except for those on columns *i* and j. The value of y_{jj} is added to y_{ii} plus two times y_{ij}. The

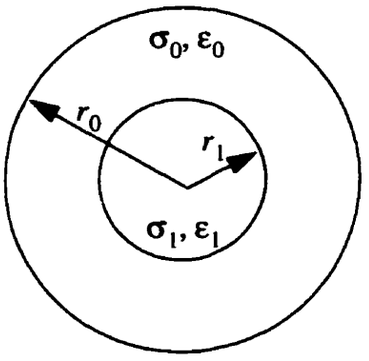

Fig. 6.9 A homogeneous cylinder with a coaxial cylindrical anomaly inside.

row and the column j are to be deleted from the NAM.

6.4 Model Evaluation

Consider a homogeneous circular cylinder with a coaxial inclusion of a circular cylinder of a different material, as shown in Fig. 6.9. This test structure admits an analytical solution. Indeed, the electric potential satisfies Eq. (6.1) [106] with the boundary condition

$$j(\theta) = \gamma_2 \left.\frac{\partial \phi}{\partial n}\right| r = r_2 \tag{6.2}$$

where $j(\theta)$ is the injected current density, $\frac{\partial}{\partial n}$ denotes the normal derivative outwardly oriented, and $\gamma = \sigma + j\varepsilon$. $j(\theta)$ satisfies the condition

$$\int_0^{2\pi} j(\theta)\, d\theta = 0. \tag{6.3}$$

The average potential on the boundary is assumed to be zero,

$$\int_0^{2\pi} \phi(r_2, \theta)\, d\theta = 0. \tag{6.4}$$

This problem can be solved analytically by using the method of separation of variables in polar coordinates. The solution can be find in Appendix A where the final answer after many manipulations is

$$\phi(r_0, \theta) = \frac{r_0}{\gamma_0} \frac{\gamma_1 (R^2 - 1) - \gamma_0 (R^2 + 1)}{\gamma_0 (R^2 - 1) - \gamma_1 (R^2 + 1)} \cos\theta \tag{6.5}$$

where $R = r_1 / r_0$.

The proposed network approximation has been applied to the same structure of Fig. 6.9. Figure 6.10 shows the region discretization and the location of the electrodes.

Figures 6.11 and 6.12 give the voltages determined at the central point of each electrode. In these figures the values of permittivity and conductivity as well as dimensions are $\varepsilon_1 = 5 \times 10^5 \varepsilon_0$, $\varepsilon_2 = 10^5 \varepsilon_0$, $\sigma_1 = 100\,(S/m)$, $\sigma_2 = 10\,(S/m)$, $r_1 = 0.04\ (m)$ and $r_2 = 0.12\ (m)$ respectively.

Even though the approximation used as shown in Fig. 6.10 is rather coarse, the results obtained by the proposed method compare well with the exact ones from the analytical solution.

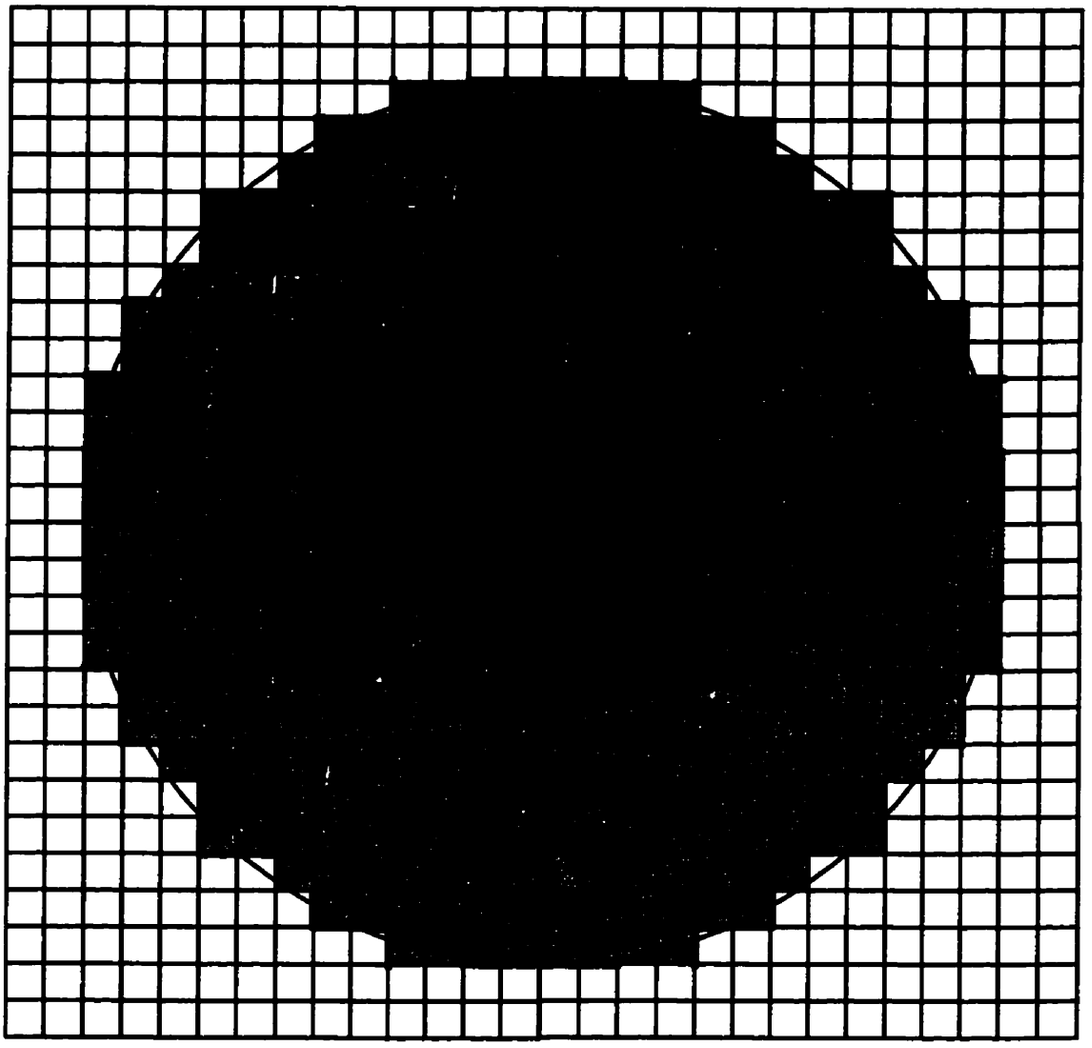

Fig. 6.10 Discretization and electrode positions. Each electrode covers five nodes and there is one node interval between consecutive nodes. Inner cylinder is the anomaly.

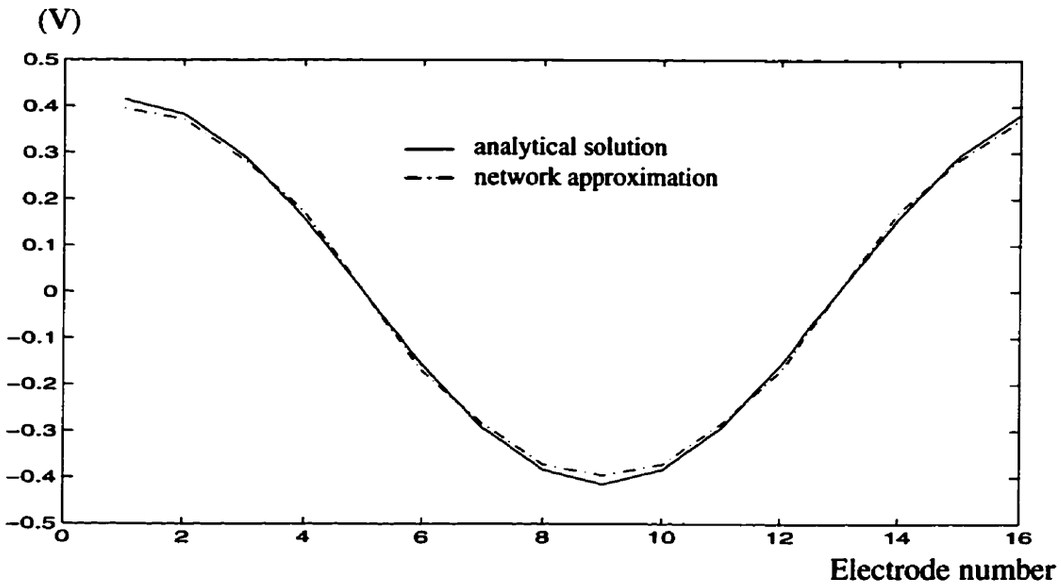

Fig. 6.11 Real part of electrode voltage.

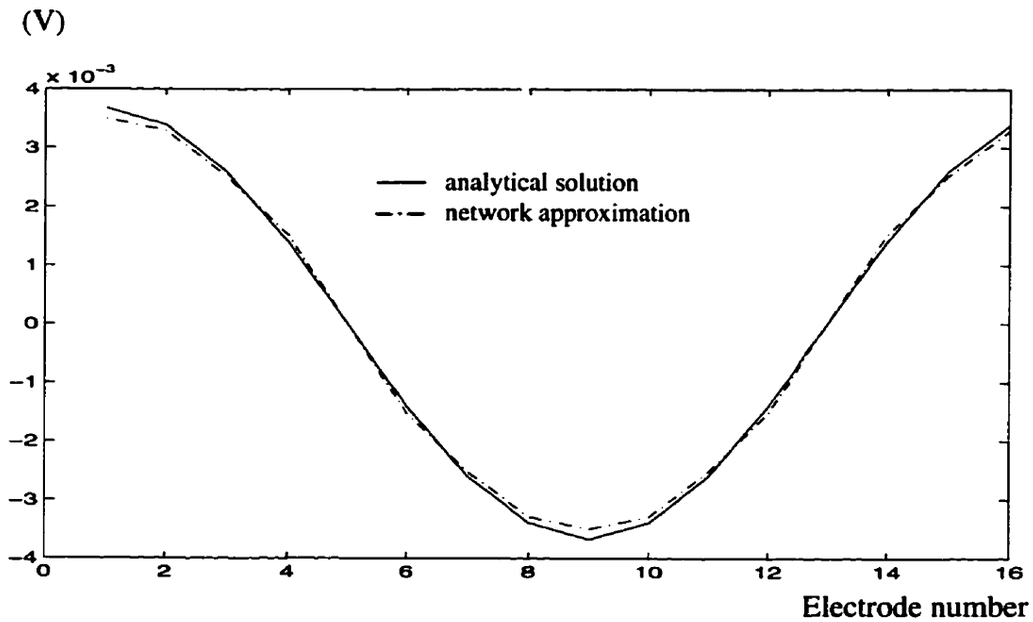

Fig. 6.12 Imaginary part of electrode voltage.

6.5 Discussion

A network approximation method has been proposed for the forward problem involved in the iterative solution of the electrical impedance tomography inverse problem. It can be applied for operating frequencies up to 10 MHz, when the contribution of the electric current induced by the time-varying magnetic field is negligible with respect to the conduction current. This method enjoys an easy implementation and yields accurate results, further it has an excellent ability to simulate wide-area electrodes. Results from a test example illustrate the applicability of the method presented.

7. INVERSE PROBLEM

In the electrical impedance imaging algorithms developed so far, the inverse problems involved are treated by using either iterative methods, which produce more accurate results but require large amounts of computation time, or non-iterative methods that, though faster, produce less accurate results. In this thesis, a new iterative procedure for electrical impedance imaging is presented. At each iteration step, the updated conductivity distribution is used to solve a forward problem and, then, two-layer backpropagation neural networks (BPNNs) with non-linear activation functions for the hidden layer are employed for solving an inverse problem. This allows for a smaller computation time with respect to other iterative methods and, at the same time, yields accurate results. Comparison with results obtained by applying a leading impedance tomography algorithm illustrates the efficiency of the proposed iterative method.

7.1 Introduction

Undoubtedly, the solution of the inverse problem, i.e. the computation of the conductivity distribution when the electrode voltages and the injected currents are known, is the most challenging part in an electrical impedance imaging system. This problem can be solved by non-iterative methods, such as those implementing various backprojection techniques [9,16,114] or employing sensitivity coefficient methods [76], and also iterative

methods such as the equipotential lines method [66], the perturbation method [73], the double constraint method [125], the Newton-Raphson method [130] and the compensation theorem method [90]. The non-iterative methods are fast methods, less sensitive to noise and to electrode displacement, but they produce less accurate and dynamic results. The iterative methods produce more accurate and static results, in general, but are computationally extensive, very sensitive to noise and measurement errors, as well as to electrode displacement. Since 1991, several research groups have reported impedance imaging results obtained by non-iterative methods employing neural networks. These networks perform well in a noisy environment when appropriately trained with noisy patterns. One-layer BPNNs with linear activation functions have been proposed in [54,3,99], and also one-layer BPNNs with non-linear activation functions [100] and RAM-based neural networks [32,33] have been used for pattern association. From the results obtained by applying such non-iterative methods, it has been realized that the neural networks required to solve the inverse problem in its general form and with accurate results would be too big to be realistic, from the point of view of the number of units in the input and in the hidden layer, as well as from the number of necessary training patterns. On the other hand, iterative neural networks such as recurrent neural networks, have successfully been used for pattern recognition [21]. Here, an impedance imaging procedure is proposed that is based on employing BPNNs in an iterative scheme that enables the use of relatively small BPNNs to solve accurately this highly non-linear inverse problem, with several times smaller CPU time compared with existent iterative methods. The proposed method also enjoys the advantageous features of the neural networks including their performance in the presence of noise and the capability of parallel processing, although these issues are

not addressed here.

A review of backpropagation neural networks has been given in Appendix B. Readers who are familiar to the neural networks may proceed to the next section where the Author proposes its implementation in the inverse problem.

7.2 Proposed Method

The data collection method has a direct impact on the solution of the inverse problem. Accordingly, a suitable data collection method needs to be selected for the proposed reconstruction algorithm which is based on the implementation of the neural networks. Chapter 3 was devoted to data collection methods and it was explained that selecting an appropriate data collection method improves the reconstruction algorithm considerably. From that discussion, it is known that the adaptive method has clear superiority over the other methods. However, this data collection method can not be used in the approach here because, the current injection pattern is dependent on the conductivity distribution. As a result there are different current injections for different conductivity distributions and one would not be able to make a valid comparison between electrode voltages used for training and those encountered during employing of the neural network namely recall episode. In other words, the network should be presented with input vectors that have been obtained under the same circumstances as training patterns, i.e. the same current injection patterns. By eliminating this method from the list, the best other options would be the trigonometric and Walsh functions. Either of these methods, enables one to compare the electrode voltages of the training set to those which are measured during employment of the network. Between these two methods, Walsh functions are better,

because in this case only fixed amplitude current generators with adjustable phase (that switches only between 0 and 180 degrees) are needed.

Therefore, Walsh function patterns are employed for the proposed method. These patterns exploit the advantage of operating with a constant current amplitude, allowing at the same time an easy programming of the current sequences. For a 16-electrode system, 15 patterns can be implemented (see Chapter 3 and Fig. 3.3).

A forward problem solving module is used in the proposed procedure. Its operation is based on a network approximation numerical method [91] (also see Chapter 6) which is easy to implement and produces fast and sufficiently accurate results. Moreover, it allows to simulate accurately wide area electrodes which could be more difficult to achieve when using finite element methods [88]. The forward problem solving module is used twice, first for producing the patterns for training the neural networks and then during the iterative procedure itself.

The inverse problem is solved iteratively by using a set of two-layer BPNNs appropriately trained as described below. Although the proposed method may be used while considering both conductivity and permittivity, here, only the real part of the measured voltages and hence the conductivity of the object are considered, to keep the computational burden lower and emphasize the method itself.

7.2.1 Neural Network Architecture

Consider for illustration a 16-electrode system, where 15 independent voltages can be identified for each current pattern. Since 15 patterns of the Walsh functions can be exploited, there are 225 measured voltages, which constitute the input vector for the neu-

ral networks. The output vectors of the neural networks has a number of entries equal to the number of cells in which the object is discretized. In the illustration considered, the object is discretized in 16 cells (as shown in Fig. 7.3). Linear activation functions are used for the units in the output layer and the hyperbolic tangent activation functions for the units in the hidden layer. By using a linear activation function in the output layer, the scaling of the outputs of the neural networks can be avoided and also the training episode is shortened approximately twenty times at the expense of more units in the hidden layer.

Instead of using a big, single neural network with 225 units in the input layer, 15 neural networks have been employed, each one for a Walsh function current pattern and with only 15 units in the input layer. This architecture decreases the overall size of the neural networks by a factor of about 15. Two different reconstruction problems have been solved using the proposed architecture namely; 1) the reconstruction of objects with conductivities of a few cells freely different from known conductivities of the background cells, and 2) the reconstruction of objects with conductivities of all cells different from each other, but, within a predefined interval. Reconstruction of conductivities for these two problems, differs from each other in two ways; 1) the number of units in the hidden layer and 2) the training patterns. When necessary, these two cases are described separately and from now on, they are called Types A and B, respectively.

7.2.1.1 Neural Network Architecture: Type A

Two-layer BPNN with tangent hyperbolic activation function in the hidden layer and units with linear activation function in the output layer is used to solve the inverse problem. As mentioned before, using units with a linear activation function in the output

layer increases the needed units in the hidden layer but decreases the training time considerably. In effect this selection decreases the CPU time at the cost of more memory which is preferred. However the BPNN shows the best performance, when the number of units in the hidden layer are taken to be as low as possible but still capable of learning the training patterns. Using more units in the hidden layer, decreases the ability of the network to generalize the features of the training patterns and instead simply memorizes the training patterns. For an object discretized to 16 cells, 300 units in hidden layer has been found to be optimum. Therefore, 15 neural networks are utilized each one of them for each pattern of the Walsh functions with 15 units in the input layer, 300 units in the hidden layer with a tangent hyperbolic activation function and 16 units with linear activation function in the output layer.

7.2.1.2 Neural Network Architecture: Type B

The reconstruction in this case is considerably more demanding compared to the type A. Again 15 neural networks are employed one for each current pattern and the same number of units in the input layer and output layer and the same kind of activation functions as in the Type A architecture. The difference, however, is in the number of units in the hidden layer. More units in the hidden layer are needed for Type B than in Type A since reconstruction is more difficult. Moreover, experience shows that different Walsh

Table 5: Number of units in the hidden layer for various BPNNs associated with corresponding Walsh function current patterns for the reconstruction problem of the Type B.

Walsh function current pattern Number	1	2	3	4	5	6	7	8

Table 5: Number of units in the hidden layer for various BPNNs associated with corresponding Walsh function current patterns for the reconstruction problem of the Type B.

Number of units in hidden layer	1500	1500	1500	2000	2000	2500	1500	2200
Walsh function current pattern Number	9	10	11	12	13	14	15	
Number of units in hidden layer	1800	2200	1800	2400	1800	2400	1700	

function current patterns require different number of units in the hidden layer of their corresponding BPNNs due to the different relationships between the electrode voltages and the cell conductivities. Consequently, different number of units in the hidden layer has been chosen for the various neural networks corresponding to the Walsh functions, namely, between 1500 to 2500 (see Table 5).

7.2.2 Neural Network Training

Selecting the appropriate patterns for training of these neural networks is a key issue in the proposed method. Usually, BPNN is trained with patterns whose input vectors are linearly independent. This arrangement is not applicable in here, because, the chosen conductivity distributions comprises the output vectors and, the input vectors are the corresponding computed electrode voltages.

7.2.2.1 Training: Type A

In the proposed method, the neural networks have been trained using a set of patterns for the conductivity distribution. Each distribution has only one cell with a conduc-

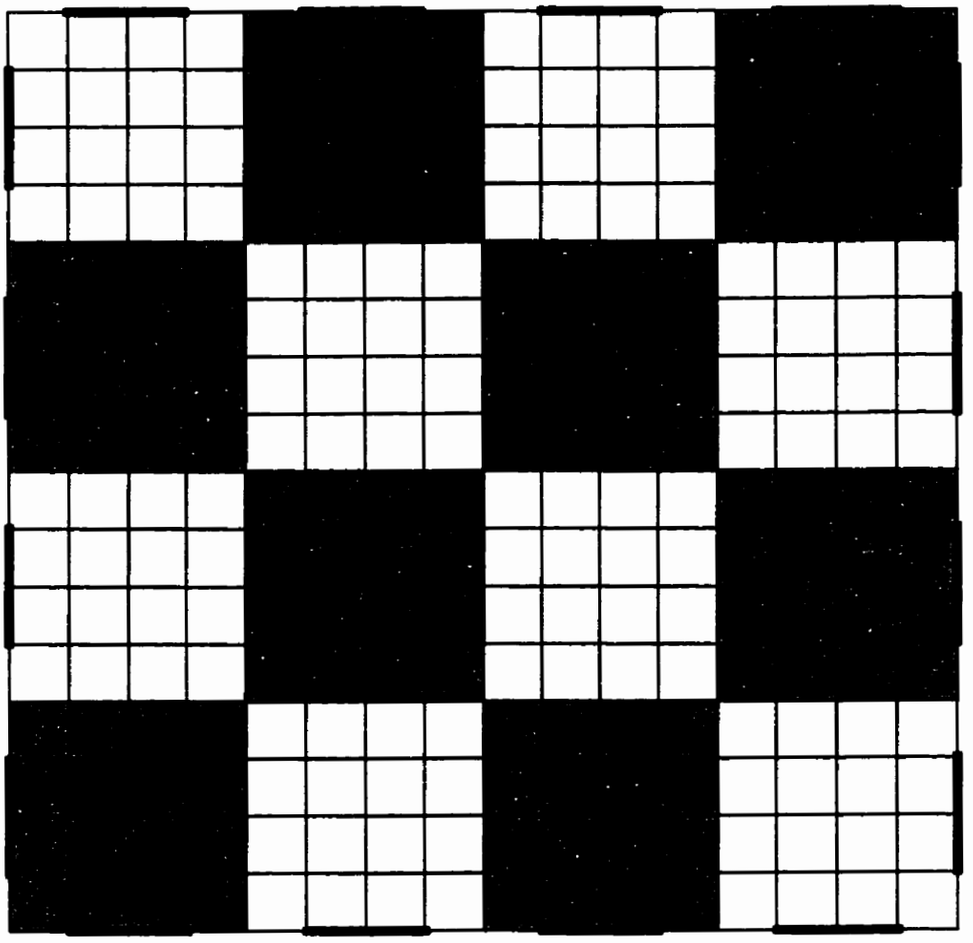

Fig. 7.1 Discretization of the object in a 16 by 16 cells for the solution of the forward problem in a 16-electrode system; each electrode covers three nodes.

tivity different from that of the other cells. This conductivity was selected to be 1/6, 3/6, 5/6, 7/6, 9/6 and 11/6 of the conductivity of the background, which was set at 6 S/m. It should be noted that these patterns are not linearly independent. With 16 cells this yields 97 different patterns for training, with one pattern having all the conductivities equal to that of the background. These patterns are employed in the forward problem solving mod-

ule [91] to determine the corresponding electrode voltages when the injected currents are known. For the forward problem solving module the object is discretized in a finer mesh of 16 by 16 cells. Each of the 16 electrodes cover 3 nodes in this model as shown in Fig. 7.1. The pattern with the conductivity of all the cells equal to the background conductivity is chosen as the reference pattern and its cell conductivities and electrode voltages are subtracted from the corresponding values in any other pattern. This arrangement is necessary for the iterative procedure that is described in the next section.

7.2.2.2 Training: Type B

For this case, the neural networks have been trained using a set of patterns for the conductivity distribution within the object that is chosen in such a way that three conductivity values, 1, 1.2 and 1.4 S/m, have been selected as background conductivities. Three patterns correspond to homogeneous distributions of conductivity within the object, with these three conductivity values. In the other patterns, one cell has a conductivity which is different from that of the background, with values equal to 1/6, 5/6, 7/6 and 11/6 of that of the background. For a number of cells equal to 16, this produces a total of 3x4x16 patterns. The input vectors are given by the voltages associated with these patterns and have been generated by using the forward problem solving module. The electrode voltages and the cell conductivities of the second homogeneous pattern have been subtracted, respectively, from those corresponding to the other patterns. The resulting sets of electrode voltages and of conductivities constitute, respectively, the input and the output training vectors for the input and the output layers of the neural networks. Thus, the neural networks are trained with relative values of electrode voltages and of conductivities.

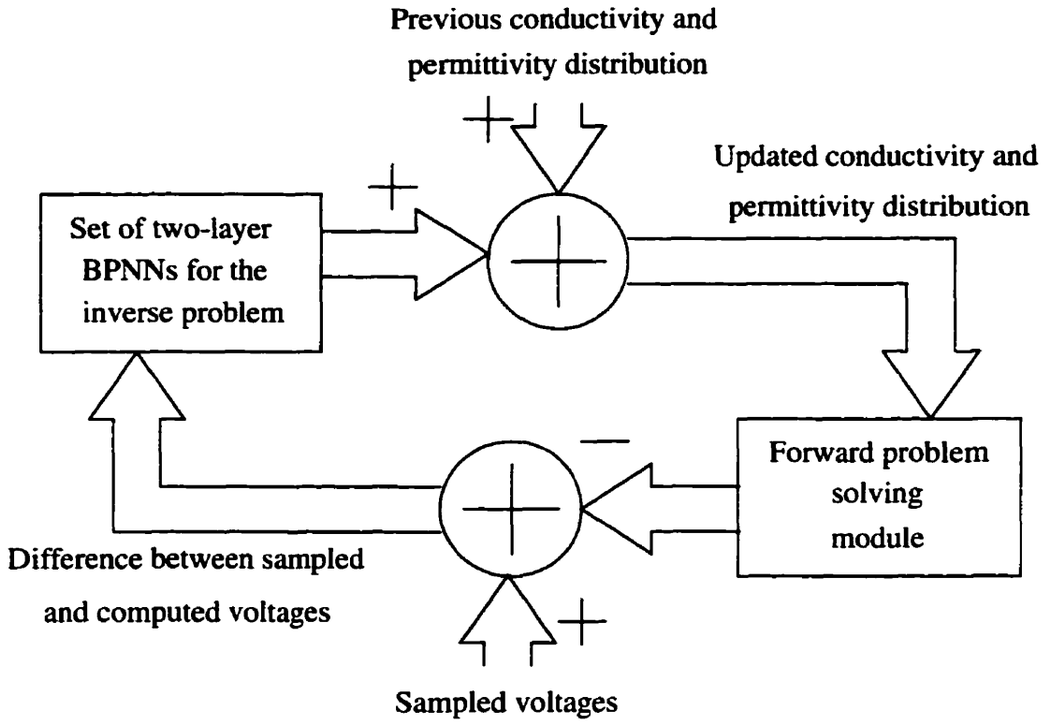

Fig. 7.2 Principle of the iterative reconstruction procedure using neural networks

7.2.3 Iterative Image Reconstruction

The trained neural networks are employed iteratively as indicated in Fig. 7.2. The procedure consists of the following main steps.

1) A homogeneous conductivity distribution equal to background conductivity (6 S/m for Type A and 1.2 S/m for Type B) is used as initial estimate.

2) The electrode voltages corresponding to the respective current patterns are computed in the forward problem solving module.

3) These computed electrode voltages are subtracted from the measured ones and the

result is forwarded to the neural networks.

4) Corresponding outputs of all the neural networks are added and then multiplied by an updating factor in the range from 10^{-4} to 0.4 in terms of the rate of convergence.

5) The resulting conductivity distribution is superposed on the previous one and the updated conductivity distribution is again used in the forward problem solving module to compute the new electrode voltages.

6) The error, i.e. the difference between the measured electrode voltages and the computed ones is examined; if this error is smaller than the specified threshold, then the procedure is terminated; if the error has decreased, the updating factor is increased and the process is repeated from step 4; if the error has increased, then the electrode voltages and the conductivity distribution corresponding to the previous updating factor is selected and the iteration process continues from step 3.

Although each network is trained with patterns having only one cell with a conductivity different from that of the background, this iterative procedure allows for the Type A neural network, the reconstruction of conductivity distribution for objects with up to three cells having conductivities freely different from that of the background, and for the Type B network, the reconstruction of conductivity distribution for objects with conductivities of all cells freely different from that of the background and with values between 1 and 1.4 S/m.

7.2.4 Reconstruction Tests

A two-dimensional domain has been discretized in 4x4 cells as shown in Fig. 7.3, and 16 current injecting electrodes have been placed equidistantly on the perimeter.

Several tests are presented to illustrate the proposed procedure for both reconstruction Types A and B.

7.2.4.1 Method Evaluation: Type A

Three cells in Figs. 7.3 (a) and 7.4 (a), and two cells in Figs. 7.5 (a) and 7.6 (a), have conductivities quite different from each other and from that of the background. These conductivity values have been used in the forward problem solving module, with Walsh function current patterns, to obtain the electrode voltages which are assumed to be the measured voltages. Sun Ultra 1 workstation and MATLAB-based [84] software were employed. The training episode for the networks used took about 15 hours of CPU time employing the same software and hardware. The reconstructed conductivity distributions, along with the required number of iterations and the total CPU time, are shown in Figs. 7.3 (b) to 7.6 (b), respectively. The error indicated have been evaluated as:

$$error = \frac{\sqrt{\sum_{cell} (cell\ \ conductivity - reconstructed\ \ cell\ \ conductivity)^2}}{\sqrt{\sum_{cell} (cell\ \ conductivity)^2}} \qquad (1)$$

To demonstrate the efficiency of the proposed method, a Newton-Raphson technique [133] was also applied on the same machine using the same MATLAB environment. At least four iterations are needed for the Newton-Raphson method and each iteration requires 71.35 seconds of CPU time. The CPU time needed in the method presented is about 8 times smaller.

7.2.4.2 Method Evaluation: Type B

Three examples have been chosen to illustrate the operation of the proposed method. In Figs. 7.7 (a) and 7.8 (b) two random conductivity distributions, and in Fig. 7.9 (a) a continuous distribution, with values between 1 and 1.4 S/m, are presented. These conductivity values have been used in the forward problem solving module, with Walsh function current patterns, to obtain the electrode voltages which then are taken to be the measured voltages. These values are used in the computer program based on the proposed method. The reconstructed conductivity distributions are shown in Figs. 7.7 (b), 7.8 (b) and 7.9 (b), respectively.

Fig. 7.3 (a) original conductivity distribution; (b) reconstructed distribution. Darker cells have, respectively, 5, 7 and 10 times the conductivity of the background which is set to 6 S/m. The error is 16% and a total of 31.93 s of CPU time is used for 13 iterations.

(a) (b)

Fig. 7.4 (a) original conductivity distribution; (b) reconstructed distribution. Darker cells have, respectively, 5, 7 and 10 times the conductivity of the background which is set to 6 S/m. The error is 14.7% and a total of 17.37 s of CPU time is used for 7 iterations.

(a) (b)

Fig. 7.5 (a) original conductivity distribution; (b) reconstructed distribution. The bright and dark cells have, respectively, 0.1 and 2 times the conductivity of the background which is set to 6 S/m. The error is 2.6% and a total of 111.4 s of CPU time is used for 45 iterations.

(a) (b)

Fig. 7.6 (a) original conductivity distribution; (b) reconstructed distribution. Brighter cells have, respectively, 0.1 and 0.3 times the conductivity of the background which is set to 6 S/m. The error is 2.2% and a total of 27.9 s of CPU time is used for 11 iterations.

(a) (b)

Fig. 7.7 (a) original conductivity distribution; (b) reconstructed distribution. The error is 2.21% and a total of 82.76 s of CPU time is used for 10 iterations.

(a) (b)

Fig. 7.8 (a) original conductivity distribution; (b) reconstructed distribution. The error is 1.64% and a total of 55.02 s of CPU time is used for 6 iterations.

(a) (b)

Fig. 7.9 (a) original conductivity distribution; (b) reconstructed distribution. The error is 5.22% and a total of 113.22 s of CPU time is used for 9 iterations.

7.3 Discussion

A new iterative method, utilising neural networks, has been proposed for the electrical impedance imaging. It is based on employing at each iteration step appropriately

trained neural networks for solving the inverse problem involved, along with a forward problem solving module. Once the training episode is completed, the method requires a reduced computation time with respect to other iterative methods, such as the Newton-Raphson method [132], and yields more accurate results than fast non-iterative methods, such as those based on back-projection [9,18,114,76] or on non-iterative neural networks [3,54,100]. The presented method can also be applied to solve other inverse problems, such as those involved in the inverse scattering of electromagnetic or acoustic waves.

8. IMAGE FUSION USING FUZZY SET THEORY

8.1 Introduction

Improving the performance of the EIT system is mainly connected with increasing its resolution and accuracy. The multi-frequency scheme as an alternative to increasing the number of electrodes has been suggested for this purpose [17,58,108] and enjoys several advantages over the latter scheme. Increasing the number of electrodes not only has technical problems but also, increases the computation time which in most cases is proportional to the fourth power of number of electrodes [43]. Even in the neural network approach, it increases the network input layer dimension as well as the hidden layer dimension and therefore the overall network dimension. On the other hand in the multi-frequency scheme, additional images are obtained with the same computation time and therefore the increase in CPU time would be proportional to the number of applied frequencies. An other point is that the sampling time does not necessarily increase in a multi-frequency scheme because all frequencies could be applied simultaneously and then separated during demodulation.

In this chapter, a method is introduced to fuse images obtained at different frequencies in order to lower the errors and distinguish different tissue. This method was mainly proposed to be used in multi-frequency EIT, nevertheless, it can be implemented in other image fusion applications. The method is based on fuzzy set theory and not only distin-

guishes different tissues but also, preserves and actually enhances the internal contrast. As the inverse problem was solved for a small size problem in Chapter 7, the proposed method here is illustrated using simulated input images.

A review of fuzzy set theory can be found in Appendix C. Interested readers are encouraged to read this appendix before proceeding to its implementation in image fusion in the next section.

8.2 Image Fusion as a Particular Case of Data Fusion

Optimal processing of the data acquired from multiple sources has recently received considerable attention [55,74,80]. Data fusion techniques combine overlapping and complementary data obtained by employing different sensors in order to improve the overall system characterization or to obtain details that can not be recognized using only one source of data. Applications of data fusion are found in a large variety of fields, for instance in automated target recognition [56], guidance for mobile robots and vehicles [70], remote sensing [25], monitoring of manufacturing processes, condition-based maintenance of complex machinery and robotics [1], and medical diagnosis [12]. A concerted effort is under way to define standard terminology, categories, processes and functions for this interdisciplinary area [14,26,57,121], where concepts are used from digital signal or image processing, statistical estimation, control theory, artificial intelligence, classic numerical methods and fuzzy set theory [27,112,113].

Data can be fused at different levels, from the raw data level up to the decision making level [57]. Data fusion methodologies are characterized by the level of input and output [26] or by the topology used for the fusion center [121]. It should be noted that

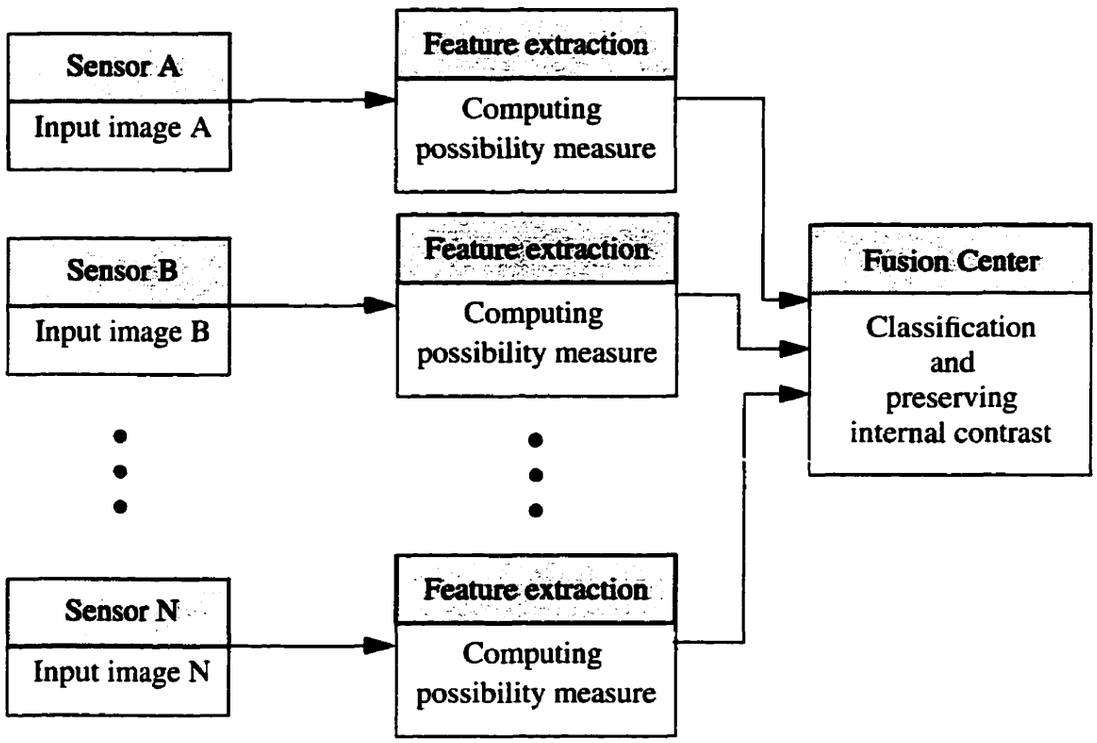

Fig. 8.1 Block diagram for the architecture of multisensor image fusion.

interferences obtained using multisensor fused data may be less accurate than interferences based on acceptable data from an individual sensor. This could be the situation when an attempt is made to fuse accurate with inaccurate data, especially if the degree of uncertainty of the data is unknown. The performance of various data fusion systems is evaluated, in most cases, by numerous simulations and statistical measurements [57]. When dealing with images, the internal contrast is not retained in the fused image. Image fusion methods that maintain or even emphasize the internal contrast are highly desirable, since this might carry important information. For instance, in medical imaging, by using

the internal contrast, one can keep track of minor changes in the tissue which could result from a malignant tumour in its early stages. If the imaging system is an EIT, for example, the darker pixel values in a certain zone of a tissue could be associated with higher values of conductivity, which in turn may be due to a higher vascular integration surrounding the tumour. If another imaging system, for example an X-ray system, is also employed and brighter pixel values are associated to the same zone as before, due to less absorption of X-ray radiation, then it would be extremely valuable to not only identify that specific tissue, but also to retain its internal contrast in the fused image, which could reveal the potential malignant tumour.

Image fusion is a special case of data fusion. Recent attempts to apply fuzzy set theory to the image fusion have produced promising results [13,92,93]. This is due to the fact that the relationships between different object classes and the corresponding pixel values, as well as the uncertainties within each imaging system, can be characterized quantitatively using membership functions. Moreover, the operators and the decision making rules in fuzzy set theory provide the necessary means to handle efficiently the image fusion process. In this chapter, a new image fusion method based on fuzzy set theory is presented. The strength of this method consists in a clear classification of different image components (e.g., different tissues in medical images) and, at the same time, in preserving the internal contrast for each class. A parallel distributed (decentralized) fusion architecture is used in this method. Each imaging system performs its own processing and provides a certain image instead of raw data to the fusion center as shown in Fig. 8.1. In the proposed method it is not necessary that the various sets of data be independent from each other, no fuzzification constraints are needed [112], the input or the output of the fusion

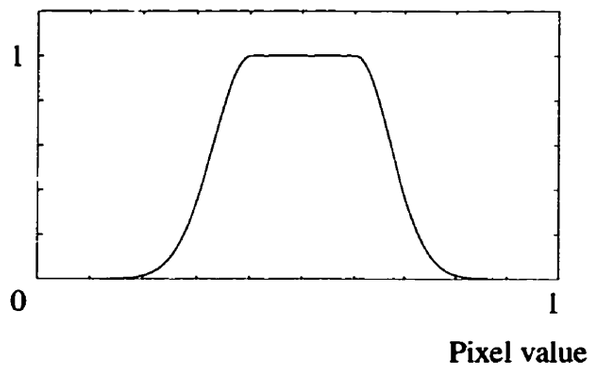

Fig. 8.2 A sample of a membership function for an image component.

center can be in the fuzzy format and not necessarily in crisp labels [113]. If the input data are insufficient to produce highly confident, unambiguous results, this is conveyed to the output so that the interpreter will not be given false information. The implementation of the method is relatively easy and straightforward and the entire procedure can be applied practically in the same way for data with noise. In the following it is assumed that the co-registration of image data (if necessary to be done) has already been performed for the input images.

8.3 Processing approach

The contrast between different image classes is due to different relationships between these classes and the corresponding pixel values, and represents the differences in the measured physical quantities used in the imaging system. Similarly, the internal contrast is due to minor changes in the physical quantity within an individual class. The relationship between the measured physical quantity and the respective pixel values can be

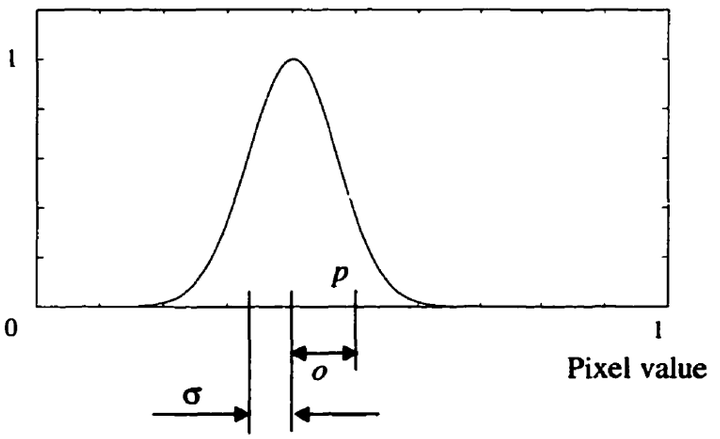

Fig. 8.3 Membership function for noise with a Gaussian probability density function: p is the pixel value, o is the offset, and σ the standard deviation.

represented by membership functions [103], for instance as shown in Fig. 8.2. This figure shows a sample membership function in which the observed greyscale value for a pixel (the ordinate) is mapped to the value of membership in a class (the abscissa). By employing such a membership function, an interval of pixel values is attributed to a specific image class and, moreover, the degree to which a pixel value in that interval is associated with that class is specified. Measurement errors can also be represented using membership functions. Whenever the deterministic errors, such as an offset, and the stochastic errors corresponding to a probability density function of noise are known appropriate membership functions can be defined to represent the noise in an imaging system as shown in Fig. 8.3. By using these membership functions and the corresponding possibility measures, which represent the degree of overlap between two membership functions, we not only determine the boundaries of various image classes in the fused image, but also preserve

the internal contrast within each class. The processing approach consists of two distinct parts: in the first part the input images are fused such that the boundaries of each image class are clearly determined; in the second part the internal contrast within each image class is restored and emphasized.

8.3.1 Determining the Boundaries of the Image Classes

First, a completely separate image for each class is produced. The procedure for identifying the class i in several input images consists of the following steps:

1) Definition of membership functions μ_i^j that represent the class i in each imaging system j employed;

2) Construction of membership functions ν^j for uncertainties in each imaging system j, according to the identified measurement errors;

3) Computation of the possibility measures of μ_i^j's with respect to the corresponding ν^j's for all the pixels in all the input images;

4) Processing the results in Step 3 for the corresponding coordinates in all the images and producing the final image for the class i.

Experience has shown that the t-norm defined as the product of the two membership functions produces better results compared to the usually used t-norm defined as the minimum of the two membership functions. This is due to the fact that the multiplicative t-norm produces smaller possibility measures wherever the two membership functions are overlapping outside their respective full membership intervals, thus decreasing the effect of those pixels that could have been wrongly identified as belonging to a given class, for

instance as a result of the presence of noise.

For the step 4 of the above procedure, one has to take into account that in a given input image a certain class i might be associated with pixel values which are darker than those corresponding to other classes. At the same time, in another input image the class i could be associated with brighter pixel values as compared to other classes. Therefore, the pixel values cannot be simply averaged to decrease the effect of noise. On the other hand, the possibility measures for pixels associated with the class i in all the input images are much greater than those for the pixels corresponding to other classes. These possibility measures can be processed in a number of ways. For instance, we can employ a simple averaging which is an effective method of decreasing the effect of the random noise [46]. A nonlinear mapping (thresholding) in combination with the averaging produces even better results [92].

The uncertainty membership function v^j in Step 2 of the proposed procedure is useful for pixels associated to a class i that have values in the neighborhood of the boundaries of the interval of μ_i^j. Indeed, when due to noise the pixel value is shifted outside this interval, the possibility measure calculated by employing the uncertainty membership function is different from zero, which allows us to count the respective pixel as a member of the class i.

8.3.2 Preserving Internal Contrast

Once the boundaries of each image class are determined, one restores and even emphasizes the internal contrast within each class. This is done by defining a new mem-

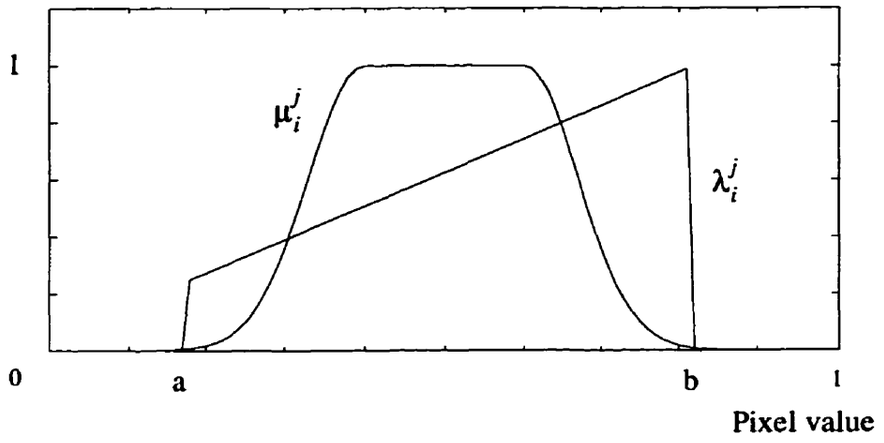

Fig. 8.4 Definition of λ_i^j with respect to μ_i^j for retaining internal contrast.

bership function λ_i^j to represent the class i in the imaging system j. Figure 8.4 presents a suitable example of λ_i^j for the class i when its pixel value interval in the image j is [a,b]. By this membership function we attribute full membership to one end of the interval and one quarter membership, for instance, to the other end. To produce coherent results one should use carefully this definition, as explained in the following example. Assume that a vascular integration region generates lighter pixel values in a certain imaging system and that in another imaging system this region produces darker pixel values. Therefore, if the full membership value of λ_i^j is attributed to the brighter pixels in the former modality, one should attribute full membership value of λ_i^j to the darker pixels in the latter modality.

One may even define different types of λ_i^j membership functions with the full membership value somewhere in the middle of the interval, for instance, or even as discontinuous functions.

The procedure for retaining the internal contrast for the class i consists of the following steps:

1) Definition of appropriate membership functions λ_i^j's for all the classes i and all the imaging systems j;

2) Definition of membership functions ν^j's for every imaging system j, according to the existent measurement errors;

3) Computation of the possibility measures of λ_i^j's with respect to the corresponding ν^j's for all the pixels of the class i;

4) Processing the results in Step 3 for the coordinates corresponding to the class i and producing its final image.

Application of the proposed method yields a much improved reconstructed image with respect to the input images, with the boundaries of the classes clearly determined and with the internal contrast within the classes well preserved.

8.4 Illustrative Example 1

Assume a 20 by 20 two-dimensional grid which is made up of three tissues, say bones, blood vessels and muscles. The geometric positions of these tissues are shown in Fig. 8.5. In the proposed method there is no restriction on the relations between tissues and pixel values associated with different imaging systems, while it is not the case in [12],

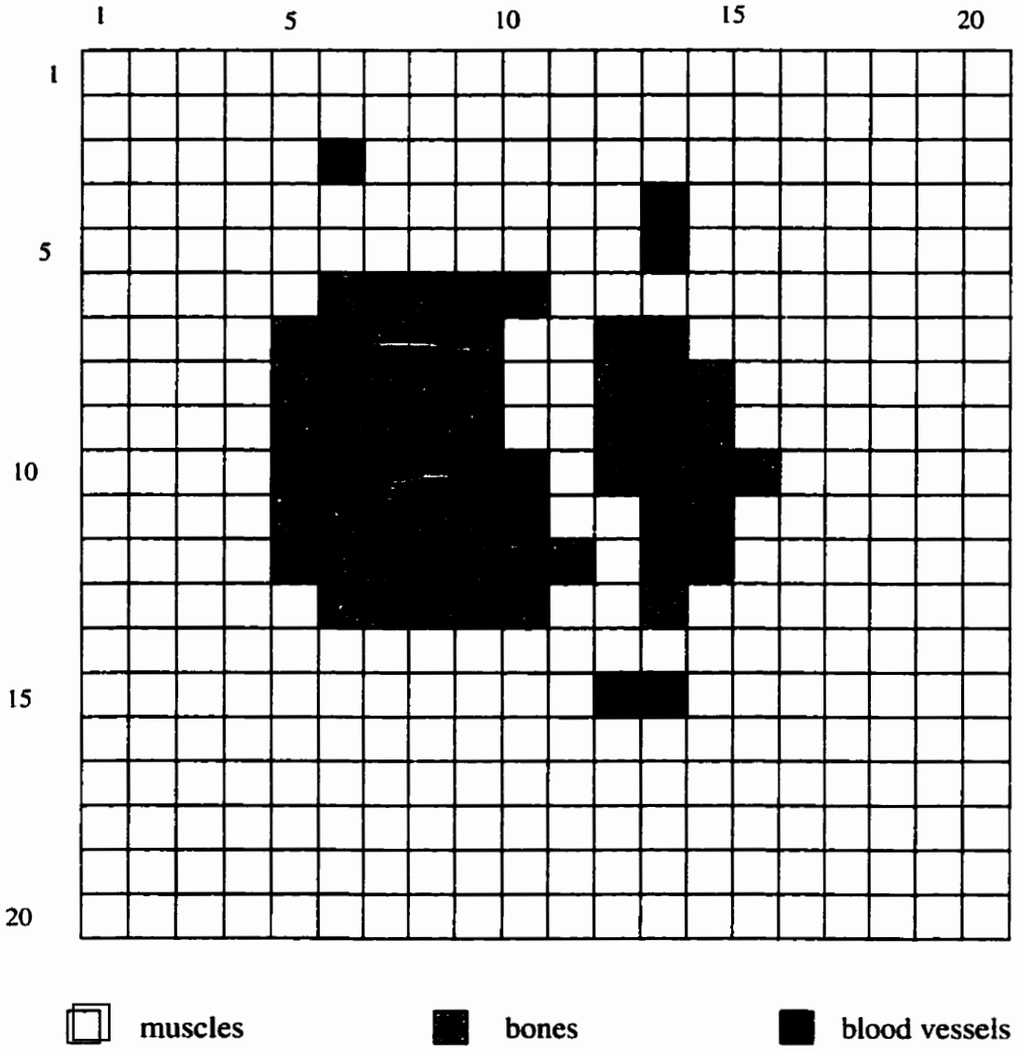

Fig. 8.5 Cross section with bones, blood vessels and muscles.

here, these relations are permitted to be quite different from each other. In the example considered, these relations have been selected randomly as shown in Fig. 8.6. Trapezoidal membership functions have been used here, for illustration, since it is the common

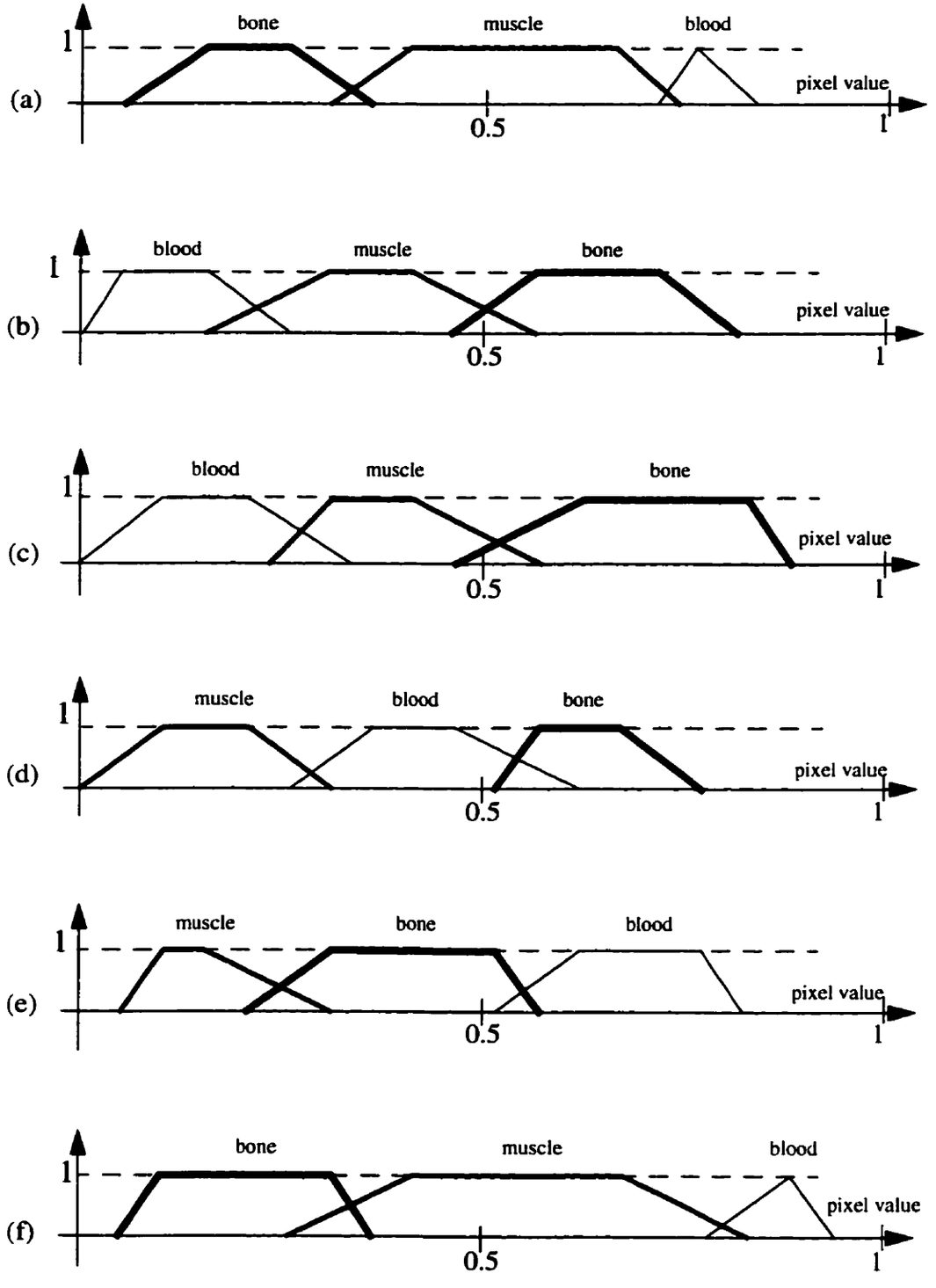

Fig. 8.6 Relation between tissues and pixel values in six different imaging systems, (a) to (f).

practice in fuzzy set theory, although Gaussian distribution functions are more realistic

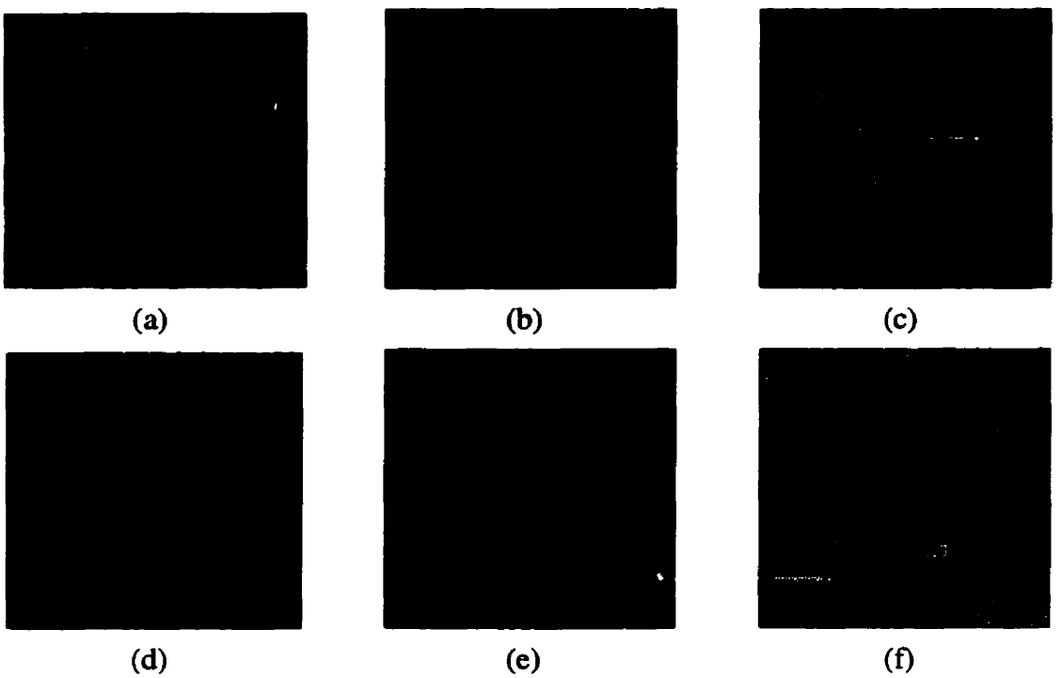

Fig. 8.7 Simulated outputs of the six imaging systems corresponding to Figs. 8.5 and 8.6.

and will be used in practical cases as well as the next example.With these membership functions and with the geometry in Fig. 8.5, one can simulate the resulting image for each imaging system, (a) to (f). To simulate the output images of these imaging systems, one should produce random numbers with trapezoidal pdf's similar to those which were assumed in Fig. 8.6. To do so, here we consider how to produce random numbers with trapezoidal pdf from a uniformly distributed random generator.

At this stage we consider each fuzzy set as a probability density function (pdf) and produce a random number with this pdf for every pixel which belongs to that tissue. A

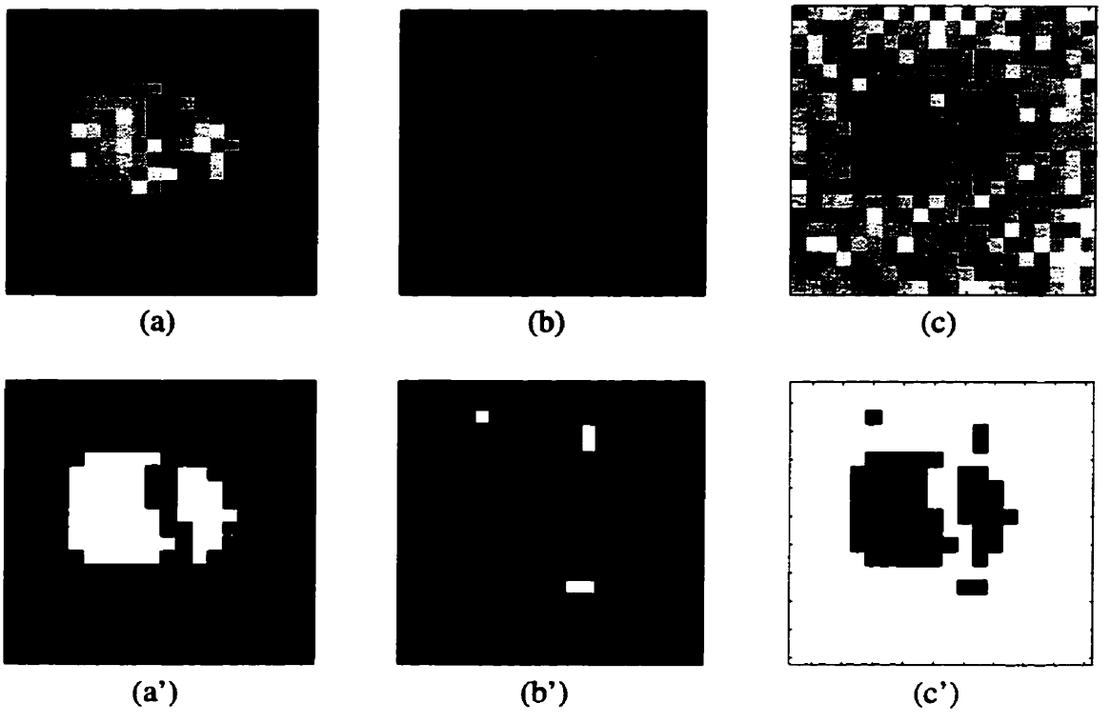

Fig. 8.8 Results by the proposed method: (a), (b) and (c) show bones, blood vessels and muscles, respectively, obtained from averaging; (a'), (b') and (c') give the same tissues after applying a step function mapping to (a), (b) and (c).

uniform distributed random number generator is usually available in most softwares. Therefore we should figure out how to map this random number to our trapezoidal pdf. This has been shown in Appendix D.

Using the method presented in Appendix D, Figure 8.11 shows the corresponding images, where random noise with a triangular probability density function has also been considered within ±5 % of the brightness interval [0,1]. The membership function v^j represents the uncertainty of pixel values and, in accordance with the random noise consid-

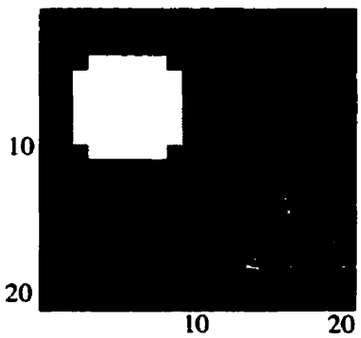

Fig. 8.9 Boundaries of image classes; the regions in white, gray and black have material characteristics of spleen, liver and muscle, respectively.

ered, has been taken to be triangular, with its upper vertex at the pixel value and its lower vertices at 0.05 distance from the pixel value. Systematic measurement errors, if present, can also be considered and compensated by defining suitable membership functions for the relations between tissues and pixel values.

Figure 8.12 shows the results after applying the part 8.3.1 of the proposed method to the simulated output of the imaging systems in Fig. 8.11. In the case considered a simple averaging of the possibility measures and then a non-linear, step function mapping have been performed as the fourth step. The step function maps values above 0.35 to 1 and values below 0.35 to 0. Obviously all tissues have been fully recovered.

8.5 Illustrative Example 2

Consider a 20 by 20 two-dimensional grid for a region containing three different

biological tissues, with material properties corresponding to spleen, liver and muscle, as shown in Fig. 8.13. Assume that an EIT system has been used to produce several images for this region using different injected current frequencies. Since the conductivity and the permittivity of biological tissues are frequency dependent, applying currents of different frequencies produces different images. Four different frequencies have been employed, namely 1 kHz, 10 kHz, 100 kHz and 1 MHz, to produce four different input images. The specific resistance and the specific reactance of the tissues considered at these frequencies are shown in Tables 6 and 7 [109]. The corresponding simulated images are shown in Fig. 8.14. They have been produced using the formula

$$pixel\ value = table\ value\,(bias + random \times noise)\ . \tag{8.1}$$

Table 6: Specific resistance of spleen, liver and muscle at different frequencies [109].

Specific resistance [Ωm]	1 kHz	10 kHz	100 kHz	1 MHz
Spleen	62.9	100	169	360
Liver	114	206	297	469
Muscle	94.3	206	483	583

Table 7: Specific reactance of spleen, liver and muscle at different frequencies [109].

Specific reactance [-Ωm]	1 kHz	10 kHz	100 kHz	1 MHz
Spleen	16.7	55	100	108
Liver	31.7	73.3	102	66.7
Muscle	40	140	127	30

In this formula *table value* refers to the values in Tables 6 and 7, *random* is a normal random variable with a zero mean value and a standard deviation equal to one, *noise* represents the noise level in the measured data and *bias* is modelled as,

$$bias = 1 + f(x, y)\ (spread/2)\ , \tag{8.2}$$

where *spread* accounts for the spread of the actual tissue values with respect to the mean values given in Tables 6 and 7; the larger the value of the *spread*, the more overlap exists between the membership functions corresponding to different tissues. *f(x,y)* is a function of x and y which associates to each point in the image a number in the interval $[-1, 1]$, used to simulate a continuous internal contrast within the tissues. In the example considered, both the spleen and the liver have a specific resistance and a specific reactance that increase with the distance from the coordinate origin, and the muscle has its specific

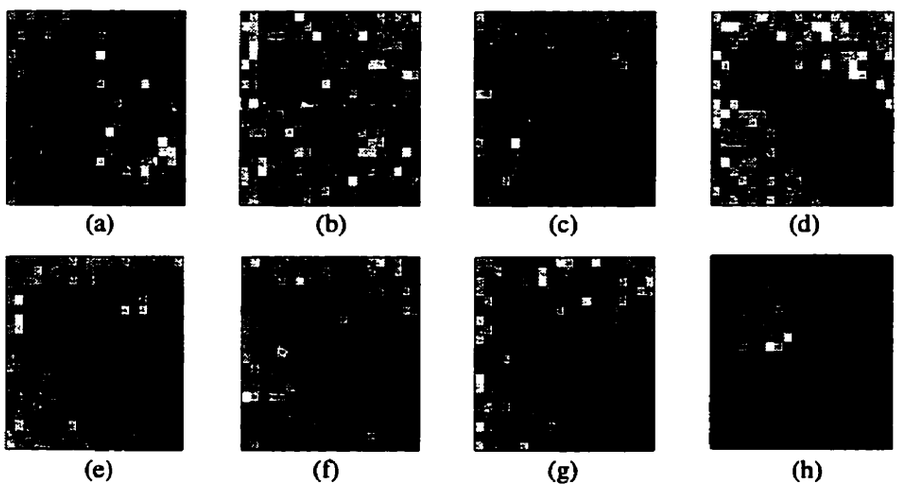

Fig. 8.10 Simulated images using the real part, (a)-(d), and the imaginary part, (e)-(h), of the impedances for an EIT system at four different frequencies, 1 kHz, 10 kHz, 100 kHz and 1MHz, respectively; the *spread* is 0.3 and the *noise* is 0.15.

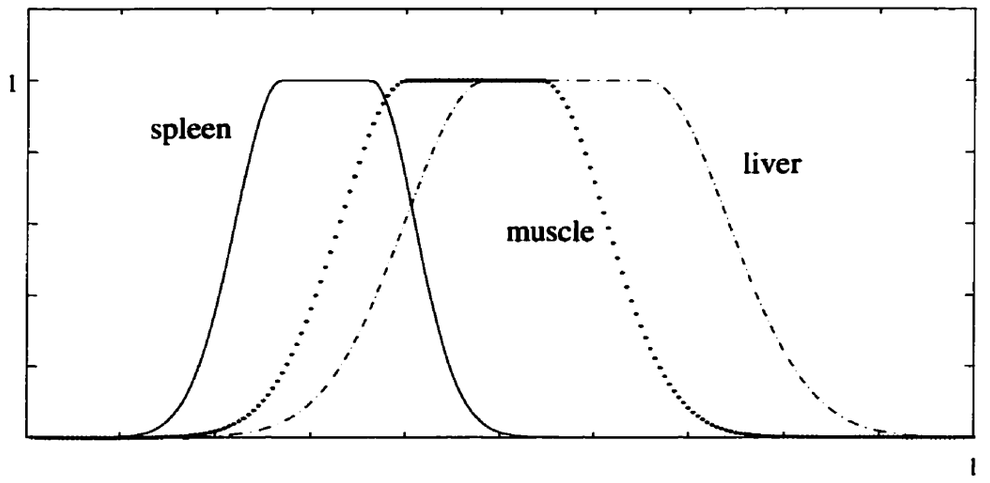

Fig. 8.11 The membership functions for the specific resistances of spleen, liver and muscle versus pixel values at 1 kHz, with *spread* equal to 0.3 and *noise* equal to 0.15 in Eqs. (8.11) and (8.12).

resistance and reactance decreasing with this distance (the coordinate origin is chosen at the top left corner of the grid).

Therefore, a normal random variable is assigned to each pixel such that the pixel value has a mean value equal to the *table value* times the *bias* and a standard deviation σ equal to the *table value* times the *noise*. By doing so, the membership function for a specified tissue would be as shown in Fig. 8.2, with the full membership for values of specific resistance and reactance between (*table value*)(1-*spread*/2) and (*table value*)(1+*spread*/2), and with a Gaussian function dependence outside this interval, $e^{-(x-\mu)^2/(2\sigma^2)}$, where μ is equal to the corresponding value bounding the full membership interval. In Fig. 8.15 membership functions are defined for the specific resistance of spleen, muscle and liver at

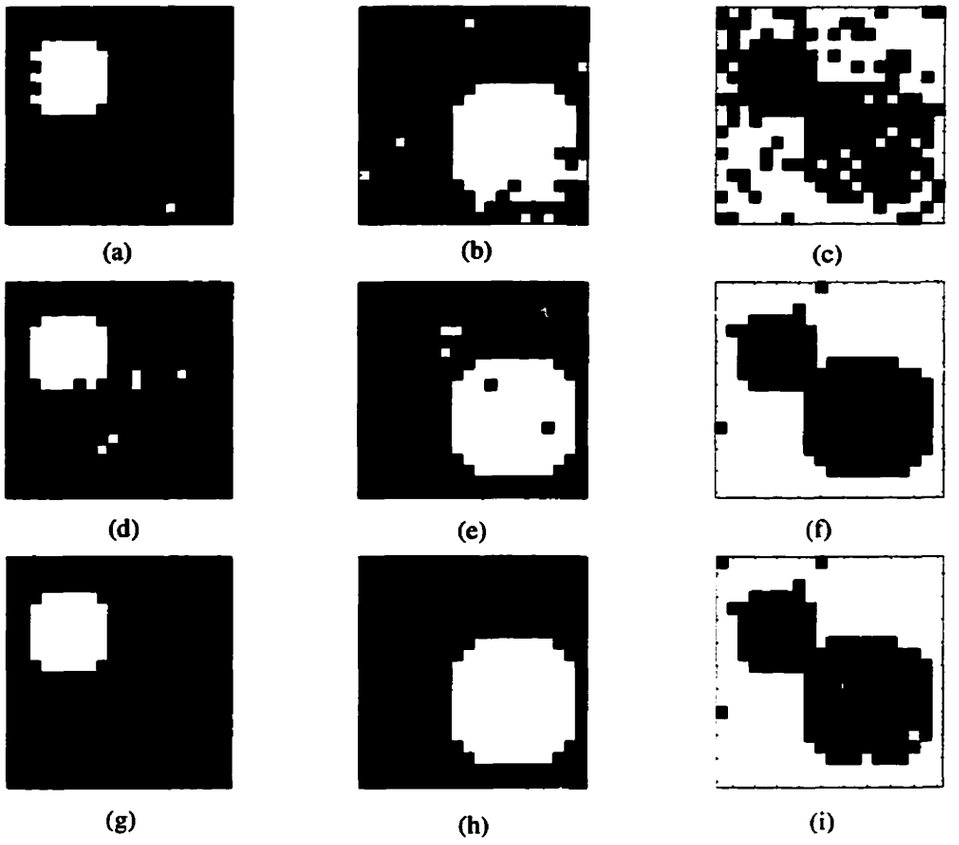

Fig. 8.12 Tissue boundaries after applying part 8.3.1 of the proposed method using the input images in Fig. 8.11, with a *spread* of 0.3 and a *noise* of 0.15 in Eqs. (8.11) and (8.12): (a)-(c) are from images using the real part of impedances; (d)-(f) are from images using the imaginary part of impedances; (g)-(i) are obtained using all the images in Fig. 8.14.

1 kHz with a *spread* equal to 0.3 and a *noise* equal to 0.15. Increasing the *spread* and the *noise* yields an increased overlap between these membership functions.

The results after applying the part 8.3.1 of the processing approach to simulated images in Fig. 8.14 are presented in Fig. 8.16. A simple averaging of the possibility measures and a thresholding have been employed to produce these results. Applying averaging yields values for pixels associated with a specified class that are normally greater than

those for pixels belonging to other classes. However, the difference between these values could be too small to distinguish clearly the boundaries of the class considered. The thresholding is applied in order to map the values below a specified level (here 0.75) to zero and the values above this level to one By doing this, only the pixels with values equal to one are identified to belong to class i. The threshold value is mainly determined by the degree of overlap between membership functions of different classes. It can be adjusted by applying the same procedure to a number of images with similar overlaps, whose contents are known, until the results generated are satisfactorily accurate. A careful examination of Fig. 8.16 (g) to (i) shows that some pixels have not been assigned to any of the three classes and some other pixels have been assigned to more than one class. These contradictory results allow the interpreter to know that the fusion attempt was not successful for those pixels due to insufficient input data.

Several simulations have been executed with a *spread* equal to 0.3 and a *noise* equal to 0.15,. The corresponding statistical measures are summarized in Table 8. For another round of simulations, with even higher values of *spread* and *noise*, statistical measures are given in Table 9. These results show that even under quite severe noise conditions and large overlap of different tissues, the processing approach produces excellent results.

To restore the internal contrast within each tissue one can use either the raw data or, to obtain better results, the data from part 8.3.1 of the proposed method. Obviously, the internal contrast can be restored from raw data only when the *spread* and the *noise* are sufficiently small. Figure 8.17 shows the simulated input images with a *spread* of 0.2 and a *noise* of 0.05, and Fig. 8.18 shows the results when applying only part 8.3.2 to the input

images in Fig. 8.17 (i.e. to the raw data). The following formula has been employed for postprocessing the data in the proposed method:

$$pixel\ \ value_i = max\left(ave_i - \frac{1}{n}\sum_{j=1}^{n}\left(ave_i - Poss\left(\lambda_i^j(x), v^j(x)\right)\right)^2, 0\right) \tag{8.3}$$

where

$$ave_i = \frac{1}{n}\sum_{j=1}^{n} Poss\left(\lambda_i^j(x), v^j(x)\right) \tag{8.4}$$

It should be noted that due to noise, the possibility measures for some pixels in a given imaging system may have unexpected large values even though these pixels do not belong to the class considered. By using this formula the effect of such possibility measures in the overall pixel value is substantially reduced.

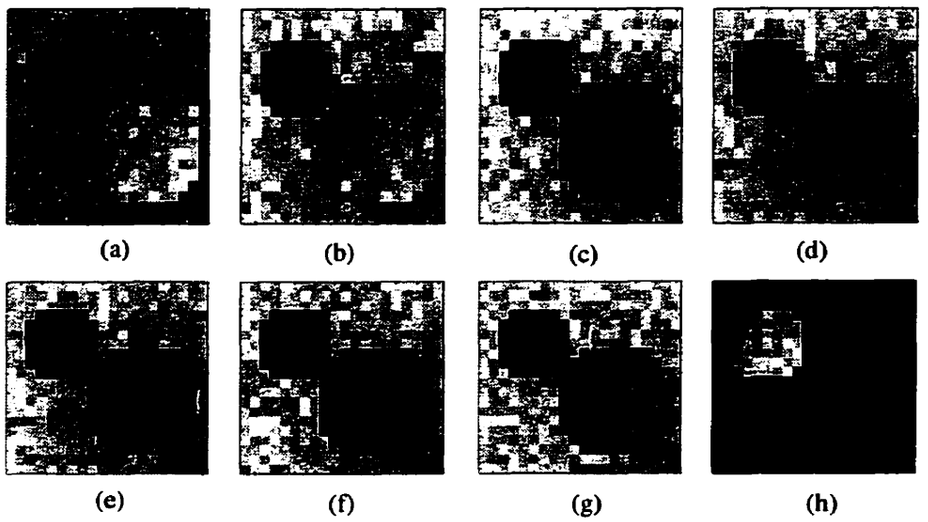

Fig. 8.13 Simulated images for the object in Fig. 8.13 to be used in the part 8.3.2 of the proposed method, with a *spread* of 0.2 and a *noise* of 0.05: (a)-(d) using the real part of impedances; (e)-(h) using the imaginary part of impedances.

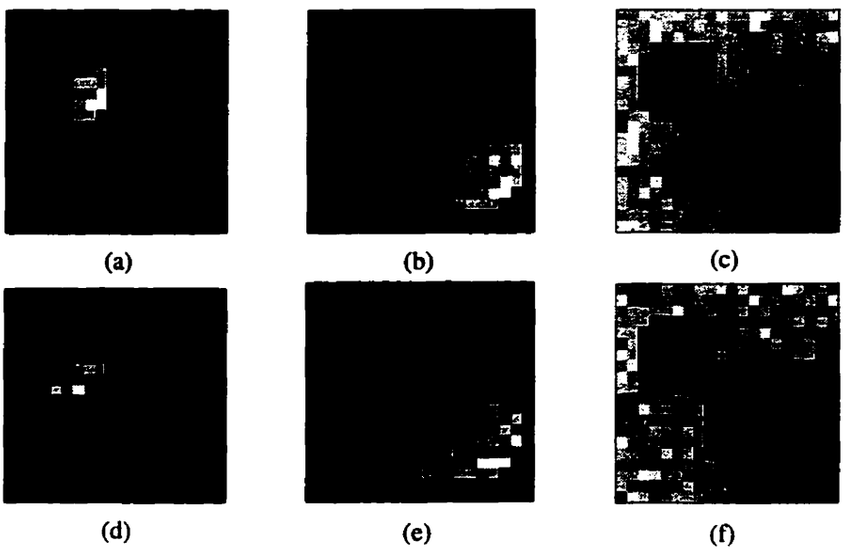

Fig. 8.14 Internal contrast reconstruction when applying only the part 8.3.2 to simulated input images in Fig. 8.17, for a *spread* of 0.2 and a *noise* of 0.05: (a)-(c) with the real part of impedances; (d)-(f) with the imaginary part of impedances.

Table 8: Errors for 10 simulations with *spread* of 0.3 and *noise* of 0.15: arithmetic mean (M) and standard deviation (SD) - Part 8.3.1 in the proposed method.

Tissue	Input images from	M [%]	SD
Spleen	Resistance	0.15	0.1748
	Reactance	0.9	0.5426
	Resistance and reactance	0.05	0.1054
Liver	Resistance	5.55	0.8882
	Reactance	1.55	0.4048
	Resistance and reactance	0.3	0.2297
Muscle	Resistance	19.425	2.2362
	Reactance	0.975	0.5062
	Resistance and reactance	1.45	0.5503

Figure 8.19 shows another set of simulated input images obtained with high values of *spread* and *noise*, 0.3 and 0.15, respectively. The internal contrast is restored by applying the procedure in part 8.3.2 to the results from the part 8.3.1 of the proposed method. The resulting images are presented in Fig. 8.20. It can be seen that not only different tissues have been clearly classified, but also the internal contrast within the three tissues has been preserved and in fact augmented.

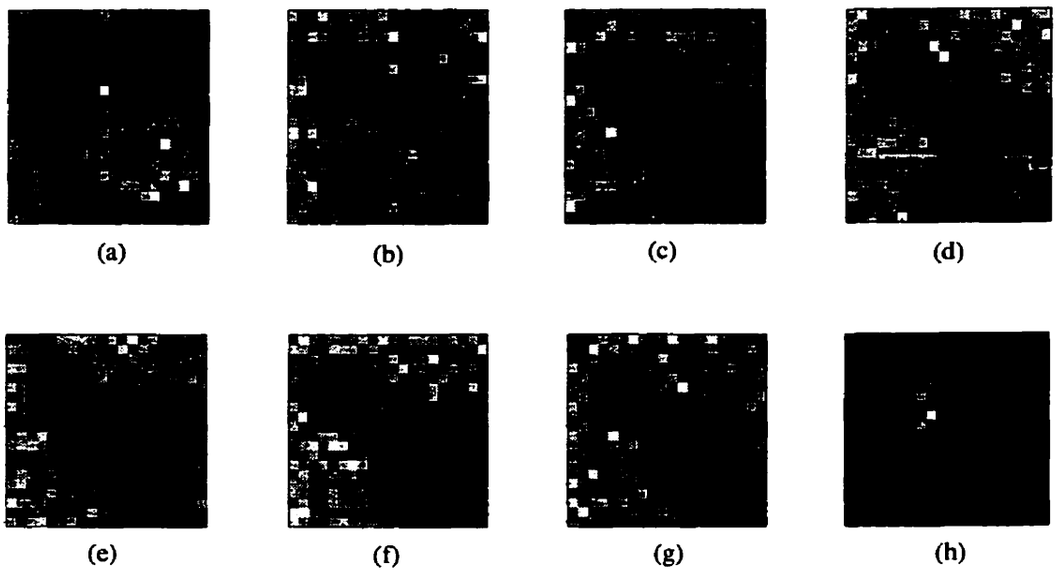

Fig. 8.15 Simulated input images to be used in both parts 8.3.1 and 8.3.2 of the method, with a *spread* of 0.3 and a *noise* of 0.15: (a)-(d) with the real part of impedances; (e)-(h) with the imaginary part of impedances.

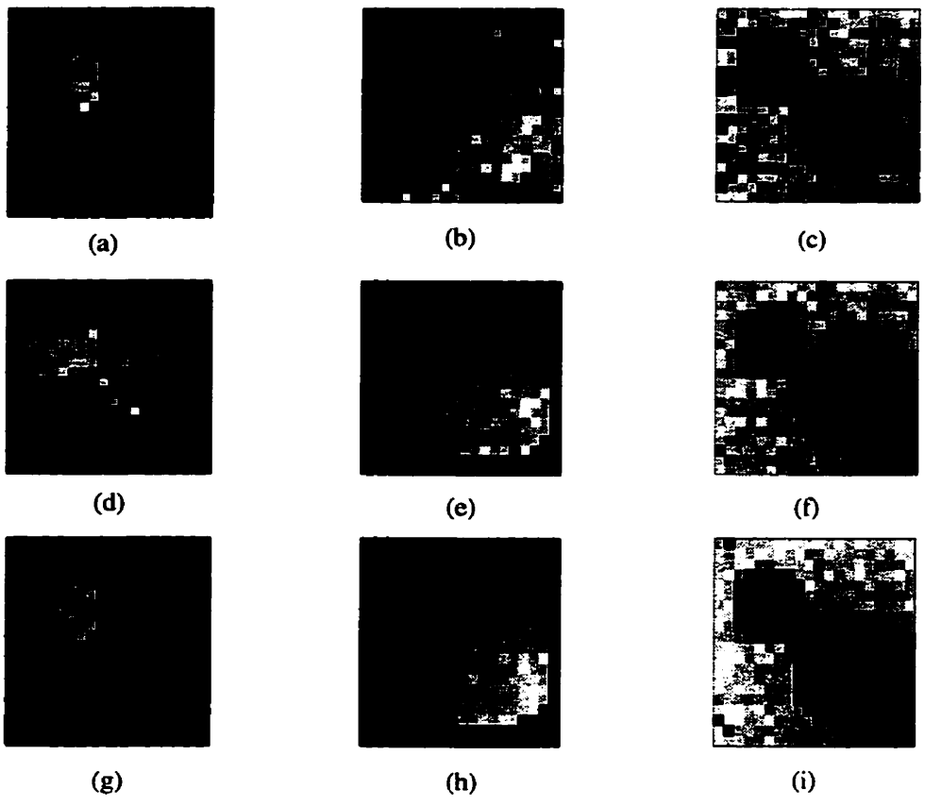

Fig. 8.16 Fused images obtained by applying part 8.3.2 of the proposed method to tissues classified in part 8.3.1, with a *spread* of 0.3 and a *noise* of 0.15: (a)-(c) using the real part of impedances; (d)-(f) using the imaginary part of impedances; (g)-(i) using all the input images from both the real and the imaginary parts of impedances.

Table 9: Errors for 10 simulations with *spread* of 0.4 and *noise* of 0.2: arithmetic mean (M) and standard deviation (SD) - Part 8.3.2 in the proposed method.

Tissue	Input images from	M [%]	SD
Spleen	Resistance	2.575	0.8901
	Reactance	4.975	1.0701
	Resistance and reactance	0.775	0.5464
Liver	Resistance	13.925	1.3847
	Reactance	3.175	0.7551
	Resistance and reactance	2.225	0.8203
Muscle	Resistance	26.3	2.1692
	Reactance	5.725	1.0766
	Resistance and reactance	6.975	1.5962

8.6 Conclusion

A new method for image fusion using fuzzy set theory has been proposed which allows different components of the input images to be clearly classified and the internal contrast within image classes to be restored and emphasized. The method is easy to implement and the resulting images can be readily interpreted and is also applicable to situations where the relations between tissues and pixel values for different imaging systems lack similarity and thus the fuzzy classification technique [12] is not applicable. The presented results have been produced without using any *a priori* information, i.e., the same weights have been assigned to all input images, independently of how accurate they are. In most practical cases when this information is available, even better results can be achieved.

9. CONCLUSIONS AND SUGGESTIONS FOR FUTURE RESEARCH

9.1 Main Contributions in the Thesis

In this dissertation research the performance of EIT systems has been improved by three basic propositions. They are namely, the forward problem, the inverse problem and the image processing. Advantages of each of them over existing methods are summarized as follows.

The network approximation method introduced in Chapter 5 has obvious advantages on previous models in network approximation by producing a smaller nodal admittance matrix. It also has the capability to simulate wide area electrodes without any approximation and to consider permittivity without increasing the computational burden over finite element method. It is easy to implement and produces accurate results.

For the first time neural networks have been utilized in an iterative scheme to solve the inverse problem. In the proposed method, a two-layer backpropagation neural networks with tangent hyperbolic activation function for the units in the hidden layer and linear units in the output layer have been trained appropriately to solve the highly nonlinear problem of reconstruction of conductivity distribution inside the object based on measured electrode voltages and known injecting current patterns. The proposed method has the ability to produce accurate static images with computation times that in comparison to other existing methods are several times shorter. Moreover, its performance can be

increased considerably using other advantages of neural networks which include hardware realization that further increases the speed as well as robustness in presence of noise. The proposed method can also be implemented in order to solve other inverse problems encountered in the inverse scattering of acoustic or electromagnetic waves.

Although the multi-frequency scheme in order to increase the accuracy of EIT systems is not a new idea, there has not been any method to appropriately address the fusion problem. In this thesis, a new method is proposed based on fuzzy set theory that is well suited for this problem. The method is quite straightforward and easy to apply and not only classifies different classes in the object but also, preserves and enhances the internal contrast, all of them in the presence of noise and other measurement errors. This method can also be implemented in other image fusion problems, i.e. specially when the images are produced using different modalities and classical image fusion methods are not applicable.

9.2 Suggestions for Future Research

The solution of the forward problem using neural networks produced fruitful and promising results. Nevertheless, the training episode which has to be done only once and in advance is an extensive computational burden. In this thesis, in order to concentrate on the method rather than become involved in the programming aspects of the technique, the inverse problem was solved for a small size problem and only the conductivity distribution was considered. However, the method can be expanded to practical size problems without any major alteration. To do so, more powerful machines and optimum softwares, have to be employed for the training of the neural networks. Here, to shorten the training

episode and at the expense of more memory, linear units were used in the output layer of the network. Another option would be to use smaller networks with non-linear units in the both hidden and output layer, provided better software and hardware are utilized.

The last but not the least step would be to perform practical experiments to implement the proposed methods.

10. REFERENCES

[1] M. A. Abidi and R. C. Gonzalez, *Data Fusion in Robotics and Machine Intelligence*. Boston, MA: Academic, 1992.

[2] J. Ackmann and M. Seitz, "Methods of complex impedance measurements in biologic tissue," *Crit. Rev. Biomed. Eng.*, vol. 11, pp. 281-311, 1984.

[3] A. Adler and R. Guardo, "A neural network image reconstruction technique for electrical impedance tomography," *IEEE Trans. Medical Imag.*, vol. 13, no. 4, pp. 594-600, Dec. 1994.

[4] H. Akaike, "A new look at statistical model identification," *IEEE Trans. Automat. Contr.*, vol. 19, pp. 16-30, 1974.

[5] D. C. Barber, B. H. Brown, and J. L. Freeston, "Imaging spatial distributions of resistivity using applied potential tomography," *Electron. Lett.*, vol. 19, pp. 933-935, 1983.

[6] D. C. Barber and B. H. Brown, "Applied potential tomography," *J. Phys. E:Sci. Instrum.*, vol. 17, pp. 723-733, 1984.

[7] D. C. Barber and B. H. Brown, *Information Processing in Medical Imaging*. S. Bacharach, Dordrecht: Martinus-Nijhoff, pp 446-462, 1986.

[8] D. C. Barber and B. H. Brown, "Errors in reconstruction of resistivity images using a linear reconstruction technique," *Clin. Phys. Physiol. Meas.*, vol. 9, suppl.

A, pp. 101-104, 1988.

[9] D. C. Barber and A. D. Seager, "Fast reconstruction of resistive images," *Clin. Phys. Physiol. Meas.*, vol. 8, suppl. A, pp. 47-54, 1987.

[10] Y. Bard, "Comparison of gradient methods for the solution of nonlinear parameter estimation problems," *SIAM J. Numer. Anal.*, vol. 7, pp. 157-86, 1970.

[11] D. P. Blair and P. H. Syndenham, "Phase sensitive detection as a means to recover signals buried in noise," *J. Phys. E: Sci. Instrum.*, vol. 8, pp. 621-627, 1975.

[12] I. Bloch, "Fuzzy classification for multi-modality image fusion", in *Proc. IEEE Int. Conf. on Image Processing*, vol. 1, pp. 628-632, Austin TX, Nov. 1994.

[13] I. Bloch and H. Maitre, "Constructing a fuzzy mathematical morphology: alternative ways", in *Proc. IEEE Int. Conf. on Fuzzy Systems*, pp. 1303-1308, San Francisco, CA, 1993.

[14] R. S. Blum, S. A. Kassam, and H. V. Poor, "Distributed detection with multiple sensors: part II--Advanced topics," in *Proc. of the IEEE*, vol. 85, no. 1, pp. 64-79, Jan. 1997.

[15] W. Breckon and M. Pidcock, "Data errors and reconstruction algorithms in electrical impedance tomography," *Clin. Phys. Physiol. Meas.*, vol. 9, suppl. A, pp. 51-58, 1988.

[16] B. H. Brown and D. C. Barber, "Recent development in applied potential tomography-APT," in *Proc. 1985 9th Conf. Inform. Process. in Med. Imaging*, Washington, DC, pp. 106-121.

[17] B. H. Brown, A. D. Leathard, L. Lu, W. Wang, and A. Hampshire, "Measured and expected Cole parameters from electrical impedance tomographic spectroscopy

images of the human thorax," *Physiol. Meas.*, vol. 16, pp. A57-A67, 1995.

[18] B. H. Brown, D. C. Barber, and A. D. Seagar, "Applied potential pomography: Possible clinical applications," *Clin. Phys. Physiol. Meas.*, vol. 6, no. 2, pp. 109-121, 1985.

[19] B. H. Brown and A. D. Seager, "Applied potential tomography- data collection problems," *IEE Conf. Publ.*, vol. 257, pp. 79-82, 1985.

[20] B. H. Brown and A. D. Seager, "The sheffield data collection system," *Clin. Phys. Physiol. Meas.*, vol. 8, suppl. A, pp. 91-97, 1987.

[21] G.A. Carpenter and S. Grossberg, eds., *Pattern recognition by self-organizing neural networks*. Cambridge, Mass.: MIT Press, 1991.

[22] K. S. Cheng, S. J. Simske, D. Issacson, J. C. Newel, and D. G. Gisser, "Errors due to measuring voltage on current-carrying electrodes in electric current computed tomography," *IEEE Trans. Biomed. Eng.*, vol. 37, pp. 60-65, Jan. 1990.

[23] J. Conway, "Electrical impedance tomography for thermal monitoring of hyperthermia treatment: an assessment using *in vitro* and *in vivo* measurements," *Clin. Phys. Physiol. Meas.*, vol. 8, suppl. A, pp. 141-6, 1987.

[24] R. D. Cook, G. J. Saulnier, D. G. Gisser, J. C. Goble, J. C. Newell, and D. Issacson. "ACT3: A high-speed, high-precision electrical impedance tomograph." *IEEE trans. Biomed. Eng.*, vol. 41, no. 8, pp. 713-722, 1994.

[25] M. M. Daniel and A. S. Willsky, "A multiresolution methodology for single-level fusion and data assimilation with applications to remote sensing," in *Proc. of the IEEE*, vol. 85, no. 1, pp. 164-183, Jan. 1997.

[26] B. V. Dasarathy, "Sensor fusion potential exploitation--Innovative architectures

and illustrative applications," in *Proc. of the IEEE*, vol. 85, no. 1, pp. 24-38, Jan. 1997.

[27] B. V. Dasarathy, "Fuzzy evidential reasoning approach to target identity and state fusion in multisensor," *Opt. Eng.*, vol. 36, no. 3, pp. 669-683, March 1997.

[28] S. G. Dawids, "Evaluation of applied potential tomography: a clinician's view," *Clin. Phys. Physiol. Meas.*, vol. 8, suppl. A, pp. 175-80, 1987.

[29] J. C. Denniston and L. E. Baker, "Measurement of urinary bladder emptying using electrical impedance," *Med. Biol. Eng.*, vol. 13, pp. 305-6, 1975.

[30] K. A. Dines and R. J. Lytle, "Analysis of electrical conductivity imaging," *Geophysics*, vol. 46, no. 7, pp. 1025-1036, July 1981.

[31] W. S. Druz and J. T. Sharp, "Activity of respiratory muscles in upright and recumbent humans," *J. Appl. Physiol.*, vol. 51, pp. 1552-1561, 1981.

[32] P. M. Duggan and T. A. York, "Tomographic Image reconstruction using RAM-based neural networks," in *Proc. 1995 of the Vth European Concerted Action on Process Tomography Workshop*, Norway, pp. 203-207.

[33] P. M. Duggan and T. A. York, "RAM-based neural networks for image reconstruction in process Tomography," *Digest of IEE Computer and Control Division Colloquium Innovation in Instrumentation for Electrical Tomography*, no. 99, pp. 4/1-4/5, 1995.

[34] B. Eyuboglu, D. C. Barber, and B. H. Brown, "Limitations to SV determination from APT images," in *Proc. 1989 IEEE 11th Annu. Conf. Eng. Med. Biol. Soc.*, pp. 442-443.

[35] B. M. Eyuboglu, B. H. Brown, D. C. Barber, and A. D. Seagar, "Localisation of

the cardiac related impedance changes in the thorax," *Clin. Phys. Physiol. Meas.*, vol. 8, suppl. A, pp. 163-73, 1987.

[36] S. Feliu, J.C. Galvan, and M. Morcillo, "Interpretation of electrical impedance diagrams for painted galvanized steel," *Prog. in Organic Coatings*, vol. 17, no. 2, pp. 143-153, 1989.

[37] L. F. Fuke, M. Cheney, D. Isaacson, D. Gisser, and J. C. Newell, "Detection and imaging of electric conductivity and permittivity at low frequency", *IEEE Trans. Biomed. Eng.*, vol. 38, no. 11, pp. 1106-1110, Nov. 1991.

[38] L. A. Geddes, *Electrodes and Measurement of Bioelectric Events*, New York, NY: Wiley-Interscience, 1972.

[39] H. Fricke and S. Morse, "The electric capacity of tumours of the breast," *J. Cancer. Res.*, vol. 10, pp. 340-76, 1926.

[40] L. A. Geddes and L. E. Baker, *Principles of Applied Biomedical Instrumentation*, 3rd ed., New York, NY: John Wiley, 1989.

[41] P. Gilbert, "Iterative methods for the reconstruction of three dimensional objects from projections," *Theoret. Biol.*, vol. 36, pp. 105-117, 1972.

[42] D. G. Gisser, D. Issacson, and J. C. Newell, "Current topics in impedance imaging," *Clin. Phys. Physiol. Meas.*, vol. 8, suppl. A, pp. 39-47, 1987.

[43] J. C. Goble and T. D. Gallagher, "A distributed architecture for medical instrumentation: An electric current tomograph," in *Proc. 1988 IEEE Eng. Med. Biol. Soc.*, pp. 285-286.

[44] G. H. Golub and C. Reinsch, "Singular value decomposition and least squares solutions," *Numer. Math.*, vol. 14, pp. 403-420, 1970.

[45] G. H. Golub and C. F. Van Loan, *Matrix Computations*. Baltimore, MD: The John Hopkins University Press, 1983.

[46] R. Gonzalez and R. Woods, *Digital Image Processing*. Reading, MA: Addison-Wesley, 1992.

[47] B. S. Gottfried and J. Weisman, *Introduction to Optimization Theory*, Englewood Clifs, NJ: Prentice-Hall, 1973.

[48] O. D. Grace and S. P. Pitt, "Sampling and interpolation of bandlimited signals by quadrature methods." *J. Accost. Soc. Emir.*, vol. 48, pp. 1311-1318, 1970.

[49] H. Griffiths, "The importance of phase measurement in electrical impedance tomography" *Phys. Med. Biol.*, vol. 32, pp. 1435-1444, 1987.

[50] H. Griffiths and A. Ahmed, "A dual frequency applied potential tomography technique: computer simulations," *Clin. Phys. Physiol. Meas.*, vol. 8, suppl. A, pp. 103-107, 1987.

[51] H. Griffiths and A. Ahmed, "Applied potential tomography for non invasive temperature mapping in hyperthermia," *Clin. Phys. Physiol. Meas.*, vol. 8, suppl. A, pp. 147-53, 1987.

[52] H. Griffiths, J. Antal, and A. Ahmed, "Non invasive thermometry using applied potential tomography," *Strahlentherapie*, vol. 161, p. 534, 1985.

[53] H. Griffiths and Z. Zhang, "Dual frequency electrical impedance tomography in vitro and in vivo," in *Proc. 1989 IEEE Eng. Med. Biol. Soc.*, pp. 476-477.

[54] R. Guardo, C. Boulay, and M. Bertrand, "A neural network approach to image reconstruction in electrical impedance tomography," in *Proc. 1991 IEEE 13th Annu. Conf. Eng. Med. Biol. Soc.*, no. 1, pp. 14-15.

[55] D. L. Hall, *Mathematical Techniques in Multisensor Data Fusion*. Boston, MA: Artech House, 1992.

[56] D. L. Hall and J. Llinas, "A survey of data fusion systems," in *Proc. SPIE Conf. on Data Structure and Target Classification*, vol. 1470, pp. 13-36, Orlando, FL, Apr. 1991.

[57] D. L. Hall, and J. Llinas, "An introduction to multisensor data fusion", in *Proc. of the IEEE*, vol. 85, no. 1, pp 6-23, Jan. 1997.

[58] A. R. Hampshire, R. H. Smallwood, B. H. Brown, and R. A. Primhak, "Multifrequency and parametric EIT images of neonatal lungs," *Physiol. Meas.*, vol. 16, pp. A175-A189, 1995.

[59] N. D. Harris, A. J. Suggett, D. C. Barber, and B. H. Brown, "Applications of applied potential tomography (APT) in respiratory medicine," *Clin. Phys. Physiol. Meas.*, vol. 8, suppl. A, pp. 155-165, 1987.

[60] R. P. Henderson and G. J. Webster, "An impedance camera for spatially specific measurements of the thorax," *IEEE Trans. Biomed. Eng.*, vol. 25, no 3, pp. 250-254, May 1978.

[61] P. Hua, J. G. Webster, and W. J. Tompkins, "Effect of measurement method on noise handling and image equality of EIT imaging" in *Proc. 1987 IEEE Annu. Int. Conf. Eng. Med. Biol. Soc.*, vol. 9, pp. 1429-1430.

[62] P. Hua, E. J. Woo, J. G. Webster, and W. J. Tompkins, "Using compound electrodes in impedance tomography," *IEEE Trans. Biomed. Eng.*, vol. 40, no. 1, pp. 29-34, Jan. 1993.

[63] P. Hua, J. G. Webster, and W. J. Tompkins, "A regularised electrical impedance

tomography reconstruction algorithm," *Clin. Phys. Physiol. Meas.*, vol. 8, suppl. A, pp. 137-141, 1988.

[64] P. Hua, E. J. Woo, J. G. Webster, and W. J. Tompkins, "Improved methods to determine optimal currents in electrical impedance tomography," *IEEE Trans. Medical Imaging*, vol. 11, no. 4, pp. 488-495, Dec. 1992.

[65] P. Hua, E. J. Woo, J. G. Webster, and W. J. Tompkins, "Finite element modelling of electrode-skin contact impedance in electrical impedance tomography," *IEEE Trans. Biomed. Eng.*, vol. 40, no. 4, pp. 335-343, 1993.

[66] Y. Z. Ider, C. Altan, E. Atalar, and N. G. Gencer, "Electrical impedance imaging system applicable to objects of arbitrary but known boundary," in *Proc. 1987 IEEE Annu. Int. Conf. Eng. Med. Biol. Soc.*, vol. 9, pp. 1427-1428.

[67] Y. Z. Ider, E. Dorken, N. G. Gencer, and H. Koymen, "A dual modality imaging system for impedance tomography with ultrasonically determined boundaries," in *Proc. 1988 IEEE Annu. Conf. Eng. Med. Biol. Soc.*, no. 10, pp. 283-284.

[68] D. Issacson, "Distinguishability of conductivities by electric current computed tomography," *IEEE Trans. on Medical Imaging*, vol. 5, no. 2, pp. 91-95, June 1986.

[69] J. Jossinet, J. P. Marques de Sa, J. Nuno Lau, L. P. Reis, and C. Trillaud. "Pattern recognition in raw data of electrical impedance tomography using neural networks," in *Proc. 1993 IEEE Annu. Int. Conf. Eng. Med. Biol. Soc.*, vol. 14, pp. 76-77.

[70] M. Kam, X. Zhu, and P. Kalata, "Sensor fusion for mobile robot navigation," in *Proc. of the IEEE*, vol. 85, no. 1, pp. 108-119, Jan. 1997.

[71] Y. Kim, J. G. Webster, and W. J. Tompkins, "Electrical impedance tomography of the thorax," *J. Microwave Power*, vol. 18, pp. 245-257, 1983.

[72] Y. Kim, H. W. Woo, T. J. Brooks, and S. O. Elliot, "Electrical impedance techniques in medical imaging: a feasibility study," *J. Clin. Eng.*, vol. 12, pp. 221-231, 1987.

[73] Y. Kim and H. W. Woo, "A prototype system and reconstruction algorithm for electrical impedance technique in medical body imaging," *Clin. Phys. Physiol. Meas.*, vol. 8, suppl. A, pp. 63-71, 1987.

[74] L. A. Klein, *Sensor and Data Fusion Concepts and Applications*, SPIE Opt. Engineering Press, Tutorial Texts, vol. 14, 1993.

[75] R. V. Kohn and M. Vogelius, "Relaxation of a variational method for impedance computed tomography," Department of Mathematics, Univ. of Maryland, 1987.

[76] C. J. Kotre, "A sensitivity coefficients method for the reconstruction of electrical impedance tomography," *Clin. Phys. Physiol. Meas.*, vol. 10, pp. 275-281, 1989.

[77] V. Kulkarni, J. Hutchison, I. K. Ritchie, R. Chesney, P. Gibson, and J. Mallard, "Monitoring fracture healing by impedance imaging," in *Proc. 1989 IEEE Annu. Int. Conf. Eng. Med. Biol. Soc.*, vol. 11, pp. 478-479.

[78] C. L. Lawson and R. J. Hanson, *Solving Least Square Problems*. Englewood Cliffs, NJ: Prentice-Hall, 1974.

[79] F. M. Liebman, "Electrical impedance pulse tracings from pulsatile blood flow in rigid tubes and volume restricted vascular beds," *Annu. N. Y. Acad. Sci.*, vol. 170. pp. 437-51, 1970.

[80] J. Llinas and E. Waltz, *Multisensor Data Fusion*. Boston, MA: Artech House,

1990.

[81] A. E. Luedtke, H. W. Woo, and Y. Kim, "Electrical impedance tomography for noninvasive detection of DVT in human calf," in *Proc. 1987 IEEE Annu. Conf. Eng. Med. Biol. Soc.*, vol. 9, pp. 1431-2.

[82] Y. F. Mangmall, A. J. Baxter, R. Avill, N. C. Bird, B. H. Brown, D. C. Seagar, A. J. Johnson, and N. W. Read, "Applied potential tomography: a new non-invasive technique for assessing gastric function," *Clin. Phys. Physiol. Meas.*, vol. 8, suppl. A, pp. 119-29, 1987.

[83] D. W. Marquardt, "An algorithm for least squares estimation for nonlinear parameters," *SIAM J. Appli. Math.*, 11, pp. 431-41, 1963.

[84] *MATLAB User's Guide*, The MathWorks, Inc., 1995.

[85] F. J. McArdle, B. H. Brown, and A. Angel, "Imaging sensitivity changes of the adult brain during the cardiac cycle." in *Proc. 1989 IEEE Annu. Conf. Eng. Med. Biol. Soc.*, vol. 11, pp. 480-481.

[86] G. R. McClelland and J. Sutton, "Epigastric impedance: a non invasive method for the assessment of gastric emptying and motility," *Gut.*, vol. 26, pp. 207-214, 1985.

[87] B. A. Mineo, "A portable non invasive ultrasonic bladder sensor for incontinence," in *Proc. 1986 IEEE Annu. Conf. Eng. Med. Biol. Soc.*, vol. 8, pp. 1864-1867.

[88] T. Murai and Y. Kagayawa, "Electrical impedance tomography based on finite element model," *IEEE Trans. Biomed. Eng.*, vol. 32, pp. 177-184, 1985.

[89] D. Murphy, P. burton, R. Coombs, L. Tarassenko, and P. Rolfe, "Impedance imaging in the newborn," *Clin. Phys. Physiol. Meas.*, vol. 8, suppl. A, pp. 131-140, 1987.

[90] K. Nakayama, W. Yagi, and S. Yagi, "Foundamental study on electrical impedance CT algorithm utilizing sensitivity theorem on impedance plethsmography." in *Proc. 1981 5th Int. Conf. on Electrical Bio-impedance (ICEBI)*, pp. 99-102.

[91] A. Nejatali, I. R. Ciric, and W. v. d. Putten, "Network approximation for solving the forward problem in electrical impedance tomography," in *Proc. 4th Iranian Conf. on Elec. Eng.*, Tehran, Iran, May 1996, pp. 577-584.

[92] A. Nejatali, I. R. Ciric, and W. v. d. Putten, "Image fusion technique using fuzzy sets", in *Proc. of Symp. on Antenna Tech. and Applied Electromag., ANTEM'96*, pp. 103-106, Montreal, Canada, Aug. 1996.

[93] A. Nejatali and I. R. Ciric, "Preserving internal contrast in image fusion using fuzzy sets theory", in *Proc. IEEE Canadian Conf. on Elec. and Comp. Eng.*, pp. 611-613, St. John's, NF, Canada, May 1997.

[94] A. Nejatali and I. R. Ciric, "Impedance image reconstruction using neural networks", *International Symposium sponsored by the IEEE Antennas and Propagation Society (AP-S)*, pp. 1376-1379, Montreal, Canada, July 13-18, 1997.

[95] A. Nejatali and I. R. Ciric, "An iterative algorithm for electrical impedance imaging using neural networks," *IEEE Conf. on the Computation of Electromag. Fields COMPUMAG*, Rio de Janeiro, Brazil, Nov. 1997.

[96] A. Nejatali and I. R. Ciric, "Novel image fusion methodology using fuzzy set theory," *Optical Engineering*, submitted.

[97] A. Nejatali and I. R. Ciric, "Solving the inverse problem in electrical impedance imaging using an iterative algorithm employing neural networks," *IEEE Trans. Magnetics*, submitted.

[98] A. Nejatali and I. R. Ciric, "An iterative method employing neural networks for impedance imaging," *IEEE Trans. Indus. Electronics*, submitted.

[99] A. Y. Nooralahiyan, B. S. Hoyle, and N. J. Bailey, "Performance of neural network in image reconstruction and interpretation for electrical impedance tomography," *Digest of IEE Computer and Control Division Colloquium on Innovation in Instrumentation for Electrical Tomography*, no. 99, pp. 5/1-5/3, 1995.

[100] A. Y. Nooralahiyan, B. S. Hoyle, and N. J. Bailey, "Neural network for pattern association in electrical capacitance tomography," *IEE Proc. Circuits Syst.*, vol. 141, no. 6, pp. 517-521, 1994.

[101] J. Nyboer, S. Bagno, A. Bernett, and R. H. Halsey, "Radiocardiograms: Electrical impedance changes of the heart in relation to electrocardiograms and heart sounds," *J. Clin. Invest.*, vol. 10, p. 963, 1950.

[102] R. Pallas-Areny and J. G. Webster. "Bioelectric impedance measurements using synchronous sampling." *IEEE Trans. Biomed. Eng.*, vol. 40, pp. 824-829, Aug. 1993.

[103] Pedrycz, W., *Fuzzy Control and Fuzzy Systems*, New York, NY: J. Wiley, 1993.

[104] R. Plonsey and R. E. Collin, *Principles and Applications of Electromagnetic Fields*. New York, NY: McGraw-Hill Book Company, 1961.

[105] J. M. Porter and I. D. Swain, "Measurement of cardiac output by electrical impedance plethysmography," *J. Biomed. Eng.*, vol. 9, pp. 222-32, 1987.

[106] L. R. Price, "Electrical impedance computed tomography (ICT): A new CT imaging technique," *IEEE Trans. Nucl. Sci.*, vol. 26, pp. 2736-2739, Apr. 1979.

[107] M. Pomerantz, R. Baumgartner, J. Lauridson, and B. Eiseman, "Transthoracic

electrical impedance for the early detection of pulmonary edema," *Surgery*, vol. 66, pp. 260-8, 1969.

[108] R. Povill and P. Riu, "Quantification in multifrequency tomography," *Physiol. Meas.*, vol. 16, pp. A69-A78, 1995.

[109] B. Rigaud, L. Hamzaoui, M. R. Frikha, N. Chauveau and J. Morucci, "*In vitro* tissue characterization and modelling using electrical impedance measurements in the 100 Hz-10 MHz frequency range", *Physiol. Meas.*, vol. 16, no. 3A, pp. A15-A28, Aug. 1995.

[110] A. Rosenfeld and A. C. Kak, *Digital Picture Processing*, New York, NY: Academy Press, 1982.

[111] J. Rosell, J. Colominas, P. Riu, R. Pallas-Areny, and J. G. Webster, "Skin Impedance from 1 Hz to 1 MHz," *IEEE Trans. Biomed. Eng.*, vol. 35, pp. 649-651, 1988.

[112] V. N. S. Samarasooriya and P. K. Varshney, "Decentralized signal detection with fuzzy information," *Opt. Eng.*, vol. 36, no. 3, pp. 658-668, March 1997.

[113] V. N. S. Samarasooriya and P. K. Varshney, "A fuzzy modelling approach to decision fusion under uncertainty," in *Proc. 1996 IEEE Int. Conf. on Multisensor Fusion and Integration for Intelligent Syst.*, pp. 788-795, Washington DC.

[114] A. D. Seagar, D. C. Barber, and B. H. Brown, "Theoretical limits to sensitivity and resolution in impedance imaging," *Clin. Phys. Physiol. Meas.* 8 suppl. A, pp. 13-31, 1987.

[115] A. D. Seagar, D. C. Barber, and B. H. Brown, "Electrical impedance imaging," *Proc. Inst. Elect. Eng.*, vol. 134, pt. A, no. 2, pp. 201-210, Feb. 1987.

[116] A. Seagar and R. Bates, "Full-wave computed tomography. Part 4: Low-frequency

electric current CT," *IEE Proc. A*, vol. 132, pp. 455-66, 1985.

[117] A. Seagar, M. Yeo, and R. Bates, "Full-wave computed tomography. Part 2: Resolution limits," *IEE Proc. A*, vol. 131, pp. 612-22, 1984.

[118] S. J. Simske, "An adaptive current determination and a one-step reconstruction technique for a current tomography system," M.S. thesis, Dept. Biomed. Eng., Rensselear Polytechnic Institute, 1987.

[119] R. Skidmore, J. M. Evans, D. Jeckins, and P. N. wells, "A data collection system for gathering electrical impedance measurements from the human breast," *Clin. Phys. Physiol. Meas.* 8 suppl. A, pp. 99-102, 1987.

[120] L. Tarassenko, K. M. Pidcock, F. D. Murphy and P. Rolfe, "The development of impedance imaging techniques for use in the newborn at risk of intra-ventricular hemorrhage," in *Proc. 1985 IEE Int. Conf. on Electric and Magnetic Fields in Medicine and Biology*, pp. 83-87.

[121] R. Viswanathan and P. K. Varshney, "Distributed detection with multiple sensors: part I--Fundamentals," in *Proc. of the IEEE*, vol. 85, no. 1, pp. 54-63, Jan. 1997.

[122] J. J. Volpe, "Current methods in neonatal medicine," *N. Eng. J. Med.*, vol. 304, pp. 886-891, 1981.

[123] J. G. Webster, *Medical Instrumentation: Application and Design*. Boston: Houghton Mifflin, 1978.

[124] J. G. Webster, *Electrical Impedance Tomography*. Bristol: Adam Hilger, 1990.

[125] A. Wexler, B. Fry, and M. R. Neumann, "Impedance computed tomography algorithm and system," *Appl. Opt.*, vol. 24, pp. 3985-3992, Dec. 1985.

[126] A. Wexler, "Electrical impedance imaging in two and three dimensions," *Clin.*

Phys. Physiol. Meas., vol. 9, suppl. A, pp. 29-33, 1988.

[127] E. J. Woo, P. Hua, W. J. Tompkins, J. G. Webster, and R. Pallas-Areny, "Walsh function current patterns and data synthesis for electrical impedance tomography," *IEEE Trans. Medical Imaging*, vol. 11, no. 4, pp. 554-559, Dec. 1992.

[128] E. J. Woo, P. Hua, W. J. Tompkins, and J. G. Webster, "Measuring lung resistivity using electrical impedance tomography," *IEEE Trans. Biomed. Eng.*, vol. 39, pp. 756-760, July 1992.

[129] T. J. Yorkey, "Comparing reconstruction methods for electrical impedance tomography," Ph.D. thesis, Dept. Elect. Comp. Eng., Univ. of Wisconsin-Madison, 1986.

[130] T. J. Yorkey, J. G. Webster, and W. J. Tompkins, "An optimal impedance tomography reconstruction algorithm," in *Proc. 1986 IEEE 8th Annu. Conf. Eng. Med. Biol. Soc.*, pp. 103-104.

[131] T. J. Yorkey, J. G. Webster, and W. J. Tompkins, "Comparing reconstruction methods for electrical impedance tomography," *IEEE Trans. Biomed. Eng.*, vol. 34, pp. 843-852, Nov. 1987.

[132] T. J. Yorkey, J. G. Webster, and W. J. Tompkins, "An improved perturbation technique for electrical impedance imaging with some criticisms," *IEEE Trans. Biomed. Eng.*, vol. 34, pp. 898-901, Nov. 1987.

[133] E., J. Woo, W. J. Tompkins, and J. G. Webster, "Improved Newton-Raphson method and its parallel implementation," in *Proc. 1990 IEEE Annu. Conf. Eng. Med. Biol. Soc.*, Philadelphia, U.S.A., vol. 12, pp. 102-103.

[134] L. A. Zadeh, "Outline of a new approach to the analysis of complex systems and decision processes," *IEEE Trans. Syst., Man, and Cybern.*, vol. 3, pp. 28-44, 1973.

APPENDIX A

Analytical Solution

Consider a homogeneous circular cylinder with a coaxial inclusion of a circular cylinder of a different material, as shown in Fig. A.1. This test structure admits an analytical solution. Indeed, the electric potential satisfies Eq. (6.1) [106] with the boundary condition

$$j(\theta) = \gamma_2 \left.\frac{\partial \phi}{\partial n}\right|_{r = r_2} \tag{A.1}$$

where $j(\theta)$ is the injected current density, $\frac{\partial}{\partial n}$ denotes the normal derivative outwardly oriented, and $\gamma = \sigma + j\varepsilon$. $j(\theta)$ satisfies the condition

$$\int_0^{2\pi} j(\theta)\, d\theta = 0. \tag{A.2}$$

The average potential on the boundary is assumed to be zero,

$$\int_0^{2\pi} \phi(r_2, \theta)\, d\theta = 0. \tag{A.3}$$

This problem can be solved analytically by using the method of separation of variables in polar coordinates. At the interface $r = r_1$, continuity of the current density and continuity of potential imply

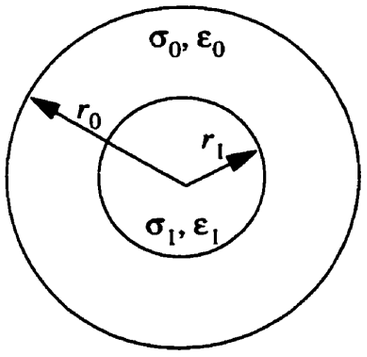

Fig. A.1 A homogeneous cylinder with a coaxial cylindrical anomaly inside.

$$\gamma_1 \frac{\partial \phi}{\partial r}\bigg|_{r_1^-} = \gamma_0 \frac{\partial \phi}{\partial r}\bigg|_{r_1^+} \quad \text{and} \quad \phi(r_1^-) = \phi(r_1^+). \tag{A.4}$$

In the circle $0 < r < r_1$ and annulus $r_1 < r < r_0$, Eq. (6.1) in polar coordinates simplifies to

$$r \frac{\partial}{\partial r}\left(r \frac{\partial \phi}{\partial r}\right) + \frac{\partial^2 \phi}{\partial \theta^2} = 0. \tag{A.5}$$

Let $\phi = R(r)\,\Theta(\theta)$. Then Eq. (A.5) can be written as

$$r \frac{d}{dr}\left(r \frac{dR}{dr}\right)\Theta + R \frac{d^2 \Theta}{d\theta^2} = 0. \tag{A.6}$$

Dividing both sides by ΘR

$$\frac{1}{R} r \frac{d}{dr}\left(r \frac{dR}{dr}\right) = -\frac{1}{\Theta} \frac{d^2 \Theta}{d\theta^2} = k^2. \tag{A.7}$$

In general both k^2 and $-k^2$ should be considered but, in this case as the periodic boundary

conditions are only present just the plus sign is used.

Eq. (A.7) constitutes two ordinary differential equations that are separated and can be solved individually. The solution of Eq. (A.5) would be the multiplication of these two equations. The solution of

$$k^2\Theta + \frac{d^2\Theta}{d\theta^2} = 0 \tag{A.8}$$

is:

$$\Theta = k''\cos(k\theta + k') \tag{A.9}$$

where k, k' and *k"* are constants that remain to be found.

The other differential equation can be rewritten as

$$r\frac{d}{dr}\left(r\frac{dR}{dr}\right) - k^2R = 0 \tag{A.10}$$

or

$$r^2\frac{d^2R}{dr^2} + r\frac{dR}{dr} - k^2R = 0. \tag{A.11}$$

With a new variable named t defined as

$$r = e^t \quad \text{or} \quad t = \ln r \quad \text{and} \quad \frac{dt}{dr} = \frac{1}{r} \tag{A.12}$$

derivatives with respect to r can be written as

$$\frac{dR}{dr} = \frac{dR}{dt}\frac{dt}{dr} = \frac{1}{r}\frac{dR}{dt} \quad \text{and} \tag{A.13}$$

$$\frac{d^2R}{dr^2} = \frac{-1}{r^2}\frac{dR}{dt} + \frac{1}{r^2}\frac{d^2R}{dt^2}. \tag{A.14}$$

By substituting Eqs. (A.13) and (A.14) in Eq. (A.11), one will have

$$r^2\left(\frac{-1}{r^2}\frac{dR}{dt}+\frac{1}{r^2}\frac{d^2R}{dt^2}\right)+r\left(\frac{1}{r}\frac{dR}{dt}\right)-k^2R=0 \tag{A.15}$$

which can be simplified to

$$\frac{d^2R}{dt^2}-k^2R=0. \tag{A.16}$$

The answer to this differential equation is

$$R=Ae^{-kt}+Be^{kt}. \tag{A.17}$$

By substituting t with $\ln(r)$, one comes to

$$\begin{aligned} R &= Ae^{-k\ln r}+Be^{k\ln r} \\ &= Ae^{-\ln r^k}+Be^{\ln r^k} \\ &= Ae^{\ln\frac{1}{r^k}}+Be^{\ln r^k} \\ &= \frac{A}{r^k}+Br^k. \end{aligned} \tag{A.18}$$

For the annulus $r_1 < r < r_0$ the full answer is

$$\phi=\left(\frac{A}{r^k}+Br^k\right)(k''\cos(k\theta+k'))=\left(\frac{A'}{r^k}+B'r^k\right)(\cos(k\theta+k')) \tag{A.19}$$

and for the circle $0 < r < r_1$ as the first term in Eq. (A.18) produces a singularity and should be eliminated, one will have

$$\phi=B''r^k\cos(k\theta+k') \tag{A.20}$$

A', B', k, k' and B'' are constants that should be found by applying the boundary conditions.

By applying the second boundary condition in Eq. (A.4), one will have

$$B''r_1^k\cos(k\theta+k') = \left(\frac{A'}{r_1^k}+B'r_1^k\right)(\cos(k\theta+k')) \tag{A.21}$$

which simplifies to

$$B''r_1^k = \frac{A'}{r_1^k}+B'r_1^k. \tag{A.22}$$

The first part of Eq. (A.4) or

$$\gamma_1\frac{\partial\phi}{\partial r}\bigg|_{r_1^-} = \gamma_0\frac{\partial\phi}{\partial r}\bigg|_{r_1^+}$$

is the other of our boundary conditions. By applying this to Eq. (A.20) one can write

$$\gamma_1 B''kr_1^{k-1}\cos(k\theta+k') = \gamma_0\left(\frac{-A'k}{r_1^{k+1}}+B'kr_1^{k-1}\right)\cos(k\theta+k') \tag{A.23}$$

or

$$\gamma_1 B''kr_1^{k-1} = \gamma_0\left(\frac{-A'k}{r_1^{k+1}}+B'kr_1^{k-1}\right). \tag{A.24}$$

Now one can apply the boundary condition related to injected currents introduced in Eq. (A.1) and get

$$j(\theta) = \sum_{l=1}^{\infty} a_l\cos(l\theta+\eta_l) = \gamma_0\left(\frac{-A'k}{r_0^{k+1}}+B'kr_0^{k-1}\right)\cos(k\theta+k') \tag{A.25}$$

The first term in this expression is the trigonometric series expansion of injected current. This expansion is not the usual Fourier series because does not have sine terms and has a phase term, η_l, instead. One can solve this equation separately for each term on left hand side, on the other words, for each l, there are a set of answers for A', B' and B''. These answers are found by using Eqs. (A.22), (A.24) and (A.25).

A manageable case occurs when the injected current density is simply

$$j(\theta) = \cos(\theta) . \tag{A.26}$$

In this case $\eta_1 = 0$, $a_1 = 1$, $k = 1$ and all other term of summation are zero. Therefore from Eq. (A.25), one gets

$$a_1 = \gamma_0\left(\frac{-A'}{r_0^2} + B'\right) = 1 . \tag{A.27}$$

For $k = 1$ from Eq. (A.24)

$$\gamma_1 B'' = \gamma_0\left(\frac{-A'}{r_1^2} + B'\right) \tag{A.28}$$

In the same way for Eq. (A.22)

$$B'' r_1 = \frac{A'}{r_1} + B' r_1 . \tag{A.29}$$

One has to solve these equations to find the constants. To do that from Eq. (A.27)

$$B' = \frac{1}{\gamma_0} + \frac{A'}{r_0^2} \tag{A.30}$$

from Eq. (A.28)

$$B'' = \frac{\gamma_0}{\gamma_1}\left(\frac{A'}{r_0^2} - \frac{A'}{r_1^2} + \frac{1}{\gamma_0}\right) \tag{A.31}$$

and from Eq. (A.29)

$$B'' = \frac{A'}{r_1^2} + \frac{1}{\gamma_0} + \frac{A'}{r_0^2} . \tag{A.32}$$

Combining Eqs. (A.31) and (A.32) and after a lengthy but straightforward manipulation

$$A' = \frac{r_0^2 r_1^2 (\gamma_1 - \gamma_0)}{\gamma_0^2 (r_1^2 - r_0^2) - \gamma_0 \gamma_1 (r_1^2 + r_0^2)} . \tag{A.33}$$

Inserting this into Eq. (A.31) and performing the necessary simplifications

$$B'' = \frac{1}{\gamma_0} + \frac{(r_1^2 + r_0^2)\,(\gamma_1 - \gamma_0)}{\gamma_0^2\,(r_1^2 - r_0^2) - \gamma_0\gamma_1\,(r_1^2 + r_0^2)} \tag{A.34}$$

$$= \frac{-2\gamma_0 r_0^2}{\gamma_0^2\,(r_1^2 - r_0^2) - \gamma_0\gamma_1\,(r_1^2 + r_0^2)}. \tag{A.35}$$

Finally for B'

$$B' = \frac{-\gamma_0 r_0^2 - \gamma_1 r_0^2}{\gamma_0^2\,(r_1^2 - r_0^2) - \gamma_0\gamma_1\,(r_1^2 + r_0^2)}. \tag{A.36}$$

Using these values in Eq. (A.19) and for r_0 of interest, the final answer after many manipulations is

$$\phi(r_0, \theta) = \frac{r_0}{\gamma_0}\,\frac{\gamma_1\,(R^2 - 1) - \gamma_0\,(R^2 + 1)}{\gamma_0\,(R^2 - 1) - \gamma_1\,(R^2 + 1)}\cos\theta \tag{A.37}$$

where $R = r_1/r_0$.

APPENDIX B

B.1 Neural Networks

Neural networks are known for their parallel and distributed structures with a significant level of learning capability. They operate on an exclusively numerical level (usually [0,1] or [-1,1]) where their basic computational components (computational neurons) are quite simple processing units. The computational neurons realize a weighted sum of input signals $x_1, x_2, \ldots, x_n$ in say $\sum_{i=1}^{n} w_i x_i + b$ where w_i's are called weights and b denotes the so-called bias term, followed by a nonlinear static transformation. This nonlinear transformation usually shows a saturation behaviour (see Fig. A.1). The neurons are then arranged into layers where the number of layers as well as their dimensions, specify the capabilities of the resulting network. Knowledge is accommodated in the neural networks by distributing it among the connections of the network. Thus the resulting structure is fairly difficult to interpret. In other words, one can not convert them into a series of readable 'if-then' statements or any other type of representation of the explicit format.

There are several kinds of neural networks such as backpropagation, competitive, counter-propagation and associative memory networks. The backpropagation network is the most popular one and has been used in a lot of applications. In line with its popularity

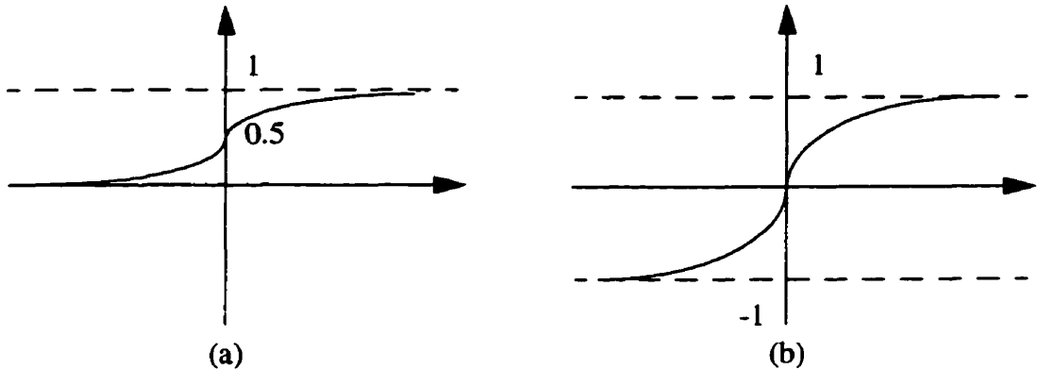

Fig. B.1 (a) Sigmoid and (b) tangent hyperbolic activation functions.

extensive work has been done to improve its performance. There is also a wide variety of backpropagation networks according to number of layers, type of activation function for neurons and learning rules. One layer or two layer networks with nonlinear activation functions are an ideal device to simulate nonlinear functions. Furthermore it has been claimed that a two layer backpropagation network with nonlinear units and suitable number of neurons in hidden layer is able to simulate a nonlinear function with any degree of complexity whatsoever.

B.2 Backpropagation Network Operation

Here a description of the network operation is presented to illustrate how the backpropagation neural network (BPNN) can be used to solve complex problems. In summary the networks learns a predefined set of input-output example pairs by using a training cycle. An input pattern is applied as a stimulus to the first layer of network units

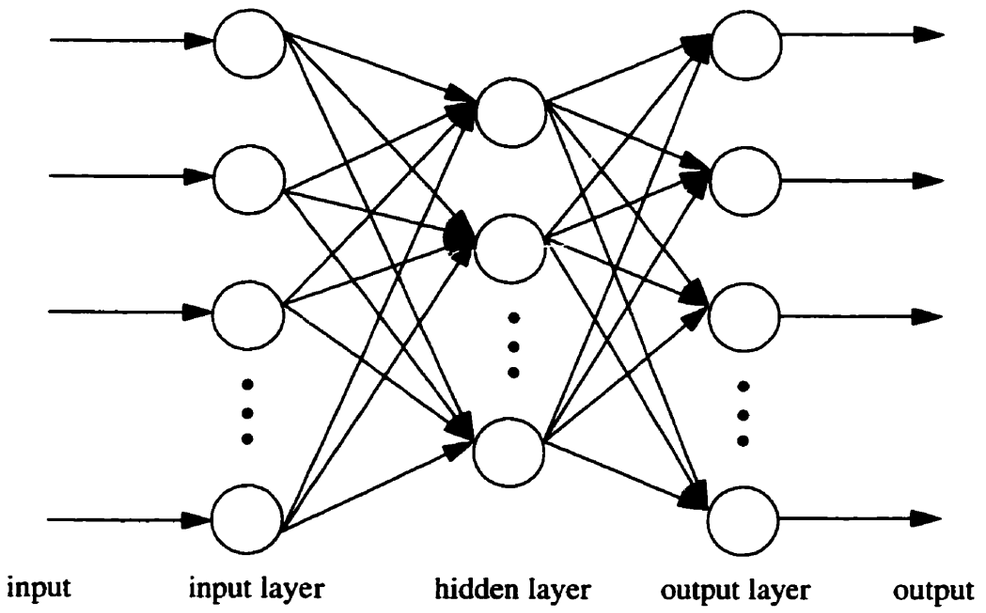

Fig. B.2 The general backpropagation network architecture.

(neurons), then it is propagated through each upper layer until an output is generated. This output pattern is then compared to the desired output, and an error is computed for each output unit (see Fig. A.2).

The error is then transmitted backward from the output layer to each node in the intermediate layer that directly contributes to the output. Each unit in the intermediate layer receives only a portion of the total error value based roughly on the relative contribution the unit made to the original output. This process continues, layer by layer, until each node in the network receives an error value that describes its relative contribution to the total error. Connection weights, based on their unit relative error value, are then updated to converge toward a state that in it, all the training patterns are encoded.

As the result of this training process the neurons of each layer of the neural network organize their weights such that different features of the their input space are learned. Upon completion of the training, when presented with an arbitrary input pattern that is noisy or incomplete, the units in the next layer of the network will respond with an output that resembles the features they learned to recognize during training and meanwhile inhibit their outputs if their input pattern does not contain those features.

As signals propagate through the subsequent layers in the network, the input pattern presented to each upper layer can be thought of as a pattern with features that can be recognized by units in that layer. The generated output pattern can be thought of as a feature map that provides an indication of the presence or absence of feature combinations at the input. This behaviour provides an effective means for the BPNN to allow a computer system to examine data patterns that may be incomplete or noisy, and to recognize subtle patterns from the partial input.

It has been shown that during training, BPNN tends to develop internal relationship between nodes so as to organize data into classes of patterns [42]. This tendency has resulted in assuming that all hidden-layer units in the BPNN are somehow associated with specific features of the input pattern as a result of training. Thus, the BPNN classifies these previously unseen inputs according to features that share with the training examples.

B.2.1 The Generalized Delta Rule

Here the formal mathematical description of BPNN operation is presented. The generalized delta rule (GDR), a member of a wider class named gradient descent training, is derived in detail for the learning algorithm of the network. Figure A.2 serves as the

reference for most of the discussion. The BPNN is a layered, feedforward network that is fully interconnected. There are no feedback connections and no connections that bypass one layer to go directly to the later layer. Although only three-layer BPNN (sometimes called two-layer network because the input layer is just used to fan out the input vector to the next layer) is discussed here, more layers are also permissible.

A neural network is called a mapping network if it computes a functional relationship between its input and its output. For example, if the input to a network is the value of an angle, and the output is the cosine of that angle, the network performs the mapping $\theta \rightarrow \cos\theta$. For such a simple function, neural networks are not needed, however, one might want to perform a complicated mapping where the description of the functional relationship in not known in advance, but some examples of the correct mapping are known. In this situation, the power of a neural network to discover its own algorithms is extremely useful.

Suppose there are a set of P vector-pairs, (x_1, y_1), (x_2, y_2), ... , (x_p, y_p), which are examples of a functional mapping $\mathbf{y} = \phi(\mathbf{x})$; $\mathbf{x} \in \mathbf{R}^N, \mathbf{y} \in \mathbf{R}^M$. A network is going to be trained such that it approximates the desired function $\mathbf{o} = \mathbf{y}' = \phi'(\mathbf{x})$. A method will be explained to do this training which usually works provided that there is a sufficient number of the properly chosen training-vector pairs, and there are sufficient layers and units in the network. Remember that learning in a neural network means finding an appropriate set of weights. This problem is a generalization of the least mean square rule and resembles the problem of finding the equation of a line that best fits a number of known points. Unlike the line-fitting problem, the relationship that is going to be mapped using BPNN is likely to be nonlinear as well as multidimensional, thus, a least-square approxi-

mation is employed which is an iterative version of the simple least-squares method, called gradient descent training.

To begin, let's review the equation for information processing in the three-layer network in figure A.2. An input vector, $x_p = (x_{p1}, x_{p2}, \ldots, x_{pN})^t$, is applied to the input layer of the network. The input units distribute the values to the hidden-layer units. The net input to the jth hidden unit is

$$net_{pj}^h = \sum_{i=1}^{N} w_{ji}^h x_{pi} + b_j^h \tag{B.1}$$

where w_{ji}^h is the weight on the connection from the ith input unit, and b_j^h is the bias term. The "h" superscript refers to quantities on the hidden layer. Then, the output of this node is

$$i_{pj} = f_j^h\left(net_{pj}^h\right). \tag{B.2}$$

Similarly, the equations for the output nodes are

$$net_{pk}^o = \sum_{i=1}^{L} w_{kj}^o i_{pi} + b_j^o \tag{B.3}$$

$$o_{pj} = f_k^o\left(net_{pk}^o\right) \tag{B.4}$$

where the "o" superscript refers to quantities on the output layer.

The initial set of weight values represents a first guess as to the proper weights for the problem. The basic procedure for training the network is embodied in the following description:

1) Apply an input vector to the network and calculate the corresponding output values.

2) Compare the computed outputs with the correct outputs and determine a measure of the error.

3) Determine in which direction (+ or -) each weight changes in order to reduce the error.

4) Determine the amount of change for each weight.

5) Apply the corrections to the weights.

6) Repeat items 1 through 5 with all the training vectors until the error for all vectors in the training set is reduced to an acceptable value.

The next section explains this description in detail.

B.2.2 Update of Output-Layer Weights

The error at a single output unit k is defined to be $\delta_{pk} = \left(y_{pk} - o_{pk} \right)$, where the subscript "$p$" refers to the pth training vector. In this case, y_{pk} is the desired output value, and o_{pk} is the actual output from the kth unit. The error to be minimized by the GDR is defined as the sum of the squares of the errors for all M output units:

$$E_p = \frac{1}{2} \sum_{k=1}^{M} \delta_{pk}^2 . \tag{B.5}$$

The factor of $\frac{1}{2}$ in Eq. (7.5) is there for convenience when derivatives later are calculated. Since an arbitrary constant appears in the final result, the presence of this factor does not invalidate the derivation.

To determine the direction in which to change the weights, the negative of the

gradient of E_p, ∇E_p is calculated, with respect to the weights, w_{kj}. Then the values of the weights can be adjusted such that the total error is reduced.

To keep the derivation trackable, consider each component of ∇E_p separately. From Eq. (7.5) and the definition of δ_{pk},

$$E_p = \frac{1}{2}\sum_k \left(y_{pk} - o_{pk}\right)^2 \tag{B.6}$$

and

$$\frac{\partial E_p}{\partial w_{kj}^o} = -\left(y_{pk} - o_{pk}\right)\frac{\partial}{\partial\left(net_{pk}^o\right)}\left(f_k^o\right)\frac{\partial}{\partial w_{kj}^o}\left(net_{pk}^o\right) \tag{B.7}$$

where Eq. (7.4) has been used for the output value, o_{pk}, and the chain rule for the partial derivatives. For the moment, the derivative of f_k^o is not evaluated, but instead is written simply as $f_k^{o\prime}\left(net_{pk}^o\right)$. The last factor in Eq. (7.7) is

$$\frac{\partial}{\partial w_{kj}^o}\left(net_{pk}^o\right) = \frac{\partial}{\partial w_{kj}^o}\left(\sum_{j=1}^{L} w_{kj}^o i_{pj} + b_k^o\right) = i_{pj}. \tag{B.8}$$

Combining Eqs. (7.7) and (7.8), the negative gradient is

$$-\frac{\partial E_p}{\partial w_{kj}^o} = \left(y_{pk} - o_{pk}\right)f_k^{o\prime}\left(net_{pk}^o\right)i_{pj}. \tag{B.9}$$

As far as the magnitude of the weight change is concerned, it is taken to be proportional to the negative gradient. Thus, the weights on the output layer are updated according to

$$w_{kj}^{o}(t+1) = w_{kj}^{o}(t) + \Delta_p w_{kj}^{o}(t) \tag{B.10}$$

where

$$\Delta_p w_{kj}^{o} = \eta\left(y_{pk} - o_{pk}\right) f_k^{o\prime}\left(net_{pk}^{o}\right) i_{pj}. \tag{B.11}$$

The factor η is called the learning rate and is positive and usually less than 1.

B.2.3 Update of Hidden-Layer Weights

It would be favourable if the same calculations could be done for the hidden layer but, a problem arises when trying to define a measure of the error of the outputs of the hidden-layer units. Although the actual output for the last layer is known, there is no way of knowing in advance what the correct output for units in hidden layer should be. It is known by intuition that the total error, E_p must somehow be related to the output values on the hidden layer. This can be verified by going back to Eq. (7.6):

$$E_p = \frac{1}{2}\sum_k \left(y_{pk} - o_{pk}\right)^2$$

$$E_p = \frac{1}{2}\sum_k \left(y_{pk} - f_k^{o}\left(net_{pk}^{o}\right)\right)^2$$

$$E_p = \frac{1}{2}\sum_k \left(y_{pk} - f_k^{o}\left(\sum_j w_{kj}^{o} i_{pj} + b_k^{o}\right)\right)^2$$

where i_{pj} depends on the weights on the hidden layer through Eqs. (7.1) and (7.2). This fact can be exploited to calculate the gradient of E_p with respect to the hidden-layer weights.

$$\frac{\partial E_p}{\partial w_{kj}^h} = \sum_k \frac{\partial}{\partial w_{kj}^h}\left(y_{pk} - o_{pk}\right)^2$$

$$= -\sum_k \left(y_{pk} - o_{pk}\right) \frac{\partial o_{pk}}{\partial\left(net_{pk}^o\right)} \frac{\partial}{\partial i_{pj}}\left(net_{pk}^o\right) \frac{\partial i_{pj}}{\partial\left(net_{pk}^h\right)} \frac{\partial}{\partial w_{ji}^h}\left(net_{pk}^h\right) \qquad \text{(B.12)}$$

where each of the factors in Eq. (7.12) can be calculated explicitly from previous equations. The result is

$$\frac{\partial E_p}{\partial w_{kj}^h} = -\sum_k \left(y_{pk} - o_{pk}\right) f_k^{o\prime}\left(net_{pk}^o\right) w_{kj}^o f_k^{h\prime}\left(net_{pk}^h\right) x_{pi}. \qquad \text{(B.13)}$$

Hidden-layer weights are updated in proportion to the negative of Eq. (7.13):

$$\Delta_p w_{ji}^h = \eta f_j^{h\prime}\left(net_{pj}^h\right) x_{pi} \sum_k \left(y_{pk} - o_{pk}\right) f_k^{o\prime}\left(net_{pk}^o\right) w_{kj}^o \qquad \text{(B.14)}$$

where η is once again the learning rate.

The definition of δ_{pk}^o given in the previous section can be used to write

$$\Delta_p w_{ji}^h = \eta f_j^{h\prime}\left(net_{pj}^h\right) x_{pi} \sum_k \delta_{pk}^o w_{kj}^o. \qquad \text{(B.15)}$$

Note that every weight update on the hidden layer depends on all the terms, δ_{pk}^o, on the output layer. This formulation shows the philosophy behind the backpropagation term. The known errors on the output layer are propagated back to the hidden layer to determine the appropriate changes on that layer. By defining a hidden-layer error term

$$\delta_{pk}^h = f_j^{h\prime}\left(net_{pj}^h\right) \sum_k \delta_{pk}^o w_{kj}^o \qquad \text{(B.16)}$$

the weight update equations becomes analogous to those for the output layer:

$$w_{ji}^{h}(t+1) = w_{ji}^{h}(t) + \eta \delta_{pj}^{h} x_i \qquad \text{(B.17)}$$

APPENDIX C

C.1 Elements of Fuzzy Set Theory

Fuzzy set theory introduction starts with the review of two-valued logic which is the foundation of our mathematical knowledge, where every concept is given a measure of correctness of only true or false [103]. Any object no matter how complex it is, is forced to be specified within any of two rigid and complementary categories. These categories in the real world may be defined for instance as good and bad, positive and negative or tall and short. Although, this classification is sometimes enough and satisfactory, in some cases it causes serious and obvious dilemmas. For example in the study of numbers, two categories of positive and negative numbers can be defined without any problem and the boundaries of each category is well defined, but, in so many other tasks such as speed, definition of the concept of fast and slow are not well defined and do not have clear boundaries.

Nevertheless, concepts such as speed, height, error and temperature, have to be dealt with in many daily activities where, the two-valued logic shows an obvious shortcoming. Definitely, no matter what definition is adopted for the border point x_0 in the concept of $f(x)$

$$f(x) = \begin{cases} 1 & if \quad x > x_0 \\ 0 & if \quad x \leq x_0 \end{cases} \tag{C.1}$$

the problem is not alleviated.

Assigning an object to either of these complementary categories is equivalent to deciding on its membership to the related set. For instance, the temperature of the room could be assigned to the set of comfortable temperature if it is considered to be comfortable. In the two-valued logic or set theory, one has to decide on boundary values that describe the comfortable temperature, e.g., the interval of 22 to 28 degrees. The dilemma that was mentioned, is obvious here. One may ask, if the 22 degrees is a comfortable temperature, then does it make sense to call the 21.99 degrees as uncomfortable temperature? The key issue of fuzzy set theory is that it extends the meaning of membership to different grades of belonging, also called membership values. This alleviates the previous problem by embracing all intermediate situations between complete (total) membership and total nonmembership.

Note, that different grades of membership or fuzziness, is quite different from the concept of randomness.

From this introduction it seems that there are sufficient reasons to follow the main idea of fuzziness and construct equivalent tools to those in the set theory e.g. intersection, union, etc. for fuzzy set theory. This would enable one to handle fuzziness, a concept that seems to be a lost piece in the jigsaw of our mathematical knowledge. Remember, fuzzy concepts, e.g. enough, comfort, good and suitable, all are indivisible from our daily life.

As mentioned before, fuzzy set theory modifies the basic idea of set theory to allow for the intermediate grades of membership. If showing the membership of an object x to a fuzzy set A as $A(x)$, then the bigger the value of $A(x)$ means the stronger the link between x and the fuzzy set A.

C.1.1 Example

An example would be instructive to show some basic applications of fuzziness in engineering and control. Let us assume that the target (goal) of our control algorithm is to set the duration of a control light at an intersection. Our aim can be stated in a linguistic phrase as 'heavier traffic, longer green light'. The first problem in constructing a control system arises when we want to compile 'heavy' in terms of say 'cars per minute'. One can say that if traffic is less than fifty cars per minute then it is not heavy and other wise it is heavy. But obviously it is not a satisfactory estimate to assign forty nine as light and fifty as heavy. The problem is not alleviated by defining a new number as border line.

Everybody accepts that five cars per minute is a light traffic and also one hundred per minute is heavy but, for any number in the remaining interval not an explicit attribute can be found. The best way to deal with this problem is to assign membership values somewhere in the interval [0,1]. Fig. 8.1(b) shows such a membership function for our problem. We are not considering the discussion that deals with how to find such a mem-

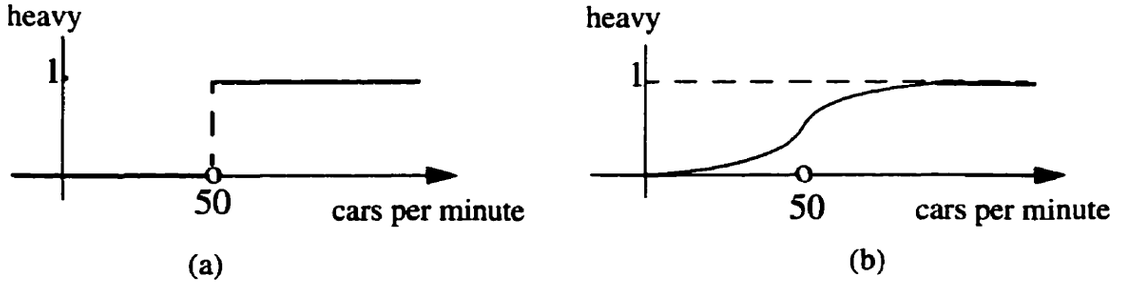

Fig. C.1 (a) Boolean membership function of heavy traffic. (b) Fuzzy membership function of heavy traffic.

bership function to be realistic for the moment.

C.1.2 Operations on Fuzzy Sets

Accepting such a many valued membership function is the first and most important one. Following that we have to define new rules concerning set theory such as union, intersection and complement. Although we are not going to explain all mathematical background of fuzzy sets here but, some elementary and basic rules which specially are related to the next sections of this chapter worth repeating. The most general definition of union and intersection in fuzzy sets theory are expressed under triangular norms titie. They are also call *t*-norm and *s*-norm respectively equivalent to intersection and union. Unlike set theory, there are not unique definitions for intersection and union in fuzzy set theory. Some common types of *t*-norms ($\wedge$) and *s*-norms ($\vee$) are as follows:

$$\begin{gathered} AtB = min(A, B) \\ AtB = AB \\ AtB = max(0, (\lambda+1)(A+b-1) - \lambda AB), \lambda \geq -1 \end{gathered} \tag{C.2}$$

which the last one with $\lambda = 0$ is the most usual case.

$$\begin{gathered} AsB = max(A, B) \\ AsB = A + B - AB \\ AsB = min(1, A + B + \lambda AB), \lambda \geq -1 \end{gathered} \tag{C.3}$$

Again usually the $\lambda = 0$ is the case.

Complement is also defined by:

$$\bar{A} = 1 - A \tag{C.4}$$

The possibility measure of fuzzy set A with respect to fuzzy set B is defined as

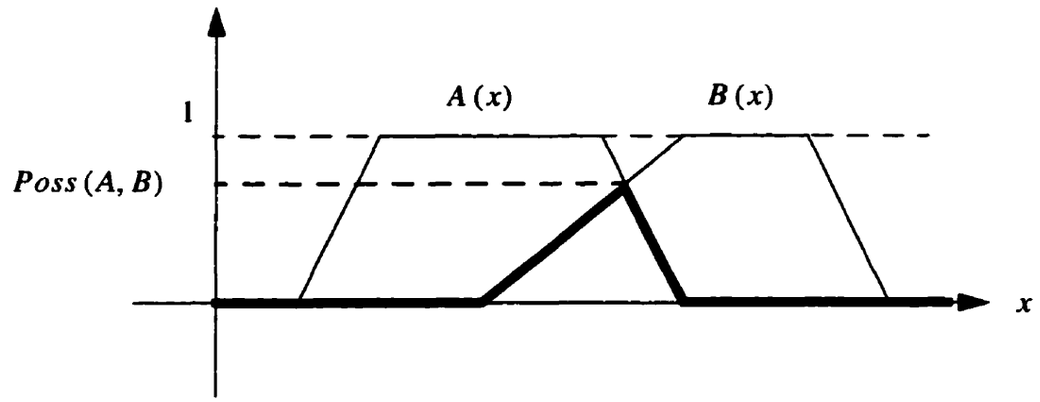

Fig. C.2 Possibility measure of $A(x)$ with respect to $B(x)$ is a measure of overlap between these two membership functions; the t-norm is based on minimum here.

$$\Pi(A, B) = Poss(A, B) = \sup_{x \in X} [A(x) \wedge B(x)] . \tag{C.5}$$

The necessity measure of A with respect to B, $N(A|B)$, similarly is defined as

$$\eta(A|B) = Nec(A, B) = \inf_{x \in X} [A(x) \vee \overline{B}(x)] \quad . \tag{C.6}$$

To interpret both of these, notice that the possibility measure of A and B reflects the extent to which A and B coincide or overlap, while the necessity expresses a grade to which B is contained in A.

C.1.3 Membership Function Estimation

The methods for estimation of a fuzzy membership function can be classified in two categories: 1) structure free and 2) structure bound algorithms. From these two categories the first one applies to our approach. From the first category, one may name hori-

zontal, vertical, Saaty and fuzzy clustering approaches. Again from this list, horizontal approach seems to be the most pertinent one to our case.

In this approach a list of elements of the universe of discourse x_1, x_2, ..., x_n are selected and referred to a group of experts. This group answers to the question "can x_i be accepted as a member of fuzzy set A?". An average of positive answers to this question forms the membership value of fuzzy set A at point x_i;

$$A(x_i) = \frac{positive(x_i)}{N} \tag{C.7}$$

where N is the number of questions.

APPENDIX D

Random Generator with Trapezoidal Probability Density Function

Figure 8.7 shows our map. γ in trapezoidal pdf will be selected in a way to have the trapezoidal area equal to one as it should be,

$$\left(m_1 - l\right)\frac{\gamma}{2} + \left(m_2 - m_1\right)\gamma + \left(u - m_2\right)\frac{\gamma}{2} = 1 \tag{D.1}$$

or

$$\gamma = \frac{2}{u + m_2 - m_1 - l}. \tag{D.2}$$

There are three different parts in the trapezoidal pdf. Two triangle and one rectangular.

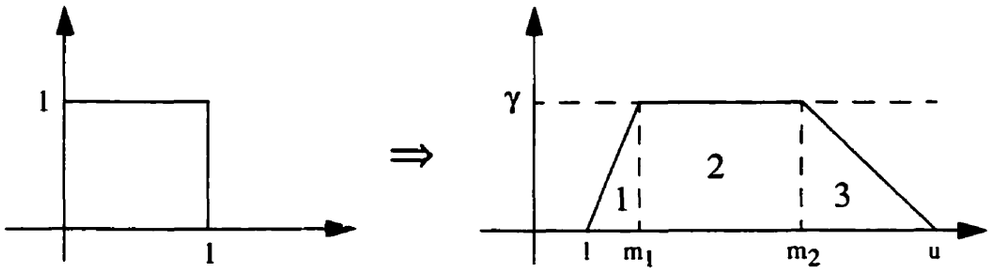

uniform pdf over [0, 1] interval trapezoidal pdf

Fig. D.1 Mapping from uniform pdf to trapezoidal one.

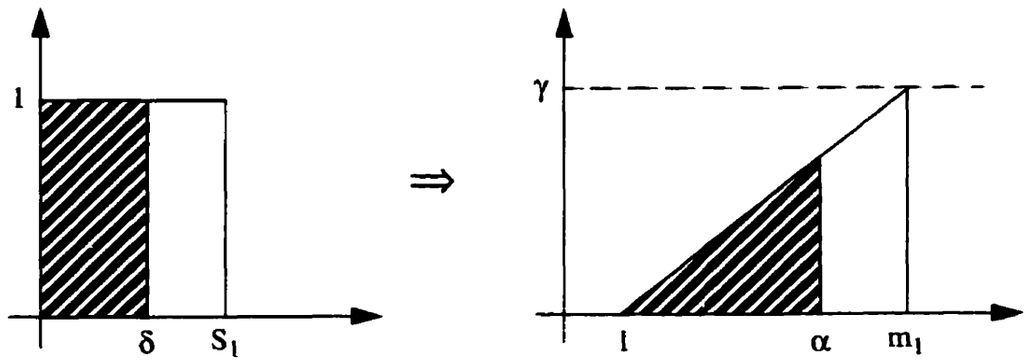

Fig. D.2 Mapping of the first section.

Each of them will receive a portion of the uniform pdf equivalent to its share of area. Therefore the area of each sections is needed and they are calculated as:

$$S_1 = \frac{m_1 - l}{u + m_2 - m_1 - l} \quad S_2 = \frac{2\left(m_2 - m_1\right)}{u + m_2 - m_1 - l} \quad S_3 = \frac{u - m_2}{u + m_2 - m_1 - l} \tag{D.3}$$

where S_1, S_2 and S_3 refer to the areas of those marked with 1, 2 and 3 in Fig. 8.7, respectively.

We now split the mapping operation to three parts. The first mapping in shown in Fig. 8.8. To have a correct mapping there should be equivalent area sweeping between two pdf's. On the other words δ should be mapped to α in a way that shaded areas be equal. In mathematical words:

$$\frac{\delta}{S_1} = \frac{\left(\frac{\alpha - l}{m_1 - l}\right)\gamma(\alpha - l)\frac{1}{2}}{\left(m_1 - l\right)\frac{\gamma}{2}} = \left(\frac{\alpha - l}{m_1 - l}\right)^2 \tag{D.4}$$

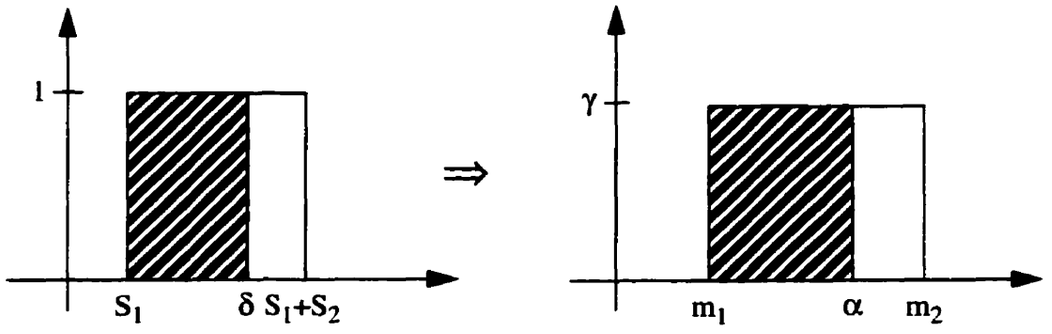

Fig. D.3 Mapping of the second section.

and after some manipulation,

$$\alpha = l + \left(m_1 - l\right)\sqrt{\frac{\delta}{S_1}} \tag{D.5}$$

or,

$$\sigma = l + \sqrt{(rand)\left(m_1 - l\right)\left(u + m_2 - m_1 - l\right)} \tag{D.6}$$

where σ is a random number with objective trapezoidal pdf and *rand* a uniform distributed random number.

Similarly, the second part is shown in Fig. 8.9. The mapping is very simple in this case and a linear one. By the same law of equity of areas, we have:

$$\frac{\delta - S_1}{S_2} = \frac{\left(\alpha - m_1\right)\gamma}{\left(m_2 - m_1\right)\gamma}. \tag{D.7}$$

And after some mathematical simplification the final result is:

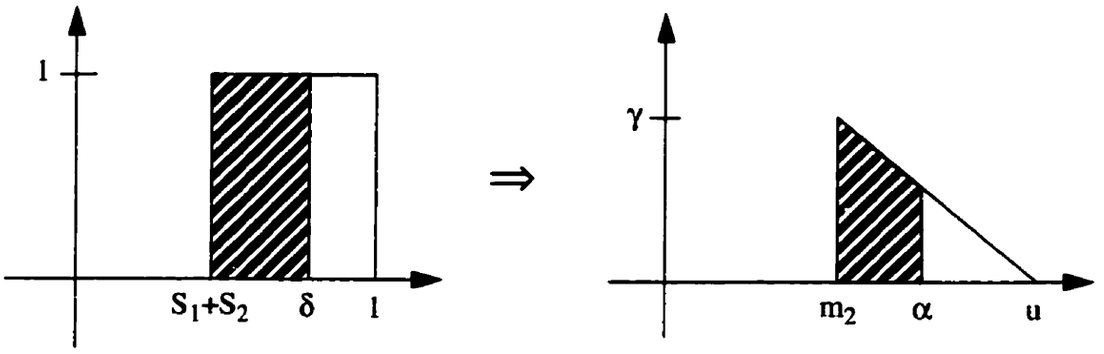

Fig. D.4 Mapping of the third section.

$$\sigma = \left(\frac{m_2 - m_1}{S_2}\right)(rand) + \left(m_1 - \frac{S_1\left(m_2 - m_1\right)}{S_2}\right). \tag{D.8}$$

And finally for the third part as shown in Fig. 8.10 we have:

$$\frac{\delta - \left(S_1 + S_2\right)}{1 - \left(S_1 + S_2\right)} = \frac{\frac{1}{2}\left(\gamma + \frac{(u-\alpha)}{\left(u - m_2\right)}\gamma\right)\left(\alpha - m_2\right)}{\frac{\gamma}{2}\left(u - m_2\right)} \tag{D.9}$$

that after a lengthily manipulation comes to

$$\sigma = u - \sqrt{\frac{\left(u - m_2\right)^2}{1 - \left(S_1 + S_2\right)}(1 - rand)}\,. \tag{D.10}$$